A model perspective on orbital forcing of monsoons and Mediterranean climate using EC-Earth

UTRECHT STUDIES IN EARTH SCIENCES
No. 55

Members of the dissertation committee:

Dr. P. Braconnot
Laboratoire des Sciences du Climat et de l'Environment, Gif-sur-Yvette, France

Prof. Dr. H. A. Dijkstra
Faculty of Science, Utrecht University, the Netherlands

Prof. Dr. H. Middelkoop
Faculty of Geoscience, Utrecht University, the Netherlands

Prof. Dr. H. Renssen
Faculty of Earth and Life Sciences, Vrije Universiteit Amsterdam, the Netherlands

Prof. Dr. E. Rohling
Research School of Earth Sciences, The Australian National University, Canberra, Australia

The research in this thesis was financially supported by a "Focus en Massa" grant from Utrecht University and was carried out at:

Stratigraphy and Paleontology, Department of Earth Sciences, Faculty of Geosciences, Universiteit Utrecht, The Netherlands
&
Royal Netherlands Meteorological Institute (KNMI), de Bilt, Netherlands

ISBN: 978-90-6266-357-6
Printed by Wöhrmann Print Service Zutphen
Copyright © 2014 Joyce Bosmans
Cover design by Joyce Bosmans and Margot Stoete
All rights reserved. No part of this publication may be copied or reproduced in any form without written permission of the author.

A model perspective on orbital forcing of monsoons and Mediterranean climate using EC-Earth

Een kijk op de astronomische sturing van moessons en het Mediterrane klimaat in het EC-Earth model (met een samenvatting in het Nederlands)

PROEFSCHRIFT

ter verkrijging van de graad van doctor
aan de Universiteit Utrecht
op gezag van de rector magnificus, prof. dr. G.J. van der Zwaan,
ingevolge het besluit van het college voor promoties
in het openbaar te verdedigen
op vrijdag 25 april 2014 des middags te 4.15 uur

door

Joyce Helena Catharina Bosmans

geboren op 3 augustus 1986
te Roermond

Promotors:	Prof. dr. L.J. Lourens
	Prof. dr. S.S. Drijfhout
Copromotors:	Dr. F.J. Hilgen
	Dr. E. Tuenter

Contents

1

Introduction

Climate on Earth changes continuously, on time scales varying from decades to millions of years. This thesis focusses on orbitally forced climate changes, occurring on time scales of thousands to hundreds of thousands of years. Gravitational interactions with other planets in the solar system and the Moon cause several quasi-periodic variations in the shape of the Earth's orbit and the tilt of the Earth's rotational axis, described by three orbital parameters. Eccentricity illustrates how much the orbit around the Sun deviates from a perfect circle. Precession describes which season occurs at which location on the orbit, and varies due to rotation of both the rotational axis of the Earth and the eccentric orbit. Obliquity is the angle between the Earth's rotational axis and the perpendicular to the orbital (ecliptic) plane. Together these three parameters controle the seasonal and latitudinal distribution of solar radiation over the Earth. This will be further elaborated on in Section 1.1 of this introduction.

Changes in the distribution of incoming solar radiation (insolation) affect Earth's climate. Therefore eccentricity, precession and obliquity are reflected in sedimentary records from all over the world, in records of different ages and different environments. These records can be interpreted and dated by tuning to a target curve of the principal cycles in the orbital parameters or insolation. In this thesis I examine the causal connection between orbital forcing (also known as the astronomical target curve) and sedimentary cycles using a state-of-the-art climate model. A better understanding of the response of climate to orbital forcing will result in a better understanding of the relation between orbital forcing and orbital cycles recorded in sediments, and therefore a more physical basis for interpreting and dating sedimentary records rather than statistical inferences.

The main focus of this thesis is on the orbital forcing of low-latitude and Mediterranean climate. It has long been recognised, based on sedimentary records, that low-latitude monsoons and Mediterranean climate respond strongly to orbital forcing. Low-latitude insolation is dominated by precession, hence precession as well as its modulator eccentricity are found in many records. Obliquity is often recor-

ded as well, despite the small obliquity-induced variations in low-latitude insolation. Therefore I examine both the impacts of precession and obliquity. A focus on the North-African and Asian monsoons is given in Chapters 3 and 4, respectively. Chapter 5 focusses specifically on the mechanisms through which obliquity affects low-latitude climate. In Chapter 6 the Mediterranean is discussed, where both a monsoonal influence through Nile runoff as well as a high-latitude influence through Atlantic storm tracks are thought to affect the Mediterranean Sea on orbital time scales. These chapters (3-6) all focus on idealised experiments of extreme precession and obliquity forcing. First, in Chapter 2, I discuss an experiment of Mid-Holocene climate, in which the orbital parameters of 6000 years ago are prescribed. For the Mid-Holocene many proxy climate reconstructions as well as many modelling studies are available through the Paleoclimate Modelling Intercomparison Project (PMIP). The Mid-Holocene experiment can therefore be validated against both proxy and modelling results, and act as a validation for the idealised precession and obliquity experiments.

In this introduction I will continue with a more detailed explanation of orbital parameters and orbital forcing (Section 1.1), a brief discussion on paleoclimate modelling, with a focus on the EC-Earth model used in this thesis (Section 1.2), and a summary of the thesis chapters (Section 1.3).

1.1 Orbital forcing

The three orbital parameters that determine the shape of the Earth's orbit and the orientation of the Earth's rotational axis are eccentricity, precession and obliquity. Each oscillates slowly, on time scales of thousands to millions of years due to gravitational interactions with the Moon and other planets in the solar system. It has long been recognised, since the first studies of ice ages in the early 1800s, that orbital (or astronomical) variations in the Earth's orbit have major impacts on Earth's climate. For more background on the history of the astronomical theory of paleoclimates see e.g. Berger (1980); Imbrie and Palmer Imbrie (1986); Paillard (2001); Tuenter et al. (2003). Here I briefly describe eccentricity, precession and obliquity (Sections 1.1.1, 1.1.2, 1.1.3), as well as their impact on insolation (Section 1.1.4).

1.1.1 Eccentricity

The orbit of the Earth around the Sun is an ellipse, with the Sun in one of the foci. The elongation of the ellipse is measured by eccentricity, defined as $e = c/a$, where c is the distance from focus to centre and a is the semi-major axis (Figure 1.1). Currently eccentricity is small, e=0.017, but it varies from nearly circular to $e \approx 0.06$ with periodicities of 100 kyr, 413 kyr and 2 Myr (kyr is thousands of years, Myr is millions of years).

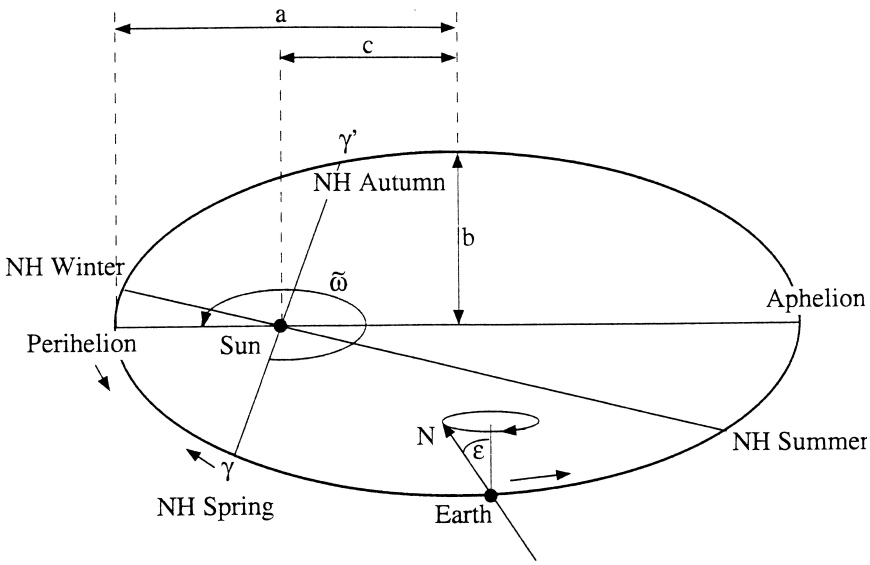

Figure 1.1: Earth's orbit around the Sun. a is the semi-major axis of the ellipse, b the semi-minor axis and c the distance from focus to centre. ε is the tilt or obliquity. $\tilde{\omega}$ is the angle between vernal equinox (γ) and perihelion, a measure of precession. Perihelion and aphelion are the points closest and furthest away from the Sun, respectively. NH (Northern Hemisphere) Spring, Summer, Autumn and Winter indicate vernal equinox, summer solstice, autumn equinox and winter solstice. From Paillard (2001), courtesy of E. Tuenter.

1.1.2 Precession

Due to the eccentricity of the orbit, the equinoxes and solstices do not occur at equal distances from the Sun (Figure 1.1). At present, the summer solstice (northern hemisphere summer) occurs near aphelion, farther away from the Sun than winter solstice (northern hemisphere winter). Therefore the northern hemisphere (NH) seasonal insolation cycle is slightly weaker compared to the insolation cycle on the southern hemisphere (SH).

Over time, the Earth's rotational axis rotates (precesses) around the normal to the orbital plane, causing a clockwise motion of the equinoxes and solstices. Together with the rotation of the ellipse on the orbital plane itself this results in the so-called climatic precession, measured by the angle $\tilde{\omega}$ between vernal equinox (γ) and perihelion (Figure 1.1). Precession is often combined with eccentricity, because the latter modulates the first. When eccentricity is low, there is little difference in the Earth-Sun distance along the orbit, while during high eccentricity the effect of precession is much more pronounced. Therefore a precession parameter $e \sin(\pi+\tilde{\omega})$ is used instead of $\tilde{\omega}$. This parameter is at it's minimum value when perihelion occurs at or near the summer solstice ($\tilde{\omega}$=90°), creating strong NH summer insolation. At so-called maximum precession, summer solstice occurs near aphelion ($\tilde{\omega}$=270°) and NH summer insolation is relatively weak. Precession varies mainly with periods of 23.7, 22.4 and 19 kyr.

Precession and eccentricity do not only affect the location of the seasons along the orbit but also the length of seasons. The second law of Kepler states that a line joining a planet and the Sun sweeps out equal areas during equal intervals of time. On a circular planetary orbit this implies a constant orbital velocity, while on an elliptical orbit the orbital velocity varies depending on the distance to the Sun. Orbital velocity is lower near aphelion (far from the Sun, Figure 1.1) and higher near perihelion (close to the Sun). Therefore length of seasons vary along a precession cycle (e.g. Chen et al., 2010; Joussaume and Braconnot, 1997). In this thesis I keep the present-day calendar in all experiments, i.e. the length of seasons is fixed, because the EC-Earth model does not facilitate the use of a different calendar, and because many other paleoclimate modelling studies also use the present-day calendar, facilitating intercomparison.

1.1.3 Obliquity

Obliquity, or tilt, of the Earth is defined as the angle between Earth's rotational axis and the normal of the orbital plane (ε in Figure 1.1). If there was no tilt, the Suns rays would be perpendicular to the Earth's surface at equator at noon on all days of the year and there would be no seasons (apart from the intra-annual variations in insolation due to eccentricity). However, because of the tilt seasons exist, and the Suns rays are perpendicular to the tropic of Cancer at summer solstice, to the tropic of Capricorn at winter solstice and to the equator at the equinoxes. The obliquity determines the latitudes of the tropics and polar circles. At present, obliquity is

23.45 degrees. It varies between ∼22 to 24.5 degrees, with a dominant period of 41 kyr.

1.1.4 Insolation

Changes in eccentricity, precession and obliquity result in changes in the distribution of insolation over latitudes and seasons. Global annual mean insolation is only affected by eccentricity; when eccentricity is high and the ellipse is elongated, the average Earth-Sun distance is smaller and the global annual mean insolation is higher. Precession affects the seasonality of insolation, more so when eccentricity is high. When for instance northern hemisphere (NH) summer occurs in perihelion, summer insolation is much higher than when NH summer occurs in aphelion, while NH winter insolation is reduced (see Figure 3.1a). Therefore the NH seasonal contrast is increased. At the same time SH seasonality is decreased. Obliquity affects the distribution of insolation between latitudes. At high obliquity, the polar circles move equatorward and both poles receive more insolation during summer, while the tropics move poleward and tropical insolation is reduced (see Figure 3.1b). Obliquity has the same effect on both hemispheres. Annual mean insolation at the poles (tropics) is therefore increased (decreased), but the global annual mean is not affected by obliquity. Details on the orbital forcing in the experiments used in this thesis is given in Section 1.2.2.

When the orbital parameters are given, insolation at any latitude or any time of year can be calculated. Details on this computation can be found in e.g. Berger (1978) and Tuenter (2004) as well as in Appendix A at the end of this thesis, which provides more details on the methods of changing the orbital parameters in the EC-Earth model.

1.2 Paleoclimate modelling with EC-Earth

Many paleoclimate modelling studies have been performed, using a wide range of climate models. There are three main types of climate models, based on complexity. Energy balance models (EBMs), Earth system models of intermediate complexity (EMICs), and general circulation models (GCMs). As complexity increases, computational cost increases as well. In this thesis I use a state-of-the-art GCM, EC-Earth, to perform experiments of the Mid-Holocene as well as idealised precession and obliquity extremes. Here I briefly describe the EC-Earth model (Section 1.2.1), the experimental set-up (Section 1.2.2) and previous model studies, mainly focussing on Tuenter (2004) (Section 1.2.3).

1.2.1 EC-Earth

EC-Earth is an ocean-atmosphere-land general circulation model developed by a European Consortium, with the Royal Netherlands Meteorological Institute (KNMI)

playing a key role. It is mainly used for studies of present-day and future climates within the framework of the Coupled Model Intercomparison Project (CMIP5), and featured in the Fifth Assessment Report of the Intergovernmental Panel on Climate Change (IPCC) (Hazeleger et al., 2010, 2011). In this thesis version 2.2 is used. The basis for EC-Earth is the numerical weather prediction system of the European Centre for Medium range Weather Forecast (ECMWF), the Integrated Forecast System (IFS). EC-Earth therefore has sophisticated parameterizations of small scale atmospheric, hydrological and surface processes which have been tested extensively in operational weather forecasts. Its high resolution (unprecedented in paleoclimate modelling) and the sophisticated parametrizations yield a detailed representation of atmospheric circulation and land surface feedbacks. The atmospheric part of EC-Earth v2.2 is based on IFS cycle 31R1 with a resolution of roughly 1.125°x1.125° (T159) and 62 vertical levels. Its land part consists of H-TESSEL, the Tiled ECMWF Scheme for Surface Exchanges over Land with an improved representation of hydrology (Balsamo et al., 2009). The ocean part consists of NEMO, the Nucleus for European Modelling of the Ocean, version 2 (Madec, 2008), running at a resolution of nominally 1° with 42 vertical levels. NEMO2 was developed at the Institute Pierre Simone Laplace (IPSL) and consists of the Océan Parallélisé version 9 (OPA9) and the Louvain-la-Neuve Sea Ice Model LIM2 (Hazeleger et al., 2011; Sterl et al., 2011). The ocean/ice model is coupled to the atmosphere/land model through the OASIS3 coupler (Valcke and Morel, 2006). Atmospheric or ocean chemistry is not yet included and vegetation and land-ice are kept fixed at present-day values. The experiments discussed here were performed on ECMWF supercomputers.

1.2.2 Experiments

The first two experiments performed with EC-Earth for this thesis are a pre-industrial and mid-Holocene experiment, conform to the framework of the Paleoclimate Model Intercomparison Project (PMIP3, see `http://pmip3.lsce.ipsl.fr/`). In these experiments the orbital parameters of the pre-industrial and mid-Holocene are prescribed and kept fixed, so these are "time slice" or "snapshot" experiments. The orbital parameters, as prescribed by PMIP, are given in Table 1.1 and the orbits are drawn in Figure 2.3. For the pre-industrial experiment the greenhouse gas concentrations are kept fixed at 1850 values (CO_2 284.5 ppmv, CH_4 791.6 ppbv, N_2O 275.7 ppbv). For the Mid-Holocene the values are slightly different (CO_2 280 ppmv, CH_4 650 ppbv, N_2O 270 ppbv), but the resulting difference in radiative forcing is negligible compared with the orbital insolation changes. These orbitally induced insolation changes, based on the orbital parameters shown in Table 1.1, are presented in Figure 4 of Chapter 2.

The orbital extreme experiments do not represent a specific time, but can be considered as idealised experiments. For precession the maximum and minimum values of $e \sin(\pi+\tilde{\omega})$ over the past 1 Myr are selected. During a so-called precession minimum, $e \sin(\pi+\tilde{\omega})$ is at its lowest value due to a combination of high eccent-

Table 1.1: Overview of the orbital configuration in each experiment. ε is the obliquity (tilt, in degrees), $\tilde{\omega}$ is the longitude of perihelion, defined as the angle from the vernal equinox to perihelion in degrees, measured counterclockwise. e is eccentricity (see Figure 1.1). e $\sin(\pi+\tilde{\omega})$ is the precession parameter. Note that for Tmax and Tmin there is no precession because of the circular orbit (e=0)

Experiment	ε (°)	$\tilde{\omega}$ (°)	e	e $\sin(\pi+\tilde{\omega})$
PI	23.45	282.04	0.017	0.017
MH	24.11	180.87	0.019	0.000
Pmin	22.08	95.96	0.056	-0.055
Pmax	22.08	273.50	0.058	0.058
Tmax	24.45	-	0	0
Tmin	22.08	-	0	0

ricity e and perihelion taking place at summer solstice ($\tilde{\omega} \approx 90°$). Therefore the NH receives a relatively large amount of summer insolation, while winter insolation is relatively low due to winter solstice occurring at aphelion. During a precession maximum winter solstice is reached in perihelion ($\tilde{\omega} \approx 270°$), so NH winter insolation is relatively high while summer insolation is relatively low. The insolation difference between the minimum and maximum precession experiments used here (Pmin and Pmax, see Table 1.1) are given in Figure 3.1a. In the Pmin and Pmax experiments obliquity is set to a minimum value of 22.08° and all other boundary conditions, such as greenhouse gas concentrations, vegetation and land ice, are kept fixed at pre-industrial levels.

In the obliquity experiments eccentricity is set to 0, hence e $\sin(\pi+\tilde{\omega})$ is 0 for all values of $\tilde{\omega}$ and the effect of precession is eliminated. In experiment Tmax obliquity is set to 24.45°, increasing insolation on the summer hemispheres. In experiment Tmin obliquity is set to a low value of 22.04°. The insolation difference between these two experiments is given in Figure 3.1b. Just as for the precession experiments, only the orbital parameters vary amongst the experiments and all other boundary conditions are kept fixed at pre-industrial levels.

1.2.3 Previous modelling studies

The first two experiments, of the pre-industrial and mid-Holocene, are performed within the framework of the Paleoclimate Modelling Intercomparison Project (PMIP3). Within PMIP data and model syntheses for the mid-Holocene have been published (e.g. Braconnot et al., 2007a,b) (see also `http://pmip3.lsce.ipsl.fr/`). A comparison with such data and model syntheses is given in Chapter 2, in which the effect of mid-Holocene insolation changes on monsoons is discussed. The EC-Earth PMIP3 experiments are therefore not only a contribution to PMIP but also act as a validation for the idealised precession and obliquity experiments.

Many other time-slice experiments have been performed in order to study orbital forcing of climate, such as for the Eemian ($\sim$ 126 kyr ago) or glacial inception at 115 ka (e.g. Braconnot et al., 2008; de Noblet et al., 1996; Montoya et al., 2000; Prell and Kutzbach, 1987). A brief overview of previous modelling studies can be found in Tuenter (2004).

Studies examining the precession and obliquity forcing separately are rare. In this thesis I mainly compare to the results of the PhD thesis of Tuenter (2004), in which the EC-Bilt model (an EMIC) was used to perform the same precession and obliquity experiments as carried out here. In a study of the North-African monsoon, Tuenter et al. (2003) found that insolation changes at higher latitudes play an important role in the monsoonal response to orbital forcing. Here I revisit the North-African monsoon in Chapter 3 using EC-Earth, in order to investigate whether the conclusions of Tuenter et al. (2003) are reproducible with a more complex climate model (EC-Earth is a GCM, while EC-Bilt is an EMIC with simplifications of atmospheric physics). Using EC-Bilt output and a regional ocean model of the Mediterranean, Meijer and Tuenter (2007) showed that orbital-scale variations in the Mediterranean freshwater budget are strongly influenced by changes in net precipitation over the basin. Other studies claim that Nile runoff is a key factor (e.g. Rossignol-Strick, 1985) or that winter storm tracks and precipitation is important for the Mediterranean freshwater budget (e.g. Kutzbach et al., 2013). I therefore investigate orbitally induced changes in both runoff and precipitation over the basin in Chapter 6.

1.3 Summary of the thesis

This thesis starts with the EC-Earth PMIP time slice experiments of the pre-industrial and mid-Holocene in **Chapter 2**. During the Mid-Holocene (6 ka), the northern hemisphere received more summer insolation than today, intensifying the meridional temperature and pressure gradients. Over North Africa, monsoonal precipitation is intensified through increased landward monsoon winds and moisture advection as well as decreased moisture convergence over the oceans and more convergence over land compared to the pre-industrial simulation. Precipitation also extends further north as the ITCZ shifts northward in response to the stronger poleward gradient of insolation. This increase and poleward extent is stronger than in most previous ocean-atmosphere GCM mid-Holocene simulations. In north-westernmost Africa, precipitation extends up to 35°N. Over tropical Africa, internal feedbacks completely overcome the direct warming effect of increased insolation. Over Asia, monsoonal precipitation during the Mid-Holocene is increased as well, but the response is different than over North-Africa. There is more convection over land at the expense of convection over the ocean, but precipitation does not extend further northward, monsoon winds over the ocean are weaker and the surrounding ocean does not provide more moisture. On the Southern Hemisphere, summer insolation and the poleward insolation gradient were weaker during the Mid-Holocene, result-

ing in a reduced South American monsoon through decreased monsoon winds and less convection, as well as an equatorward shift in the ITCZ. These results corroborate the findings of paleodata research as well as previous model studies, while giving a more detailed account of Mid-Holocene monsoons.

In **Chapter 3** I investigate the response of the North-African monsoon to separate precession and obliquity forcing. Precession has the largest effect on the monsoon, as strongly increased summer insolation results in more intense and more northward heat lows over North-Africa, drawing in stronger south-westerly winds. A stronger South Atlantic high pressure area further enhances the meridional pressure gradient. The strengthened south-westerly monsoon winds carry more moisture landwards from both the northern and southern tropical Atlantic, mostly due to reduced precipitation over the ocean. Upper level circulation patterns are shifted northwards. Obliquity-induced summer insolation changes over the tropics are nearly zero, but they nonetheless result in notable changes in precipitation and monsoonal circulation over North-Africa. The obliquity-induced precipitation changes originate mostly from the tropical Atlantic. Our results provide an explanation for the precession and obliquity signals preserved in the sedimentary record of North-Africa and the Mediterranean, but the mechanisms are different than previously suggested by Tuenter et al. (2003). Using a quasi-geostrophic model of intermediate complexity they found a smaller response to the precession and obliquity forcing, suggesting that northerly moisture transport from higher latitudes plays an important role. In contrast, we argue that moisture transport from both the northern and southern tropical Atlantic, resulting from increased insolation and an increased tropical insolation gradient, is responsible for the precession and obliquity signals in the North-African monsoon.

The Asian monsoons are discussed in **Chapter 4**, based on the same precession and obliquity experiments as in Chapter 3. The focus is on the effect of insolation changes on precipitation and underlying circulation changes in the Indian and the East Asian summer monsoons. The results show increased summer monsoon precipitation at times of increased summer insolation, i.e. minimum precession and maximum obliquity. There is a redistribution of precipitation and convection from ocean to land. Southerly monsoon winds over East Asia are strengthened due to an intensified west-east land-sea pressure gradient. The response of the Indian summer monsoon is more complex, there is no simple intensification of the land-sea pressure gradient. Surface pressure is enhanced over south-east Asia and an Indian Ocean Dipole emerges, with increased precipitation and convection over the western tropical Indian Ocean. During minimum precession there are also increased temperatures and lower surface pressure over the western Indian Ocean, but not during maximum obliquity due to reduced summer insolation over the tropics and southern hemisphere. Evaporation is reduced over the northern Indian Ocean for both minimum precession and maximum obliquity due to reduced wind speeds, which together with increased precipitation over the western Indian Ocean damps the increase of monsoonal precipitation over the continent. The southern tropical Indian Ocean acts as a moisture source for enhanced monsoonal precipitation. Our results

show a direct response of both Arabian Sea upwelling and southern Indian Ocean evaporation, which is in contrast to what proxy climate records suggest.

In Chapters 3 and 4 both precession and obliquity are found to affect the monsoons, despite the near absence of obliquity forcing at low latitudes. Many tropical and subtropical paleoclimate records also reveal a clear obliquity signal. Therefore the influence of obliquity on low-latitude climate is examined in more detail in **Chapter 5**. Several mechanisms have been proposed to explain this influence, such as the remote impact of high-latitude glacials, the remote effect of insolation changes at mid- to high latitudes independent of glacial cyclicity, shifts in the latitudinal extent of the tropics, and changes in latitudinal insolation gradients. Our results show that obliquity-induced changes in tropical climate can occur without high-latitude ice sheet fluctuations. Furthermore, the tropical circulation changes are consistent with obliquity-induced changes in the cross-equatorial insolation gradient, implying that this gradient may be used to explain obliquity signals in low-latitude paleoclimate records instead of the classic 65°N summer insolation curve.

Lastly, in **Chapter 6**, I investigate the precession and obliquity forcing of the freshwater budget of the Mediterranean Sea. There is ample proxy evidence suggesting that at times of enhanced insolation seasonality, i.e. minimum precession and maximum obliquity, the area was wetter and the Mediterranean Sea surface was less saline. This has been attributed to increased Nile runoff as a consequence of a strengthened North-African monsoon, as well as to increased precipitation over the Mediterranean Sea itself. The EC-Earth model results show that both mechanisms have to be considered in the freshwater budget changes, with monsoonal summer runoff being most important for precession and winter precipitation being most important for obliquity. Changes in winter precipitation are related to changes in the air-sea temperature difference, leading to unstable conditions. Winter precipitation changes are not associated to increased storm track activity, identified as a source of enhanced winter precipitation by previous studies. The results show that freshening during minimum precession and maximum obliquity has a strong effect on Mediterranean sea surface salinity and mixed layer depth, thereby likely influencing deep sea circulation and sedimentation at the ocean bottom.

2

Monsoonal response to mid-holocene orbital forcing

Abstract

In this study, we use a sophisticated high-resolution atmosphere-ocean coupled climate model, EC-Earth, to investigate the effect of Mid-Holocene orbital forcing on summer monsoons on both hemispheres. During the Mid-Holocene (6 ka), there was more summer insolation on the Northern Hemisphere than today, which intensified the meridional temperature and pressure gradients. Over North Africa, monsoonal precipitation is intensified through increased landward monsoon winds and moisture advection as well as decreased moisture convergence over the oceans and more convergence over land compared to the pre-industrial simulation. Precipitation also extends further north as the ITCZ shifts northward in response to the stronger poleward gradient of insolation. This increase and poleward extent is stronger than in most previous ocean-atmosphere GCM simulations. In north-westernmost Africa, precipitation extends up to 35° N. Over tropical Africa, internal feedbacks completely overcome the direct warming effect of increased insolation. We also find a weakened African Easterly Jet. Over Asia, monsoonal precipitation during the Mid-Holocene is increased as well, but the response is different than over North-Africa. There is more convection over land at the expense of convection over the ocean, but precipitation does not extend further northward, monsoon winds over the ocean are weaker and the surrounding ocean does not provide more moisture. On the Southern Hemisphere, summer insolation and the poleward insolation gradient were weaker during the Mid-Holocene, resulting in a reduced South American monsoon through decreased monsoon winds and less convection, as well as an equatorward shift in the ITCZ. This study corroborates the findings of paleodata research as well as previous

This chapter is published as: Bosmans, J. H. C., Drijfhout, S. S., Tuenter, E., Lourens, L. J., Hilgen, F. J., and Weber, S. L.: Monsoonal response to mid-holocene orbital forcing in a high resolution GCM, Climate Of The Past, 8, 723740, 2012

model studies, while giving a more detailed account of Mid-Holocene monsoons.

2.1 Introduction

Monsoon systems play a key role in the climate of the tropics and subtropics. Generated by the asymmetric heating of continents and oceans, they are characterised by seasonal reversals in atmospheric circulation and associated precipitation (Hastenrath, 1991; Webster, 1987a; Webster et al., 1998). The strength of monsoons varies on inter-seasonal to inter-decadal timescales, through interactions with different components of the climate system (e.g., Shukla, 1987; Webster, 1987b). Even larger changes occur on time scales of (tens of) thousands of years, when variations in the Earth's orbit induce fluctuations in the distribution of incoming solar radiation on Earth (Berger, 1978). On these orbital time scales, monsoons are primarily controlled by precession, which modifies the seasonality of insolation and, thereby, changes the asymmetric heating of continents and oceans (Ruddiman, 2007).

During the Mid-Holocene, 6000 yr ago (6 ka), the Earth's orbit was different than today. Compared to the present-day orbital configuration, the Mid-Holocene was characterised by relatively strong insolation during boreal summer and autumn, and relatively weak insolation during austral summer and autumn (see Sect. 2.2.2). There is ample evidence from paleodata that the enhanced seasonal cycle of insolation on the Northern Hemisphere coincided with intensified monsoonal summer precipitation, while the reduced seasonal cycle on the Southern Hemisphere corresponded to weaker monsoons. Pollen- and plant macrofossil-based reconstructions of the 6 ka vegetation distribution in North-Africa show that steppe extended up to 23° N in the Sahara, compared to roughly 16° N today, and that lake levels were higher than they are today (e.g. Jolly et al., 1998; Kohfeld and Harrison, 2000; Street-Perrott and Perrot, 1993), indicating increased monsoonal precipitation. Similar paleodata from Asia show that the Indian and East-Asian summer monsoons were enhanced as well (Winkler and Wang, 1993; Yu and Harrison, 1996; Yu et al., 1998). For the Southern Hemisphere, less paleodata are available, but it has been shown from pollen-based biome reconstructions and lake levels that over South America moisture levels were lower at 6 ka (Baker et al., 2001; Marchant et al., 2009; Markgraf, 1993).

The relation between monsoon strength and orbitally-forced changes in insolation was already investigated in some of the earliest paleoclimate model studies (e.g. Kutzbach and Guetter, 1986; Kutzbach and Otto-Bliesner, 1982). These atmosphere-only experiments mostly focused on the Northern Hemisphere, showing that monsoons were enhanced during the Early- and Mid-Holocene in response to relatively strong summer insolation. By adding ocean models and/or dynamic vegetation models, several complex feedbacks that play a role in the climate's response to the initial orbital forcing have been identified (e.g. Dallmeyer et al., 2010; Kutzbach et al., 1996; Liu et al., 2004; Marzin and Braconnot, 2009b; Ohgaito and Abe-Ouchi, 2007; Zhao and Harrison, 2012; Zhao et al., 2005). Many of these modelling studies have been performed within the framework of PMIP, the Paleocli-

mate Modelling Intercomparison Project (Braconnot et al., 2000; Joussaume et al., 1999). In the first phase of PMIP, atmospheric general circulation models (GCMs) were used to simulate Mid-Holocene climate, applying 6 ka orbital forcing and pre-industrial greenhouse gas concentrations while keeping all other boundary conditions (sea surface temperatures, ice sheets, vegetation and land surface properties) constant at present-day values. Phase 2 of PMIP included dynamic ocean models, and for some models interactive vegetation as well (Braconnot et al., 2007a,b). The EC-Earth experiments discussed in this study are a contribution to the third phase, PMIP3, in which improved and higher-resolution models are used to further investigate the effect of Mid-Holocene orbital forcing and internal climate feedbacks.

The earlier model studies mentioned above have shown that on the Northern Hemisphere (NH) the increased summer insolation during the Mid-Holo-cene enhances the thermal low over the continents, which strengthens the land-sea pressure gradients, thereby reinforcing monsoon winds and bringing more moisture landward. This results in an intensified monsoon circulation and, over North-Africa, a poleward shift in precipitation. The opposite occurs on the Southern Hemisphere (SH), resulting in weaker monsoons.

Although the mechanisms of monsoon intensification/weakening are generally agreed upon, several questions remain. Some of these questions concern the spatial pattern of climate response to the orbital forcing, as paleoclimate models generally have a coarse resolution and paleodata is sparse. Another important question is what mechanism causes the northward extension of precipitation over North Africa, which is evident from paleodata, but which models fail to reproduce (Joussaume et al., 1999), even if ocean and vegetation feedbacks are included (Braconnot et al., 2007a). Besides coarse resolution, this discrepancy could also be attributed to models' sensitivity to the parameterization of clouds, atmospheric dynamics, the hydrological cycle and land-surface interactions. Several studies have shown that monsoons are better resolved when the resolution, and consequently the representation of topography, is increased (Gao et al., 2006; Kobayashi and Sugi, 2004; Sperber et al., 1994; Zhou and Li, 2002), while results remain susceptible to changes in model's parameterization (Bonfils et al., 2001; Lal et al., 1997; Masson and Joussaume, 1997; Vamborg et al., 2011).

To re-examine the monsoonal response to Mid-Holocene orbital forcing using a state-of-the-art modelling tool, we present results of a Mid-Holocene experiment with the EC-Earth climate model (Hazeleger et al., 2010, 2011). EC-Earth is an atmosphere-ocean coupled model with a high resolution (T159) compared with PMIP2 and PMIP3 models. EC-Earth has sophisticated parameterizations of small-scale atmospheric, hydrological and surface processes which have been tested extensively in operational weather forecasts. We believe that the high resolution and reliable, sophisticated parameterizations will yield a more detailed representation of monsoons and related circulation systems such as the Inter Tropical Convergence Zone (ITCZ). We are particularly interested in the spatial distribution of Mid-Holocene monsoonal precipitation and the atmospheric dynamics that explain these precipitation patterns. Many studies have described changes in precipitation (sum-

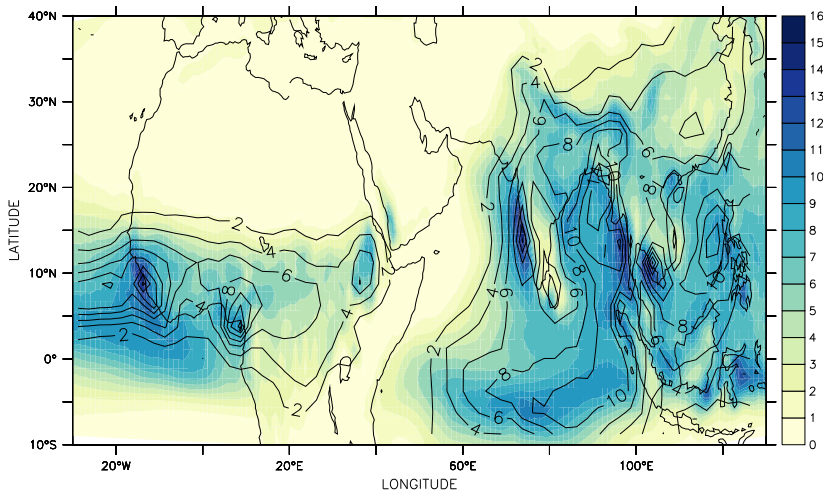

Figure 2.1: JAS precipitation (mm/day) from the EC-Earth pre-industrial experiment (colour) and the CPC Merged Analyses of Precipitation data set (contours, Xie and Arkin 1997).

marised in Braconnot et al., 2007a; Liu et al., 2004), but only few studies have looked into the atmospheric dynamics that cause these changes (Marzin and Braconnot, 2009a; Patricola and Cook, 2007; Su and Neelin, 2005; Texier et al., 2000).

This paper is organised as follows: Sect. 6.2 describes the EC-Earth model and the experimental set-up. Changes in monsoonal precipitation and the associated atmospheric dynamics (temperature and pressure gradients, wind fields, moisture advection and vertical velocity) are examined in Sect. 5.3. We focus on three monsoon regions: North-Africa, Asia (India and South-East Asia) and South-America. Section 2.4 provides a discussion of the EC-Earth Mid-Holocene experiment and a comparison to previous modelling results and paleodata studies. A conclusion is given in Sect. 2.5.

2.2 Model and experiment set-up

2.2.1 The model: EC-Earth and pre-industrial results

EC-Earth is a fully coupled ocean-atmosphere GCM (Global Climate Model). It is used for exploratory studies of feedbacks in the climate system as well as for future climate projections as part of CMIP5 (Hazeleger et al., 2010, 2011). The atmospheric part is based on the Integrated Forecasting System (IFS), cycle 31R1, of the European Centre for Medium-range Weather Forecast (ECMWF). It runs at T159 horizontal resolution (roughly $1.125^\circ \times 1.125^\circ$) with 62 vertical levels. IFS has a

new convection scheme (Bechtold et al., 2008) and the new land surface scheme H-TESSEL, which includes surface runoff (Balsamo et al., 2009). The ocean component is the NEMO model, version 2, which runs at a horizontal resolution of nominally 1° with 42 vertical levels and incorporates the sea-ice model LIM2 (Madec, 2008; Sterl et al., 2011). The ocean/ice and atmosphere are coupled through the OASIS3 coupler (Valcke and Morel, 2006). The resolution of the ocean in EC-Earth is comparable to PMIP2 and PMIP3 models, but the resolution of the atmospheric component is higher than all PMIP2 models (at most $2.8^\circ \times 2.8^\circ$, Braconnot et al., 2007a) and is amongst the highest of PMIP3 models (only two of which run at a comparable resolution, see `http://pmip3.lsce.ipsl.fr`).

Hazeleger et al. (2010) demonstrate that EC-Earth performs well compared to CMIP3 models (see their Fig. 2). The model also captures inter-annual variability very well, as shown by the spatial and temporal variability of the modelled El Niño Southern Oscillation (see Hazeleger et al., 2010, Fig. 3). More importantly, monsoons are represented well in EC-Earth, both temporally and spatially. Figure 2.1 shows that EC-Earth captures the spatial pattern of July-August-September precipitation over Africa and Asia very well. Furthermore, a comparison between EC-Earth, CMAP and PMIP2 models, presented in Fig. 2.2, illustrates that the temporal patterns of monsoon precipitation is also resolved well in EC-Earth.

2.2.2 Experimental set-up: insolation forcing and boundary conditions

Here we study two time-slice experiments performed with EC-Earth: a pre-industrial and a Mid-Holocene experiment, both at the T159L62 resolution (in the atmosphere). We use the boundary conditions as prescribed by PMIP, see `http://pmip3.lsce.ipsl.fr/`. This means that CMIP5 pre-industrial boundary conditions are applied for the pre-industrial (PI) experiment, including greenhouse gas concentrations from 1850 (CO_2 284.5 ppmv, CH_4 791.6 ppbv, N_2O 275.7 ppbv). For the Mid-Holocene (MH) experiment the greenhouse gas concentrations were set to pre-industrial values slightly different from those of 1850 (CO_2 280 ppmv, CH_4 650 ppbv, N_2O 270 ppbv), but the resulting difference in radiative forcing is negligible compared to the orbitally induced changes in insolation. The orbital parameters are given in Table 1.1. During the Mid-Holocene, the tilt of the Earth (obliquity) was larger and the orbit was slightly more eccentric than at present. The difference in MH and PI insolation, however, is mostly due to precession. The position closest to the Sun (perihelion) was reached around the time of the autumnal equinox, instead of near the winter solstice at present (Fig. 2.3). This causes a larger seasonal cycle of insolation on the Northern Hemisphere and a smaller seasonal cycle on the Southern Hemisphere, shown in Fig. 2.4.

The initial conditions were taken from EC-Earth's CMIP5 pre-industrial experiment, which was run for 730 yr (Hazeleger et al., 2011). The PI and MH experiments discussed here were both performed with version 2.2, including the equations

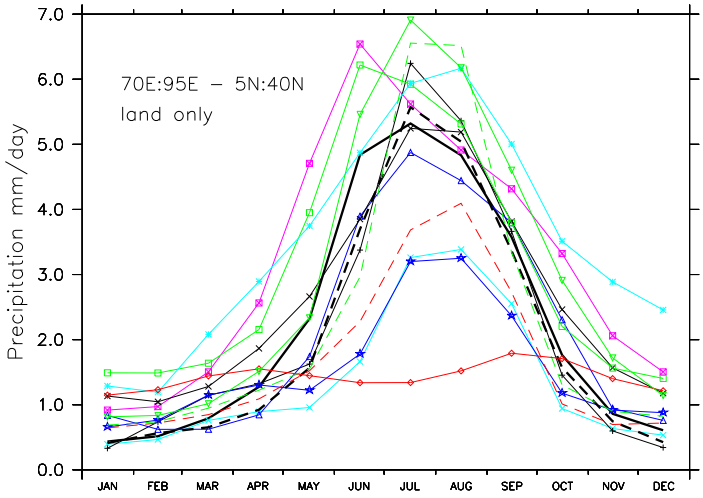

Figure 2.2: Precipitation over India and the Himalaya (mm day^{-1}, 70° E:95° E, 5° N:40° N land only). The thick black solid line is for the EC-Earth pre-industrial experiment, the thick black dashed line is for CMAP (Xie and Arkin, 1997). The other lines are for PMIP2 ocean-atmosphere models (pre-industrial). The colours and symbols are the same as in Braconnot et al. (2007a); see their Fig. 10 for a legend and their Table 2 for model characteristics and references. Two models that are included here are not included in Braconnot et al. (2007a): GISS modelE (green dashes, Schmidt et al., 2006) and CSIRO (red dashes, Gordon et al., 2000).

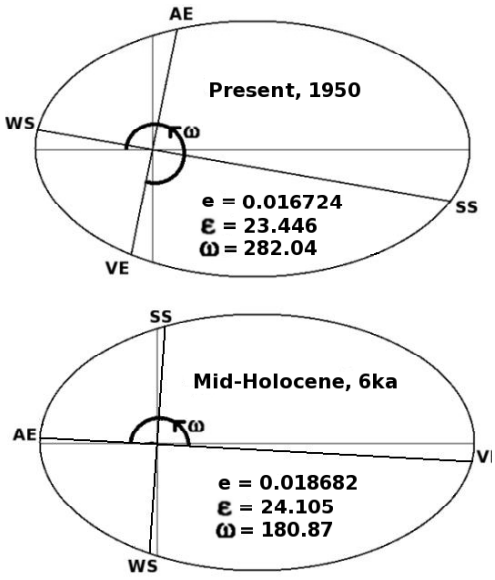

Figure 2.3: Present and Mid-Holocene orbit. WS and SS are winter and summer solstice, VE and AE are vernal and autumnal equinox, e is eccentricity, ε is obliquity and ω is the longitude of perihelion, defined as the angle between the vernal equinox and perihelion, measured counterclockwise (figure drawn after Joussaume and Braconnot, 1997).

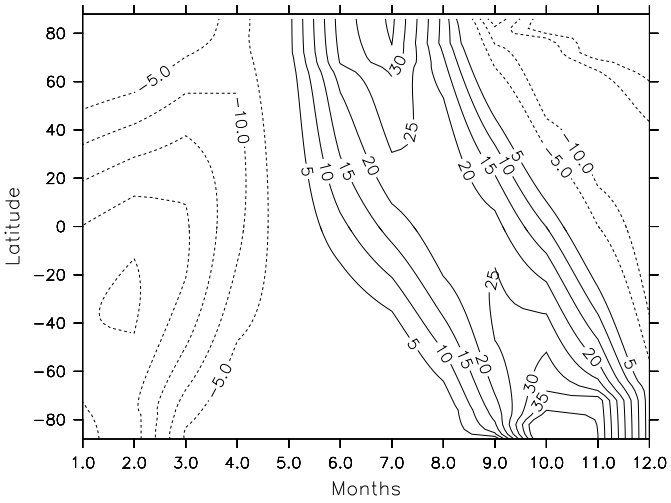

Figure 2.4: Insolation difference Mid-Holocene (MH) minus Pre-Industrial (PI) in W m^{-2}, calculated using the equations of Berger (1978).

of Berger (1978).

The EC-Earth model is computationally very expensive because of its complexity and high resolution. The PI and MH time-slice experiments were run for 50 yr, of which the last 40 yr are used. This is sufficiently long for atmospheric, ocean surface and land processes that are of interest to monsoon dynamics to equilibrate to the changed insolation; trends in surface air temperature, sea surface temperature, the surface heat flux, the top-of-atmosphere net flux and precipitation are shown in Fig. 2.5. Also, we calculated the globally averaged tendency term of surface air temperature, dT/dt, which is near-zero (on the order of 10^{-9} K yr^{-1}) and shows no trend in the pre-industrial and Mid-Holocene experiments (not shown).

The EC-Earth model does not (yet) include dynamic vegetation. Vegetation in the MH experiment is the same as in the PI experiment, hence vegetation feedbacks are not included in this study. We set the date of vernal equinox to 21 March and use the present-day calendar, which introduces some errors, mainly in Mid-Holocene autumn insolation, because we do not take into account changes in seasonal length and the dates of equinoxes and solstices, induced by precession (Joussaume and Braconnot, 1997). However, all PMIP experiments use the present-day calendar with the vernal equinox as a reference date in order to facilitate model intercomparison.

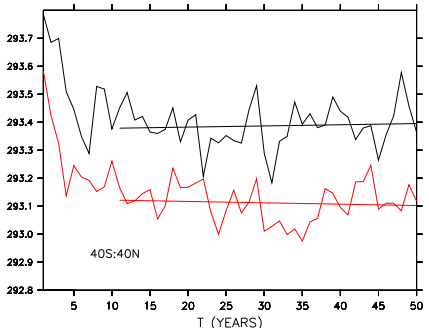

(a) Surface air temperature, K

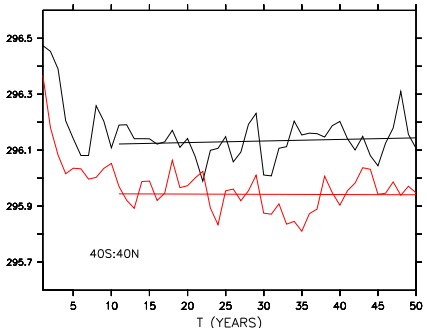

(b) Sea surface temperature, K

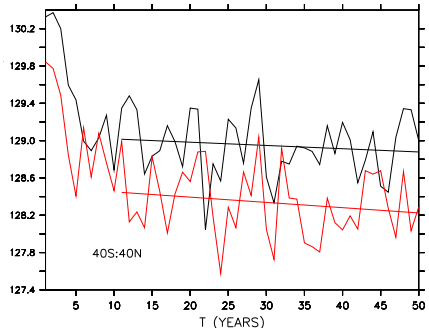

(c) Surface sensible and latent heat flux, W/m^2

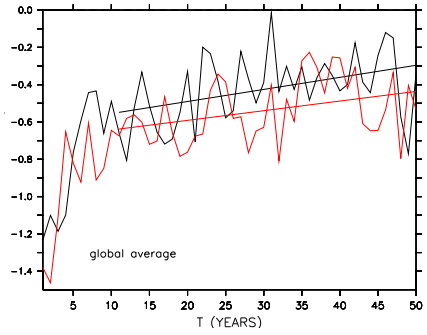

(d) TOA net flux (TSR + OLR), W/m^2

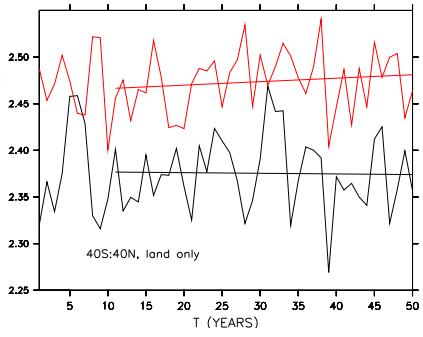

(e) Precipitation, mm/day

Figure 2.5: Trends in the pre-industrial (black) and Mid-Holocene (red) experiments: **(a)** surface air temperature, **(b)** sea surface temperature, **(c)** sum of the surface sensible and latent surface heat flux, **(d)** net TOA flux (top of atmosphere net short- and longwave) and **(e)** precipitation. **(a)**, **(b)**, **(c)** and **(e)** are 40° S:40° N zonal and annual averages, **(e)** is over land only, and **(d)** shows a global annual average. The trend over the last 40 years has been drawn in all figures for both experiments.

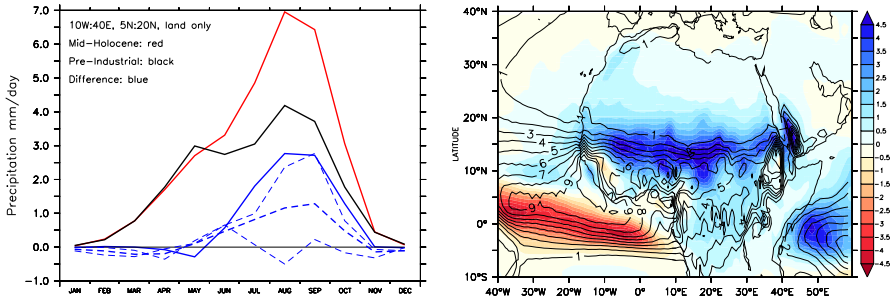

(a) Monthly precipitation over North-Africa, mm/day

(b) JAS precipitation over North-Africa, mm/day

Figure 2.6: (a) Precipitation (mm day^{-1}) for PI (black), MH (red) and difference MH-PI (blue) throughout the year. The dashed blue lines are differences in the PMIP2 models: the thick dashed blue line is the average of 12 PMIP2 models (see Fig. 2.15 for references). The thin dashed blue lines are individual PMIP2 model results with the largest and smallest changes for North-Africa in JAS. **(b)** The spatial pattern of precipitation differences in JAS. Colours indicate MH-PI differences, contours are absolute PI values.

2.3 Results

In this section, we describe how the change in insolation affects summer monsoonal precipitation through temperature and pressure gradients, wind fields, moisture advection and vertical motion. Section 2.3.1 focuses on the North-African monsoon, Sect. 2.3.2 on the Indian and East-Asian monsoons and the South American monsoon is assessed in Sect. 2.3.3. For North Africa and Asia we focus on the months July-August-September (JAS), when insolation changes over the NH tropics are largest. In these three months the precipitation increase is largest as well, but for Asia the absolute precipitation amounts are highest in June-July-August. For South America, we focus on JFM, when the SH insolation decrease is largest, as is the precipitation decrease, while absolute precipitation amounts are highest in DJF. In the figures with colour scales the MH minus PI difference is shown, with the PI climatology given in contours, unless stated otherwise.

2.3.1 The North-African monsoon

During the Mid-Holocene, precipitation over North-Africa was higher than during the pre-industrial, with the largest increase occurring in late summer (Fig. 2.6a), centred around 10–15° N (Fig. 2.6b). Precipitation over the equatorial Atlantic is reduced, while over land precipitation is not only increased, but also extended further poleward.

To investigate the cause of the precipitation changes, we first examine the changes in surface air temperature, pressure and wind. The increased summer insolation gen-

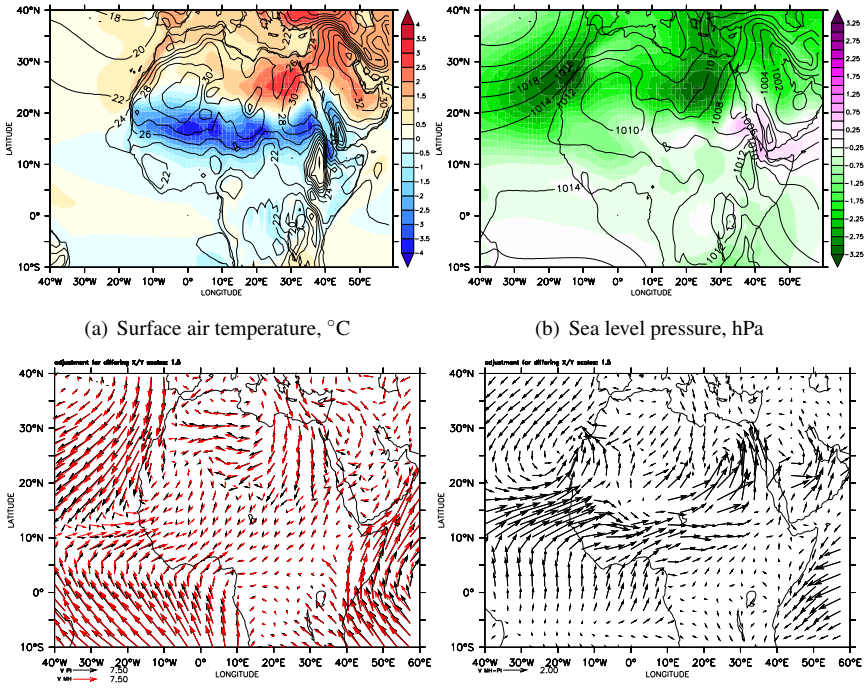

(a) Surface air temperature, °C

(b) Sea level pressure, hPa

(c) Surface wind field, PI (black), MH (red), m/s

(d) Surface wind difference, MH - PI, m/s

Figure 2.7: MH-PI difference in JAS surface air temperature – **(a)**, °C – and sea level pressure – **(b)**, hPa; contours are PI values, colours indicate differences between MH and PI. **(c)** Shows the PI surface wind field (black) and the MH surface wind field (red), unit length is 7.5 m s^{-1}, **(d)** gives the difference between the MH and PI wind field, unit length is 2.0 m s^{-1}.

erally results in higher temperatures in the atmosphere and at the surface. Over a large part of North Africa, however, feedbacks from monsoon intensification cause surface air temperatures to decrease (Fig. 2.7a). Increased cloud cover reduces the surface downward shortwave radiation by $24\,\mathrm{W\,m^{-2}}$ (averaged over 20° W:40° E, 5° N:25° N, land only). The surface latent heat flux to the atmosphere is enhanced by $13\,\mathrm{W\,m^{-2}}$, so increased evaporation over this area also acts to cool the surface. These changes in the surface heat budget are only partly balanced by an increase in surface downward longwave radiation ($13\,\mathrm{W\,m^{-2}}$), a decreased sensible heat flux ($11\,\mathrm{W\,m^{-2}}$) and a decreased surface upward shortwave radiation ($6\,\mathrm{W\,m^{-2}}$). This leaves a deficit of $7\,\mathrm{W\,m^{-2}}$ $(-24-13+13+11+6)$ which explains the surface cooling. The changes in the surface energy fluxes (summarised in Table 3.1) are of the same order of magnitude as the insolation forcing (Fig. 2.4) and more than offset the direct effect of increased insolation, indicating the importance of internal feedbacks in the monsoonal response to insolation changes. Another feedback mechanism operates on the sea surface temperatures. These remain relatively cool during summer south of 15° N, not only because of the delayed response of the ocean due to its large heat capacity, but also because stronger surface monsoon winds act to cool the ocean surface through increased evaporative cooling and upwelling (not shown). This wind-evaporation-SST feedback further enhances the ocean-land temperature gradient (e.g. Zhao et al., 2005).

Changes in surface pressure are more uniform (Fig. 2.7b). Increased insolation results in lower surface pressure over nearly all of North Africa, especially over the northern Sahara, where the surface air temperature increase is largest and thermal lows arise (Fig. 2.7a and b). These changes in the pressure gradient are strongly modified by the temperature and precipitation changes and are, therefore, not a passive response to the increased insolation, but involve the feedbacks that lower the surface air temperature over monsoonal North Africa. The enhancement of the meridional pressure gradient intensifies the southerly and south-westerly monsoon winds over the Gulf of Guinea and the equatorial Atlantic, and monsoon winds over the continent extend further north (Fig. 2.7c and 2.7d). At 15–20° N, the northerly trade winds over the Atlantic are more eastward (i.e., landward), and the northerly winds over the coast at 20–30° N are weaker in the MH. This is related to the reduced surface pressure at 25° N, 15° W (Fig. 2.7b), which creates a cyclonic pattern in the wind difference field (Fig. 2.7d). The pressure reduction in the north-eastern Sahara, at 20–30° N, results in weaker northerly winds over this area.

The next question is where the moisture originates that is necessary to sustain the increased precipitation over North Africa. The precipitation decrease over the equatorial Atlantic (Fig. 2.6b) and the stronger landward winds over this area (Fig. 2.7d) strongly suggest that the equatorial Atlantic is the source for increased precipitation over North Africa. This is further supported by changes in evaporation over the ocean, shown in Fig. 2.8a. South of 10° N–15° N, enhanced south-westerly winds lead to more evaporation over the ocean, cooling the ocean surface. This wind-evaporation-SST feedback, in addition to the precipitation decrease over the equatorial Atlantic, makes more moisture available for transport to the contin-

ent. Over land, evaporation is increased north of 15° N, where the MH precipitation increase is relatively large because there is virtually no precipitation in the PI (Fig. 2.6b). Between 5° N and 15° N, where the relative precipitation increase (not shown) is smaller than north of 15° N, evaporation is decreased in association with lower temperatures in the MH. The small and partly negative changes in evaporation over North Africa indicate that local recycling cannot explain the precipitation increase. A simple calculation of $(\Delta P - \Delta E)/\Delta P$, where Δ is the MH-PI difference, shows that for 20° W:40° E, 5° N:25° N (land only) 77 % of the precipitation increase during JAS is due to moisture advection from outside this area. Given the wind pattern, the moisture needed to sustain the increased precipitation over the continent must, therefore, come from the Atlantic Ocean. Moisture advection (defined here as $\vec{Q}$, the mass-weighted vertical integral of the product of specific humidity $\vec{q}$ and the horizontal wind vector $\vec{v}$, based on 12-hourly model output) is shown in Fig. 2.8b (MH-PI difference). There is more moisture advection towards the continent between 10° N and 20° N, south of 10° N increased landward moisture advection occurs in the lower atmosphere (not shown). This is in agreement with the stronger landward surface winds (Fig. 2.7d) and enhanced evaporation in the tropical North Atlantic (Fig. 2.8a). The moisture transport from the east of the Azores High into the north-westernmost part of Africa is reduced (Fig. 2.8b), despite intensified northerly surface winds over the ocean. At the coast, surface winds become more offshore (Fig. 2.7d). Over land, southerly winds near 0° W–10° W, 20° N are enhanced and moisture advection from the south is increased up to 30° N. The precipitation increase in western Africa north of 20° N could, therefore, be linked to monsoonal precipitation, instead of increased moisture advection from the subtropical Atlantic. Local recycling is also an important factor here, because moisture advection accounts for only 33 % of the precipitation increase over 15° W:0° E, 25° N:35° N (land only). Both the moisture advection and local recycling lead to enhanced moisture convergence (indicated by net precipitation, P-E) over this area (Fig. 2.8b). In line with the results presented so far, moisture convergence over the equatorial Atlantic decreased during the Mid-Holocene, in favour of increased moisture convergence over land.

These changes in moisture advection and convergence are linked to changes in the circulation patterns over North Africa. Other model studies have already indicated that the ITCZ shifts poleward when the insolation forcing is positive (Braconnot et al., 2007a; Joussaume et al., 1999; Marzin and Braconnot, 2009a). Figure 2.8c shows vertical motion averaged over 40° W:40° E, which indicates the location of the ITCZ. Upward motion is weaker over the southern half of the pre-industrial ITCZ, and stronger in the northern half, demonstrating that the ITCZ was located more poleward during the Mid-Holocene. The weakening and northward shift on the southern half of the ITCZ occurs mostly over the ocean, while the stronger upward motion and northward shift on the northern side occurs mostly over land. This spatial pattern is analogous to the changes in vertical motion (not shown), with reduced upward motion and moisture convergence over the ocean and increased upward motion and moisture convergence over land (see Fig. 2.8b). The decrease

in convection centred at 15–20° N, 925 hPa is caused by the northward shift of the convection maximum located here during the PI (contours in Fig. 2.8c).

Over the desert north of the monsoonal area, the downward velocity that characterises this area as the subsidence zone of the Hadley circulation over North Africa is reduced in the MH as the ITCZ shifts northward (Fig. 2.8c). This results in a weakened Saharan High, a high pressure area in the upper levels (not shown) overlaying the surface low (Fig. 2.7b). Outflow on the southern side of this pressure ridge is forced westward through the Coriolis force, forming the African Easterly Jet (AEJ, Cook, 1999). In the EC-Earth pre-industrial experiment this jet is situated at approximately 700 hPa, 10–15° N. The weakening of the Saharan High during the Mid-Holocene yields a weaker AEJ (Fig. 2.8d) and, hence, weaker outflow of air from North Africa to the Atlantic at this altitude. Together with increased surface westerlies this enhances the moisture content over Northern Africa.

2.3.2 The Indian and East-Asian monsoons

The model results demonstrate that monsoonal precipitation in Asia was also enhanced as a result of the increased insolation during July, August and September in the Mid-Holocene (Fig. 2.9a and b). The precipitation increase is largest just south of the Himalayas, where precipitation maxima also occur in the pre-industrial experiment (contour lines in Fig. 2.9b). The intensified Asian monsoon did not move further northward, as it did over North-Africa. Precipitation increases over land are balanced by precipitation decreases over most of the Indian Ocean and the South Chinese Sea (Fig. 2.9b).

Changes in surface air temperature over India and South-East Asia are small (less than 0.5 °C, Fig. 2.10a), because the direct warming effect of insolation is offset by increased cloudiness. Similar to North Africa, the SSRD is lower and the STRD is increased, but the changes are relatively small (see Table 3.1). Further north, over central Asia, temperatures do increase as a result of increased insolation. This reduces the surface pressure north of 20° N (Fig. 2.10b), reinforcing the meridional pressure gradient north of 20° N. As a result, the monsoon winds into Asia over the Arabian Sea, the Bay of Bengal and the South China Sea (Fig. 2.10c and d) are stronger in the Mid-Holocene. Over land, northerly winds are stronger in the monsoonal areas, but they do not penetrate further northward because they are hindered by the Himalayas, which are represented well by the model because of its high resolution. Winds south of 15° N are weaker during the MH, associated with the increase of surface pressure over 10–20° N (Fig. 2.10b), which weakens the meridional pressure gradient between the equator and 15° N. This pressure increase is connected to an intensified high pressure system over the west Pacific (not shown) and contributes to the northward flow along the coasts of eastern India and Vietnam (Zhao et al., 2005).

The increase of the monsoon winds over the Asian coasts is a plausible explanation for the increased precipitation over India and South-East Asia. However, the surrounding oceans do not supply more water during the Mid-Holocene; evapor-

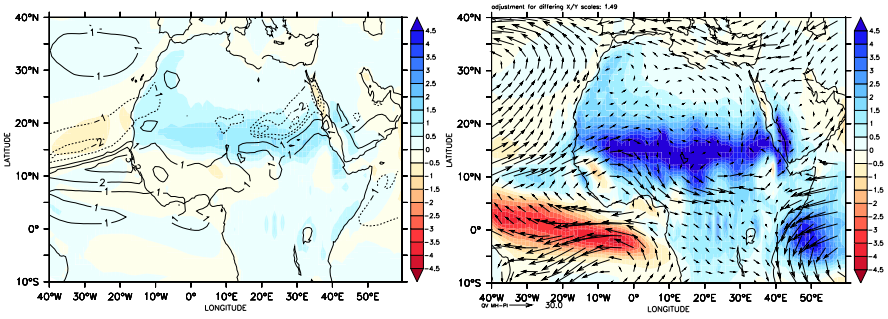

(a) Evaporation, mm/day (colours) and wind speed, m/s (contours), both are MH-PI differences

(b) P-E, mm/day (colours) and moisture advection $\boldsymbol{Q}$, kg m^{-1} s^{-1} (vectors), both are MH-PI differences

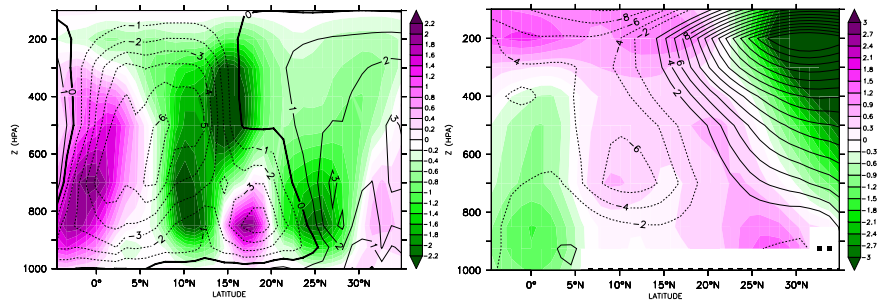

(c) Vertical velocity (omega) 40°W:40°E, hPa/s

(d) Zonal wind, 0°E, m/s

Figure 2.8: MH-PI JAS differences in **(a)** evaporation (colours, mm day^{-1}) and wind speed (contours, m s^{-1}), **(b)** P-E (colours, positive values indicating moisture convergence, in mm day^{-1}) and moisture advection $\vec{Q}$ (vectors, vector length is 30 kg ms^{-1}), **(c)** vertical velocity in 10^{-2} Pa s^{-1}, averaged over 40° W:40° E (negative values indicating upward motion), **(d)** zonal wind velocity in m s^{-1} at the meridian (0° E), positive values are westerly winds. White areas indicate where the pressure levels are below the surface. In panels **(c)** and **(d)**, colours give the MH-PI difference, contours indicate the PI climatology, and height is given in pressure coordinates, 500 hPa is approximately 5 km.

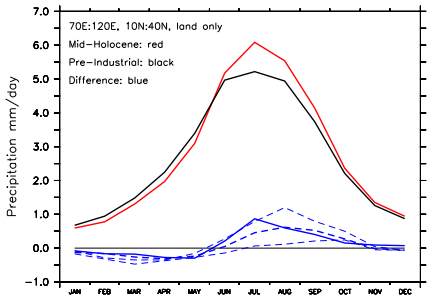

(a) Monthly precipitation over Asia, mm/day

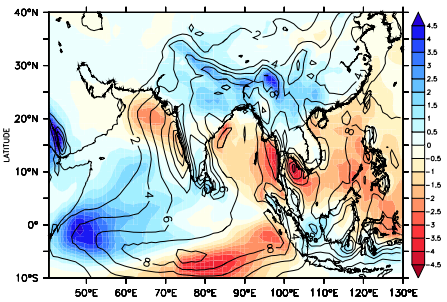

(b) JAS precipitation over Asia, mm/day

Figure 2.9: **(a)** Precipitation (mm day^{-1}) for PI (black), MH (red) and difference MH-PI (blue) throughout the year. The dashed blue lines are differences in the PMIP2 models: the thick dashed blue line is the average of 12 PMIP2 models (see Fig. 2.15 for references). The thin dashed blue lines are individual PMIP2 model results with the largest and smallest changes for Asia in JAS. **(b)** The spatial pattern of precipitation differences in JAS. Colours indicate MH-PI differences, contours are absolute PI values.

ation is decreased over most of the ocean (Fig. 2.11a). Between the equator and 10–15° N this can be related to decreased wind speeds. Over the areas close to the continent where winds are increased, other feedbacks dominate. Over the Arabian Sea, stronger winds cool the surface through increased upwelling, while over the Bay of Bengal increased river runoff freshens the surface waters and reduces the mixed layer depth (not shown), which reduces evaporation. The only ocean region that provides more moisture to the monsoon flow into Asia is the Indian Ocean south of the equator, where wind speeds and evaporation are increased (Fig. 2.11a). Over land, in the region where precipitation increases are largest, evaporation changes are mostly negative (Fig. 2.11a). Also, calculating $(\Delta P - \Delta E)/\Delta P$ for 70:100° E, 10:35° N (land-only) reveals that 99 % of the precipitation increase is due to moisture advection, local recycling does not play a role.

The increased evaporation in the southern Indian Ocean is small compared to the precipitation increase over land. Therefore, the redistribution of precipitation from ocean to land (Fig. 2.9b) must play an important role. This is in agreement with changes in the vertical motion (Fig. 2.11b): increased moisture convergence and precipitation over the continent is linked to larger upward motions. Over most of the ocean upward motion is weakened, which is in agreement with the higher surface pressure seen in Fig. 2.10b, resulting in less precipitation. The western equatorial Indian Ocean receives more precipitation in the MH because of the weakened monsoon southerlies (Fig. 2.10c and d) and increased convection.

Table 2.1: PI, MH and difference values of the surface energy budget terms (in $\mathrm{W\,m^{-2}}$), precipitation and evaporation (in $\mathrm{mm\,day^{-1}}$), over land points only, for North Africa (20° W:40° E, 5° N:25° N, JAS), Asia (60° E:120° E, 10° N:30° N, JAS) and South America (40° W:80° W, 10° S:40° S, JFM). SSRD is surface shortwave radiation downward, STRD is surface thermal (longwave) radiation downward, SLHF is surface latent heat flux, SSHF is surface sensible heat flux, SSRU is surface shortwave radiation upward, STRU is surface thermal (longwave) radiation upward. Positive values of the energy budget terms indicate a flux from the atmosphere towards the surface.

	North Africa			Asia		
	PI	MH	MH-PI	PI	MH	MH-PI
SSRD	252.7	228.6	−24.1	191.2	188.3	−2.9
STRD	369.6	382.3	12.7	382.2	386.2	4.0
SLHF	−52.2	−65.3	−13.1	−86.2	−86.2	0.0
SSHF	−48.1	−37.1	11.0	−27.2	−26.3	0.9
SSRU	−66.6	−60.4	6.2	−31.3	−30.7	0.6
STRU	−454.5	−447.2	7.3	−427.0	−428.0	−1.0
Precip	3.02	4.98	1.96	5.69	6.50	0.81
Evap	1.80	2.26	0.46	2.98	2.98	0.0

	South America		
	PI	MH	MH-PI
SSRD	225.7	221.2	−4.5
STRD	362.2	356.4	−5.8
SLHF	−90.4	−86.5	3.9
SSHF	−41.9	−40.9	1.0
SSRU	−33.8	−33.3	0.5
STRU	−420.1	−416.0	4.1
Precip	5.62	5.17	−0.45
Evap	3.23	3.08	−0.15

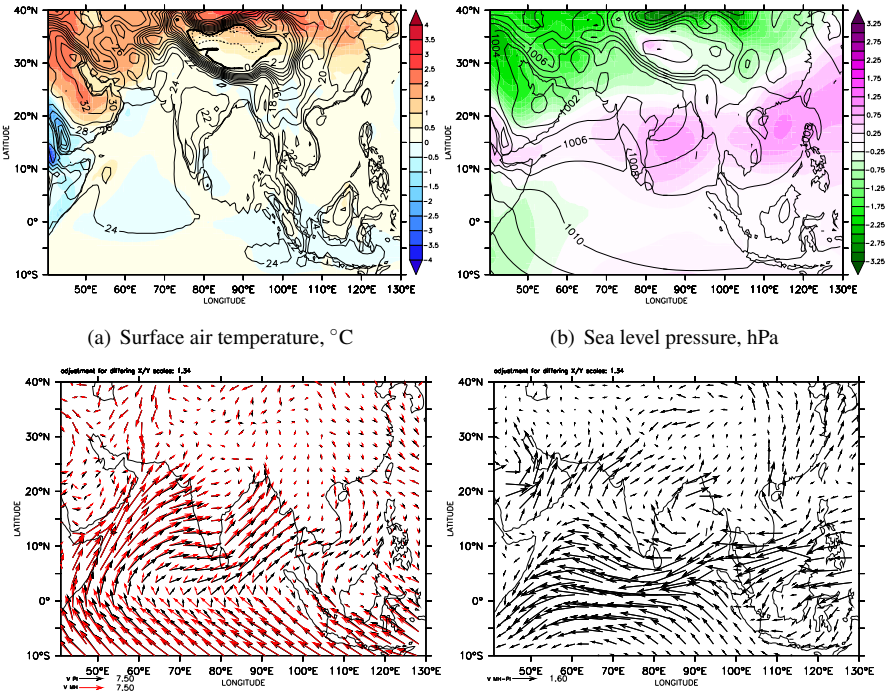

(a) Surface air temperature, °C

(b) Sea level pressure, hPa

(c) Surface wind field, PI, m/s

(d) Surface wind difference, MH - PI, m/s

Figure 2.10: MH-PI difference in JAS surface air temperature – **(a)**, °C – and sea-level pressure – **(b)**, hPa; contours are PI values, colours indicate differences between MH and PI. **(c)** Shows the PI surface wind field (black) and the MH surface wind field (red), unit length is 7.5 m s^{-1}, **(d)** gives the difference between the MH and PI wind field, unit length is 1.6 m s^{-1}.

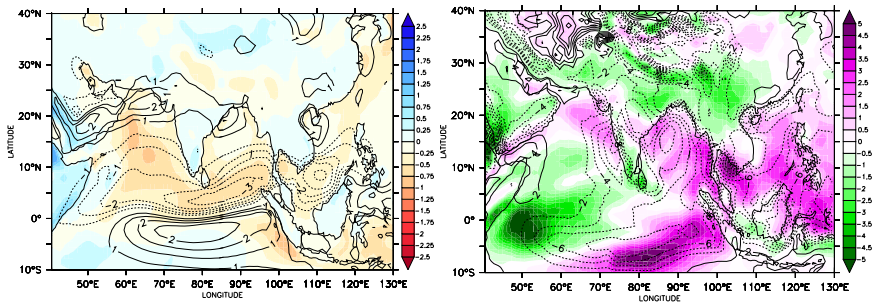

(a) Evaporation, mm/day (colours) and wind speed, m/s (contours), both are MH-PI differences

(b) Vertical velocity (omega) at 500hPa, hPa/s

Figure 2.11: MH-PI JAS differences in **(a)** evaporation (colours, mm day^{-1}) and wind speed (contours, m s^{-1}), **(b)** vertical velocity at 500 hPa in 10^{-2} Pa s^{-1} (negative values indicating upward motion), contours are PI values. 500 hPa is approximately 5 km.

2.3.3 The South-American monsoon

The Southern Hemisphere received less insolation during the Mid-Holocene summer (see Fig. 2.4). The change in insolation in the tropics and subtropics during summer is of the order 20 W m^{-2} on both hemispheres. On the SH, the insolation decrease is partly offset towards the South Pole by increased obliquity, which acts to increase summer insolation on both hemispheres. Therefore, the summer insolation gradient from equator to pole is weaker on the SH during the Mid-Holocene, while on the NH it is stronger.

The decreased insolation during the SH summer weakens the South-Ame-rican monsoon. Figure 2.12a shows a decrease in precipitation in December–April, especially in a northwest-southeast band over the continent (Fig. 2.12b, JFM). Over the Atlantic, precipitation is decreased just north of the equator, while the Atlantic between 0 and 20° S is wetter.

The precipitation decrease over the South-American continent is consistent with decreased surface air temperatures (Fig. 2.13a), as a direct consequence of decreased insolation. Table 3.1 shows that SSRD is decreased, as well as STRD because of reduced cloudiness. Decreased temperatures are associated with a pressure increase over most of the continent (Fig. 2.13b). The north-easterly monsoon winds are weaker due to the smaller land-sea pressure contrast (Fig. 2.13c and d). A clockwise pattern is present in the wind difference field around 15° S, 35° W (Fig. 2.13d), where pressure changes are negligible (Fig. 2.13b), further weakening the monsoons winds around 10° S and slightly increasing them at 20° S. The South Atlantic Subtropical High (SASH, centred around 35° S, 5° W) is slightly stronger and located closer to the continent (Fig. 2.13b), intensifying the easterlies at 20° S and the westerlies at 40° S.

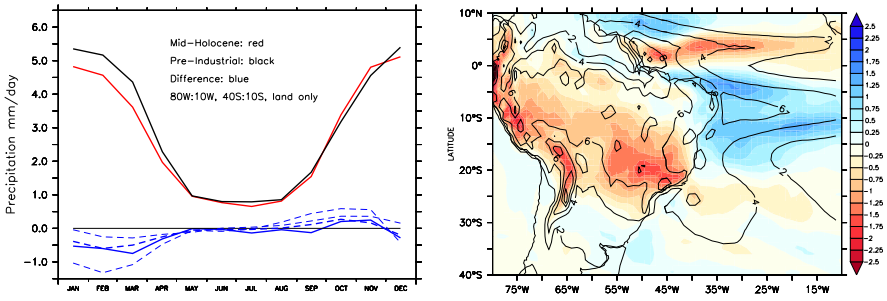

(a) Monthly precipitation over South America, (b) JFM precipitation over South America, mm/day mm/day

Figure 2.12: (a) Precipitation (mm day^{-1}) for PI (black), MH (red) and difference MH-PI (blue) throughout the year. The dashed blue lines are differences in the PMIP2 models: the thick dashed blue line is the average of 12 PMIP2 models (see Fig. 2.15 for references). The thin dashed blue lines are individual PMIP2 model results with the largest and smallest changes for South-America in JFM. **(b)** The spatial pattern of precipitation differences in JFM. Colours indicate MH-PI differences, contours are absolute PI values. Note that the colour scales are different than for the figures in Sects. 2.3.1 and 2.3.2.

The result of reduced landward winds is a lower transport of moisture to the continent. The weaker surface pressure in the MH over most of the continent decreases convection in a northwest-southeast band over South-America (Fig. 2.14a), lowering precipitation amounts. Evaporation over land is reduced in the MH as well (not shown) due to lower surface air temperatures and less precipitation. However, the decreased moisture transport to the continent plays a larger role; $(\Delta P - \Delta E)/\Delta P$ is -70 % over 80° W:40° W, 35° S:5° S.

Over the ocean, the precipitation increase between 0° S and 20° S (Fig. 2.12b) is due to increased upward motion (Fig. 2.14a) as well as the reduced moisture transport to the continent, leaving more moisture to precipitate out over the ocean. Just north of the equator, precipitation is decreased in response to reduced convection near the coast and increased downward motion further away from the coast (Fig. 2.14a).

These changes over the ocean can be related to a change in the ITCZ. Figure 2.14b shows changes in the MH vertical motions with respect to the PI, averaged over 70° W:10° W. The northern part of the convective cell at 5–10° S is intensified in the lower atmosphere while the downward velocities north of that, around 0–5° S, are weaker. The DJF average of vertical motion (not shown) demonstrates a northward shift of the ITCZ in the whole atmospheric column, which indicates that the Mid-Holocene ITCZ was located more equatorward during the SH summer. This is in agreement with the weaker poleward gradient of insolation (Fig. 2.4).

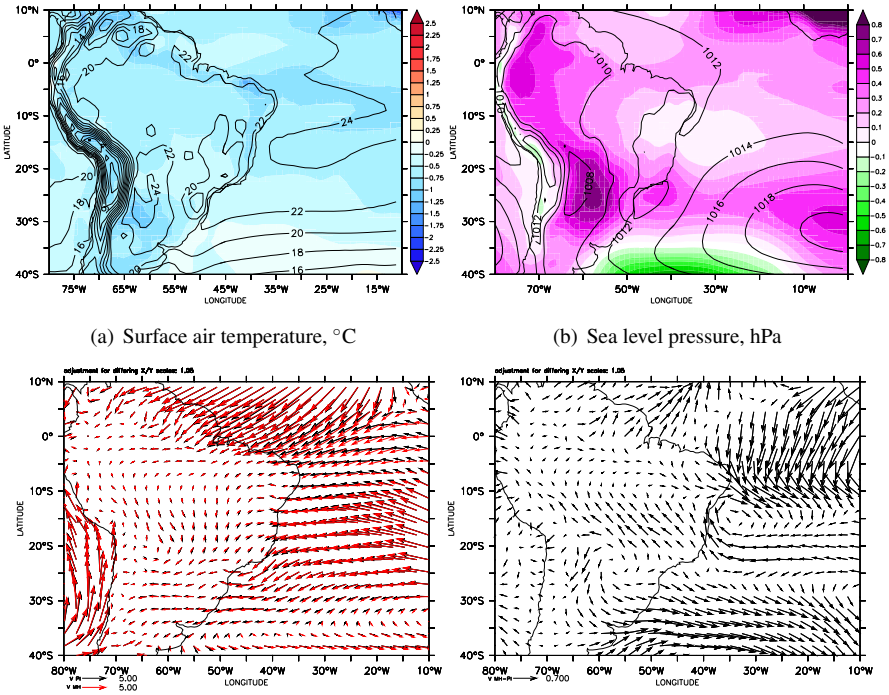

(a) Surface air temperature, °C

(b) Sea level pressure, hPa

(c) Surface wind field, PI, m/s

(d) Surface wind field, MH - PI, m/s

Figure 2.13: MH-PI difference in JFM surface air temperature – **(a)**, °C – and sea-level pressure – **(b)**, hPa; contours are PI values, colours indicate differences between MH and PI. **(c)** Shows the PI surface wind field (black) and the MH surface wind field (red), unit length is 5.0 m s^{-1}, **(d)** gives the difference between the MH and PI wind field, unit length is 0.7 m s^{-1}. These are JFM averages; note that the scales of the colour bars and vectors are not the same as in Figs. 2.7 and 2.9.

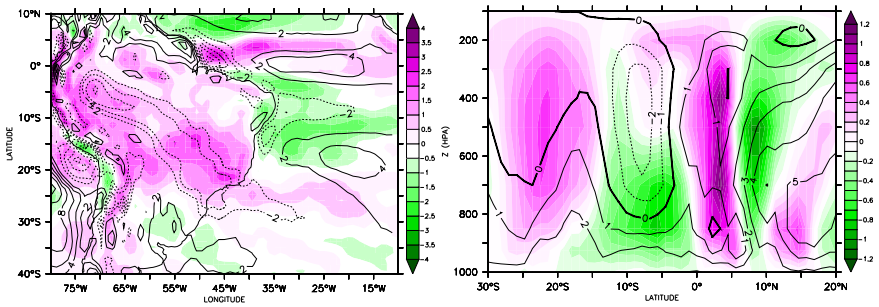

(a) Vertical velocity (omega) at 500hPa, hPa/s (b) Vertical velocity (omega) 70°W:10°W, Pa/s

Figure 2.14: MH-PI JFM difference in **(a)** vertical velocity at 500 hPa in 10^{-2} Pa s^{-1}, and **(b)** vertical velocities averaged over 70° W:10° W. Negative values indicate upward motion. Contours are PI JFM values.

2.4 Discussion

In this study, we investigated the response of monsoons on both hemispheres to changes in the insolation distribution in the Mid-Holocene with respect to pre-industrial climate, using the EC-Earth model, a high resolution model based on a weather forecast model. The North-African and Asian monsoons were stronger during the Mid-Holocene in response to increased summer insolation, while the South-American monsoon was weaker due to decreased summer insolation. These results corroborate the findings of earlier modelling experiments, most of them summarised in Braconnot et al. (2007a); Liu et al. (2004); Tao et al. (2010); Zhao et al. (2005) and Zhao and Harrison (2012).

2.4.1 The North African monsoon

Over North-Africa, we see an intensified meridional temperature and pressure gradient during the Mid-Holocene summer which allows for a stronger moisture advection from the tropical Atlantic to the continent. Moisture advection plays a larger role than local recycling (in agreement with Marzin and Braconnot, 2009a; Zhao et al., 2005). The pressure gradient is reinforced by internal feedbacks over tropical Africa which decrease surface air temperatures and dampen the pressure response. The lower temperatures over tropical North Africa are also present in PMIP2 results (Braconnot et al., 2007a). Over the Atlantic, a dipole pattern in SSTs exists, with lower SSTs south of 15° N due to stronger winds and increased evaporation and higher SSTs north of 15° N due to weaker winds and decreased evaporation. This dipole pattern further enhances the meridional temperature and pressure gradients, shifting the ITCZ northward, as has also been reported by Zhao et al. (2005) and Zhao and Harrison (2012), who state the dipole is further south, around 5–10° N.

The northward shift of the ITCZ, which can be inferred from changes in precipitation and vertical velocity, is supported by Braconnot et al. (2007a,b); Liu et al. (2004); Zhao et al. (2005) and Marzin and Braconnot (2009a). The precipitation increase over the continent is also related to a weakening of the African Easterly Jet (AEJ). Texier et al. (2000) and Patricola and Cook (2007) also find a decrease in or disappearance of the AEJ, but only when vegetation feedbacks are included. An atmosphere-ocean experiment without dynamic vegetation in Texier et al. (2000) results in an increased AEJ located further north, as opposed to the the EC-Earth experiments in which the AEJ weakens and remains at the same location.

A notable difference with previous studies is the precipitation increase over north-westernmost Africa. Only two PMIP2 ocean-atmosphere models show a precipitation increase in this region as well (GISS, Schmidt et al., 2006 and UBRIS-HadCM3, Gordon et al., 2000). EC-Earth, GISS and UBRIS all show an increase in southerly winds into north-westernmost North Africa, which in EC-Earth is related to a pressure reduction at 25° N, 10° W. Southerly moisture advection $\vec{Q}$ into this area is increased, while north-westerly moisture advection from the Atlantic is decreased. This suggests that the precipitation increase over north-westernmost Africa is monsoonal and is not related to the subtropical Atlantic. However, we cannot exclude that short-lived depressions from the Atlantic had an influence on precipitation over this part of Africa, because these disappear in the averages. Further investigation into the influence of these depressions is beyond the scope of this study. The high resolution and, consequently, the accurate representation of topography could play a role in the precipitation increase over north-westernmost Africa as well: in mid- and eastern North Africa the MH precipitation does not extend north of the Tibesti and Ahaggar mountains.

The increase and northward shift in precipitation over North Africa in EC-Earth is larger than in most PMIP2 ocean-atmosphere models, as shown in Figs. 2.6a and 2.15. Figure 2.6a shows that the summer precipitation increase over monsoonal North Africa is larger than in any PMIP2 model. The northward shift towards the Sahara is also relatively large compared to PMIP2 models (Fig. 2.15). This could indicate that a higher resolution and sophisticated parameterizations play a role in reproducing the precipitation pattern for the Mid-Holocene. However, to determine the exact roles of resolution and parameterization, further sensitivity experiments are needed. For EC-Earth this is currently not possible, as no other resolutions or versions similar to the one used here are currently available.

Despite the relatively large northward shift in precipitation in EC-Earth, this shift is not large enough to sustain the plant types that are known to have occurred during the Mid-Holocene (Braconnot et al., 2007a; Joussaume et al., 1999). This could be related to the lack of vegetation feedbacks in this study, as both the vegetation cover and albedo is kept at pre-industrial values in both simulations. Vegetation is thought to have a positive feedback on the orbitally induced monsoonal precipitation increase over North Africa through the warming effect of a lowered albedo (Bonfils et al., 2001), an increased sensible heat flux due to increased roughness length and an increased latent heat flux due to increased evapotranspiration (Levis

et al., 2004; Texier et al., 2000). The surface warming and increased moisture recycling increase convection and the landward moisture flux. However, there are also studies indicating a negative feedback of vegetation on (annual) precipitation during the Mid-Holocene, when bare soil evaporation was more important and albedo feedbacks played a smaller role due to wetter conditions (Notaro et al., 2008; Wang et al., 2008). Another mechanism that could play a role is the ventilation mechanism (inflow of low moist static energy air, Hales et al., 2006; Su and Neelin, 2005). Further research with dynamic vegetation models and/or sensitivity experiments is necessary to investigate the role of vegetation feedbacks, soil changes, albedo changes and the ventilation effect, as well as the interaction between these effects. Given that the resolution and parameterizations in EC-Earth are good enough to resolve the orography over North-Africa (including the Atlas, Tibesti, Ahaggar and East African mountains) and to capture the present-day precipitation patterns well (Fig. 2.1), we think that the lack of precipitation over the Sahara in the Mid-Holocene in EC-Earth is not so much related to insufficient resolution or the accuracy of parameterizations, but to the lack of interactive vegetation.

2.4.2 The Asian monsoons

Over Asia, monsoonal precipitation is enhanced as well in response to increased summer insolation. Figure 2.9a shows that the the amount of precipitation increase in summer over continental Asia is very similar to the increases in PMIP2 models, especially in August and September. In EC-Earth, the largest precipitation increases are along the southern rim of the Himalayas, northern India and southern China. There is little change over northern China and the South-East Asian peninsula. These precipitation changes are broadly in agreement with PMIP2 studies (Braconnot et al., 2007a; Zhao and Harrison, 2012) but patterns vary amongst models (Braconnot et al., 2007a; Liu et al., 2004; Marzin and Braconnot, 2009a; Tao et al., 2010; Zhao et al., 2005). A notable difference between EC-Earth and most PMIP2 models is that the largest precipitation changes are located exactly on the southern rim of the Himalayas, which are represented well at the T159L62 resolution. Models at lower resolutions also represent the Himalayas well, but the precipitation pattern in EC-Earth is more detailed than in previous studies. Dallmeyer et al. (2010) also show a precipitation increase on the southern rim of the Himalayas.

In EC-Earth, precipitation increase over continental Asia is mostly related to a redistribution of precipitation between ocean and land, as well as the increased moisture transport from the southern equatorial Indian Ocean (corroborated by Clemens et al., 1991; Hastenrath, 1991; Marzin and Braconnot, 2009a). Local recycling over land does not play a role, which is opposite to the findings of Marzin and Braconnot (2009a) and Dallmeyer et al. (2010). Evaporation over the ocean is lower during the MH due to increased upwelling over the Arabian Sea and increased runoff in the Bay of Bengal (also described in Marzin and Braconnot, 2009a), as well as reduced wind speeds between the equator and 10–15° N. These reduced winds are related to increased surface pressure at 10–20° N, linked to an intensified north-

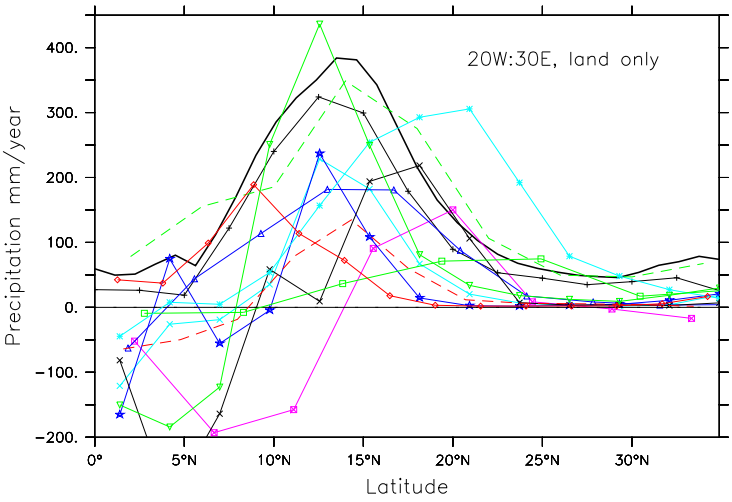

Figure 2.15: Annual mean precipitation difference MH-PI over North Africa (20° W:30° E, land only). The thick black line is for EC-Earth, coloured lines are for PMIP2 ocean-atmosphere models. The colours and symbols are the same as in Braconnot et al. (2007a), Fig. 10. See their Table 2 for model characteristics and references. Two additional models that are included here are: GISS modelE (green dashes, Schmidt et al., 2006) and CSIRO (red dashes, Gordon et al., 2000).

western Pacific subtropical High (Zhao et al., 2005). Stronger winds occur close to the continent over the Arabian Sea, Bay of Bengal, South China Sea and the southern tropical Indian Ocean. This pattern of MH winds is generally agreed upon amongst models, but the exact pattern and magnitude of winds varies (Dallmeyer et al., 2010; Liu et al., 2004; Marzin and Braconnot, 2009a,b; Tao et al., 2010; Texier et al., 2000; Zhao et al., 2005). The weakened southerly winds in the western Indian Ocean and the associated increased moisture convergence over this area is consistent with previous PMIP results (Braconnot et al., 2007a; Zhao and Harrison, 2012). The only ocean area providing more evaporation is the southern tropical Indian Ocean, where wind speeds are increased. Liu et al. (2004) suggest another ocean feedback that reduces the precipitation increase over Asia: increased MH SSTs over the western tropical North Pacific lead to increased convergence and precipitation, competing with convergence and precipitation increases over the Asian continent. This feedback does not occur in the EC-Earth experiments.

2.4.3 The South American monsoon

Over South America, surface air temperatures are lower and surface pressure is higher during the Mid-Holocene as a direct response to the reduced summer insolation. Summer monsoonal precipitation is decreased and the magnitude of this decrease is very similar to that in previous PMIP2 models (Fig. 2.12a). The precipitation decrease occurs over most of the continent, with the exception of the north-eastern tip of the continent, as a result of weakened monsoon winds and reduced convection. This is consistent with previous model studies (Dias De Melo and Marengo, 2008; Kitoh and Murakami, 2002; Liu et al., 2004; Valdes, 2000). The precipitation increase over the north-eastern coast could be a sign of monsoon retreat, as well as a shift in the ITCZ, because upward motion between the equator and 10° S over the Atlantic is stronger as the ITCZ shifts northward in response to a weakened poleward insolation gradient. The South Atlantic Subtropical High is located slightly closer to the continent, which is in agreement with Dias De Melo and Marengo (2008) in their DJF average. Although previous model studies agree on the general pattern of the MH monsoon over South America, more research is required because only two of the studies mentioned here are coupled ocean-atmosphere models (Kitoh and Murakami, 2002; Liu et al., 2004), both using a relatively low resolution.

2.4.4 EC-Earth vs. paleodata

Our results are not only in general agreement with other modelling studies, but also with paleodata. The exception is the lack of precipitation increase over the Sahara, but this is a shortcoming of all ocean-atmosphere models (Braconnot et al., 2007a). Reconstructions of vegetation patterns (e.g. Bartlein et al., 2011; Jolly et al., 1998; Wu et al., 2007) and lake levels (e.g. Kohfeld and Harrison, 2000; Yu and Harrison, 1996) show that North Africa, northern India and South-East Asia were wetter dur-

ing the Mid-Holocene. An overview of these reconstructions is given in Liu et al. (2004). Reconstructions of precipitation in southern India and South-East Asia are sparse. For China, more reconstructions of temperature and precipitation are available, a summary can be found in Tao et al. (2010), along with the average results of PMIP2 over China. There is some spread amongst models (Braconnot et al., 2007a; Hsu et al., 2010; Marzin and Braconnot, 2009a; Tao et al., 2010; Zhao et al., 2005), but EC-Earth generally agrees with PMIP2 models as well as with paleodata. Temperature is higher, especially towards northern China, and precipitation is increased, especially in south-west China near the Himalayas. One discrepancy is that EC-Earth fails to reproduce the precipitation increase over north-western China.

In South America, lake levels were lower during the Mid-Holocene (Baker et al., 2001; Sifeddine et al., 2001; Turcq et al., 2002) and studies of pollen and ocean cores show a general drying and imply a more northerly location of the ITCZ (Behling, 2002; Haug et al., 2001; Mayle et al., 2000). These paleodata studies do not clearly indicate wetter conditions in north-east Brazil, which does occur in the EC-Earth Mid-Holocene experiment as well as in other models (Dias De Melo and Marengo, 2008; Kitoh and Murakami, 2002; Liu et al., 2004; Valdes, 2000).

Note that these comparisons are based on changes in the model's summer precipitation, whereas most paleodata reconstructions indicate changes in annual precipitation. However, in the monsoon areas discussed here, precipitation barely changes in winter (see Figs. 2.6a, 2.9a, 2.12a) so the summer precipitation changes are a good indication of changes in the annual precipitation.

2.5 Conclusions

Further research is necessary to close the gap between paleodata and climate modelling. The roles of vegetation, soil moisture, albedo, evapotranspiration, the ventilation effect and their combined effect need to be investigated further (Bonfils et al., 2001; Braconnot et al., 2007a; Dallmeyer et al., 2010; Kutzbach et al., 1996; Levis et al., 2004; Patricola and Cook, 2007; Su and Neelin, 2005; Vamborg et al., 2011), especially for North-Africa where models fail to reproduce the northward extend of the monsoon. A higher resolution and sophisticated model parameterization can also help to close the gap between paleodata and models, as indicated by the relatively large northward extend of the North African monsoon in EC-Earth. With this model we have not only contributed to PMIP and confirmed its previous conclusions, we have also obtained an unprecedentedly detailed picture of Mid-Holocene monsoon dynamics and precipitation.

3

Response of the North-African summer monsoon to precession and obliquity forcing

Abstract

In this paper, we use a high-resolution coupled climate model, EC-Earth, to investigate the response of the North-African monsoon to separate precession and obliquity forcing. Precession has the largest effect on the monsoon, as strongly increased summer insolation results in more intense and more northward heat lows over North-Africa, drawing in stronger south-westerly winds. A stronger South Atlantic high pressure area further enhances the meridional pressure gradient. The strengthened south-westerly monsoon winds carry more moisture landwards from both the northern and southern tropical Atlantic, mostly due to reduced precipitation over the ocean. Upper level circulation patterns are shifted northwards. Obliquity-induced summer insolation changes over the tropics are nearly zero, but they nonetheless result in notable changes in precipitation and monsoonal circulation over North-Africa. The obliquity-induced precipitation changes originate mostly from the tropical Atlantic. Our results provide an explanation for the precession and obliquity signals preserved in the sedimentary record of North-Africa, but the mechanisms are different than previously suggested by Tuenter et al. (2003). Using a quasi-geostrophic model of intermediate complexity they show a smaller response to the precession and obliquity forcing, suggesting that northerly moisture transport from higher latitudes plays an important role. In contrast, we argue that moisture transport from both the northern and southern tropical Atlantic, resulting from increased insolation and an increased tropical insolation gradient, is responsible for the precession and obliquity signals in the North-African monsoon.

This chapter is under review for publication in Climate Dynamics as: Bosmans, J.H.C., S.S. Drijfhout, E. Tuenter, F.J. Hilgen and L.J. Lourens (2014). Response of the North-African summer monsoon to precession and obliquity forcing

3.1 Introduction

Sedimentary records from North-Africa and its surroundings suggest that the North-African summer monsoon responds strongly to astronomical forcing (e.g. Larrasoaña et al., 2003; Pokras and Mix, 1987; Rossignol-Strick, 1985). Changes in monsoon intensity are mainly driven by the precession cycle, which dominates the incoming solar radiation (insolation) changes over the tropics. Precession governs the seasonality of insolation and is modulated by the eccentricity of the Earths orbit. Evidence for an obliquity (axial tilt) component has been found as well (Lourens et al., 1996, 2001), despite the near absence of obliquity-induced summer insolation changes over the tropics.

Numerous climate modelling studies have confirmed the presence of astronomical cycles in the monsoon systems. Most of these modelling studies use time slices of the last glacials and interglacials, such as the Eemian ($\sim$ 126 ka, kyr before present) and glacial inception at 115 ka (e.g. Braconnot et al., 2008; de Noblet et al., 1996; Montoya et al., 2000; Prell and Kutzbach, 1987), as well as the last glacial maximum and the Holocene, including some of the earliest modelling studies (e.g. Kutzbach, 1981) and many PMIP-simulations (e.g. Braconnot et al., 2007a). In these modelling studies, the combined effect of all orbital parameters (eccentricity, precession and obliquity) on monsoon intensity are investigated.

At present, there are not many studies that examine the precession and obliquity signals separately. The few that do focus mainly on precession. Short and Mengel (1986) used an energy balance model (EBM) to investigate the response of the tropics to precession. Prell and Kutzbach (1987) performed idealised precession and obliquity experiments with an atmospheric general circulation model (AGCM) in permanent July mode. Braconnot and Marti (2003) studied the effect of precession on the Indian monsoon and the Indian Ocean using a GCM. Clement et al. (2004) compare the importance of precession to glacial boundary conditions in the tropics. The precession effect on subtropical highs is investigated by Mantsis et al. (2013). Merlis et al. (2013a,b) study tropical circulation and precipitation in response to precession changes. Their idealised GCM shows a stronger monsoonal Hadley circulation and increased precipitation on the northern hemisphere when summer insolation on this hemisphere is increased during a precession minimum. The study of Erb et al. (2013) also finds stronger monsoons during a precession minimum, as well as during high obliquity, but the monsoons are not the main focus of their study. Wyrwoll et al. (2007) also performed both precession and obliquity experiments, but focussed only on the Australian monsoon. The response of the Asian monsoons to obliquity is tested by Chen et al. (2011), also using a GCM. However, in their obliquity experiments neither Prell and Kutzbach (1987) nor Chen et al. (2011) nor Erb et al. (2013) fully remove the precession signal, which affects the amplitude of the obliquity signal (Tuenter et al., 2003).

The only study, to our knowledge, that has examined the separate precession and obliquity effects on the North-African monsoon is that of Tuenter et al. (2003). Us-

ing an intermediate complexity quasi-geostrophic model, EC-Bilt, they investigated the climate response to the separate astronomical forcings. They found a stronger and more northward monsoon over North-Africa at times of minimum precession or maximum obliquity, when summer insolation is increased. In addition they showed that remote forcings, i.e. insolation changes at high latitudes, play an important role in both the precession and obliquity experiments. The monsoonal south-westerlies are intensified, forced by a deepening of convergence over Asia, and there is increased moisture transport from the north into the monsoon region. Such mechanisms can explain why obliquity affects the North-African monsoon despite the near lack of summer insolation change over the tropics. Precession-induced insolation changes over the tropics also induces a stronger land-sea contrast, which dominates the remote effects.

A weakness of the quasi-geostrophic model EC-Bilt is that it cannot capture tropical circulation patterns or cross-equatorial moisture and energy transport well. Therefore we revisit the response of the North-African monsoon to separate precession and obliquity forcing using the fully coupled state-of-the-art general circulation model (GCM) EC-Earth. Our aim is to investigate whether the main conclusions of Tuenter et al. (2003) still hold, by examining which physical mechanisms and feedbacks operate for both orbital parameters, including surface as well as upper level circulation features. EC-Earth is built upon a weather forecast model and runs at a resolution of $\sim$1.125° (Hazeleger et al., 2010, 2011). The higher resolution and more sophisticated parametrizations of EC-Earth compared to EC-Bilt result in a much more reliable representation of the monsoonal precipitation and related circulation patterns. Moreover, EC-Earth has been shown to respond well to Mid-Holocene orbital forcing in Chapter 2 (Bosmans et al., 2012).

This paper is set up as follows: in Section 3.2 the EC-Earth model and the experiments are described. Section 3.3.1 describes the orbitally forced changes over the tropics. The North-African monsoon is discussed in Section 3.3.2 for precession and in Section 3.3.3 for obliquity. A discussion and conclusion is given in Section 6.4.

3.2 Model and Experiment set-up

3.2.1 The model: EC-Earth

EC-Earth is a fully coupled ocean-atmosphere GCM (general circulation model, Hazeleger et al. 2010, 2011). The atmospheric part of EC-Earth 2.2 is based on the Integrated Forecasting System (IFS), cycle 31R1, of the European Centre for Medium-range Weather Forecast (ECMWF). Its spectral horizontal resolution is T159 (roughly 1.125°x1.125°) with 62 vertical levels. IFS cycle 31R1 has the Bechtold et al. (2008) convection scheme and the Balsamo et al. (2009) land surface scheme H-TESSEL, which includes surface runoff. The ocean component consists of NEMO (Nucleus for European Modelling of the Ocean), version 2, running at

a horizontal resolution of nominally 1° with 42 vertical levels (Madec 2008; Sterl et al. 2011). NEMO incorporates the sea-ice model LIM2. The ocean, sea-ice, land and atmosphere are coupled through the OASIS3 coupler (Valcke and Morel, 2006).

EC-Earth performs well for the present-day compared to CMIP3 models and data in terms of climatology as well as interannual, spatial and temporal variability (Hazeleger et al., 2010, 2011). More importantly, we have previously shown that monsoons are represented well in both a pre-industrial and a Mid-Holocene paleo-experiment (Chapter 2, Bosmans et al. 2012).

3.2.2 Experimental set-up: insolation forcing and boundary conditions

In order to examine the separate precession and obliquity (tilt) signals we have performed four time-slice experiments with different orbital parameters:

Pmin: Minimum precession, minimum obliquity

Pmax: Maximum precession, minimum obliquity

Tmax: Maximum obliquity with a circular orbit

Tmin: Minimum obliquity with a circular orbit

The values of the orbital parameters are given in Table 1.1. These are the same as the P-T-, P+T-, P0T+, P0T- experiments in Tuenter et al. (2003), and are based on the extreme values of the orbital parameters occuring in the last 1 Ma (Berger, 1978). For precession, extremes of the precession parameter $e \sin(\pi+\tilde{\omega})$ are chosen rather than extremes of $\sin(\pi+\tilde{\omega})$, as eccentricity e modulates precession. We did not perform the precession experiments with maximum obliquity (P-T+ and P+T+ in Tuenter et al. 2003) due to lack of computing time. Furthermore, Tuenter et al. (2003) have shown that the precession signal (in the African monsoon) is not dependent on obliquity. The obliquity signal does depend on the prevailing precession (Tuenter et al., 2003), but in this study we fully exclude precession in the obliquity experiments by setting eccentricity to zero (i.e. prescribing a circular orbit).

During a precession minimum (Pmin) the summer solstice occurs in perihelion, so seasonality is enhanced in the Northern Hemisphere (NH) and reduced in the Southern Hemisphere (SH). The opposite occurs during a precession maximum (Pmax), when the summer solstice occurs in aphelion. Figure 3.1(a) shows the insolation differences between Pmin and Pmax, calculated using the equations of Berger (1978). During an obliquity maximum (Tmax, maximum tilt), both NH and SH summers receive more insolation, especially at the poles, while during an obliquity minimum (Tmin) summer insolation is reduced. The obliquity-induced insolation changes are shown in Figure 3.1(b). The orbital parameters, shown in Table 1.1, are kept fixed during each experiment. All other boundary conditions (e.g. the solar constant, greenhouse gas concentrations, orography, ice sheets, vegetation) were kept constant at pre-industrial levels. We keep vernal equinox fixed

at the 21^{st} of March and use the present-day calendar. This introduces some errors in the precession experiments, because the lengths of the seasons and the dates of the equinoxes and solstices change along the precession cycle (Joussaume and Braconnot, 1997). A celestial calendar, using angular months based on astronomical positions, would be more appropriate. However, because Tuenter et al. (2003), and others (e.g. Braconnot et al., 2008; Chen et al., 2011), also use the present-day calendar, we maintain this calendar to facilitate comparison.

EC-Earth is computationally expensive. Each experiment was run for 100 years, initiated from a pre-industrial experiment (Hazeleger et al., 2011). The first 50 years are considered spin-up. The experiments are long enough for atmospheric and surface variables that are of interest to monsoon dynamics to equilibrate to the forcing (see Figure 3.2). Annual mean temperatures drop in the first $\sim$10 years, then level off. Temperatures during Tmax show a relatively strong cooling trend (Figures 3.2(a), 3.2(b)), but these trends to not cause a trend in the tropical monsoonal precipitation (Figure 3.2(d)). The globally averaged tendency term of surface air temperature, dT/dt, is near-zero and shows no trend in all experiments (not shown). Precipitation over the tropical land areas, an indication of monsoon precipitation, show virtually no trend (Figure 3.2(d)).

3.3 Results

In this section we will first describe the precession- and obliquity-induced changes over the (sub-) tropics (Section 3.3.1). Then we focus on the North-African summer monsoon, investigating in more detail the precession- and obliquity-induced changes in the monsoon circulation (Section 3.3.2 and 3.3.3). In our text and main figures we compare Pmin to Pmax and Tmax to Tmin, i.e. comparing maximum to minimum boreal summer insolation. The figures in the Appendix give results for each experiment separately. We use June-July-August averages for boreal summer and December-January-February for austral summer.

3.3.1 The tropics and sub-tropics

During boreal summer, insolation is higher in both hemispheres during Pmin than during Pmax, while lower insolation prevails during austral summer. Insolation differences reach over 100 Wm^{-2}, see Figure 3.1(a). These precession-induced insolation changes result in intensified boreal summer monsoons and weakened austral summer monsoons (Ruddiman, 2007). EC-Earth shows enhanced precipitation during JJA over the monsoon regions of North-Africa, Asia and North-America, as well as increased landward monsoon winds and decreased precipitation over most of the surrounding oceans (Figure 3.3(a)). However, the monsoon south-westerlies over the western Indian Ocean are weaker and more north-westward, and precipitation over the western Indian Ocean is increased. Over the North-Atlantic, the anticyclonic winds are stronger, related to a strengthening and slight northwestward shift

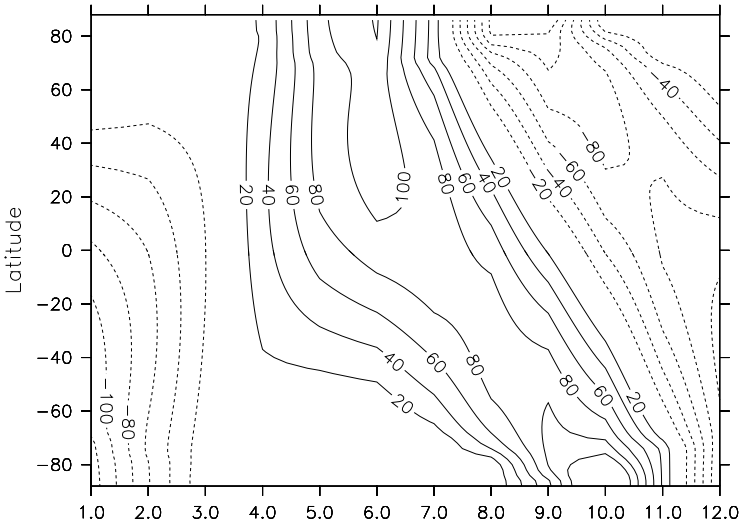

(a) Insolation Pmin-Pmax, Wm^{-2}

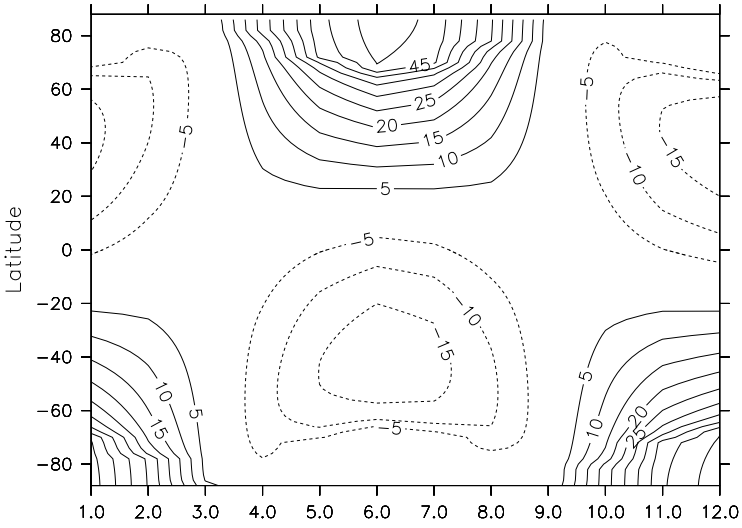

(b) Insolation Tmax-Tmin, Wm^{-2}

Figure 3.1: Insolation differences at the top of the atmosphere (TOA): precession minimum minus maximum (a, contour interval 20 Wm^{-2}) and obliquity (tilt) maximum minus minimum (b, contour interval 5 Wm^{-2}). See Table 1.1 for the values of the orbital parameters. Insolation is calculated for every second latitude and every month (mid-month)

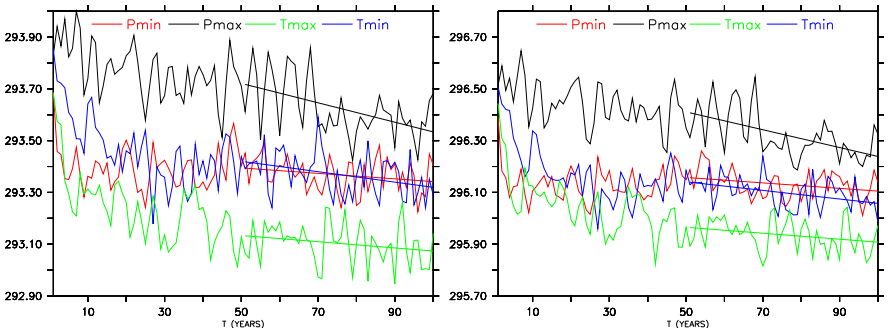

(a) Surface air temperature, K

(b) Sea surface temperature, K

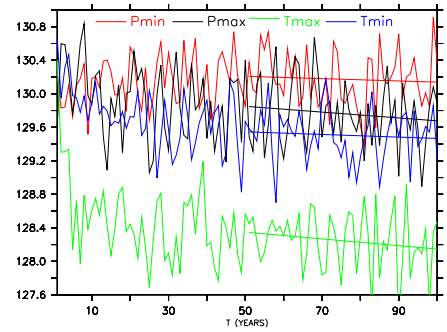

(c) Surface heat flux, Wm^{-2}

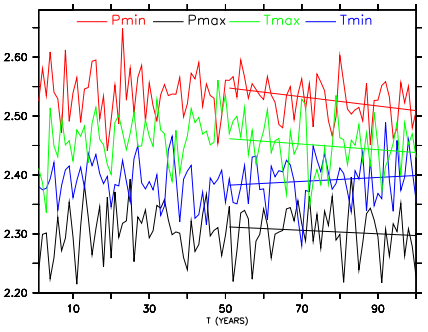

(d) Precipitation, land only, mm/day

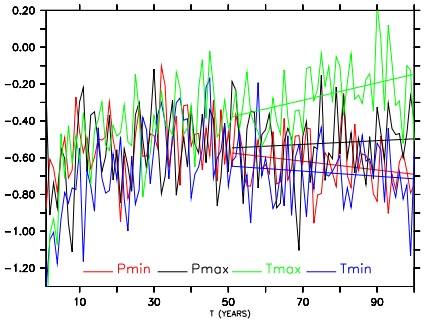

(e) TOA net radiative flux, Wm^{-2}

Figure 3.2: Annual mean zonally averaged 40°S:40°N surface air temperature (a), sea surface temperature (b), sum of surface sensible and latent heat fluxes (c) and total (convective + large scale) precipitation (d) in all four experiments. Top-of-atmosphere annual global mean net radiative flux (net shortwave plus net longwave radiation) is given in (e). Trend lines over the last 50 years are added in each figure (calculated using linear regression)

of the Azores High. A stronger South-Atlantic subtropical high results in stronger southerly cross-equatorial winds from the south-eastern Atlantic into the North-African monsoon region. High-pressure areas over the North- and South-Pacific are also intensified, with stronger anticyclonic winds over the North-Pacific and stronger south-easterlies over the tropical South-Pacific. There is more precipitation over the eastern tropical Pacific and less in the west during Pmin. These changes are similar in magnitude to those over the monsoonal regions, but the largest changes occur over North-Africa and Asia, where the JJA-averaged precipitation and wind speed differences reach over 12 mm/day and 4 m/s respectively. For North-Africa, the maximum increase in precipitation and the monsoonal south-westerlies in EC-Earth is approximately twice as large as in EC-Bilt (Tuenter et al., 2003).

During DJF, the largest changes occur over the tropical oceans and the (southern) continental monsoon regions. The austral summer monsoons are weaker in response to lowered insolation (Figure 3.3(b)). During Pmin, it is drier over South-America, South-Africa, Indonesia and Australia, with weaker landward monsoon winds and more precipitation over the surrounding oceans. Over the Pacific, surface pressures are reduced and winds over the tropics are weakened. There is more precipitation over the western tropical Pacific, and less over the north. Over the North-Atlantic, the north-easterly trade winds are weaker in response to lower pressure over the Azores.

Obliquity-induced insolation changes over the tropics are very small ($< 5\ \mathrm{Wm}^{-2}$) compared to the precession-induced changes (compare Figures 3.1(a) and 3.1(b)). The monsoonal response to obliquity changes is therefore smaller than the response to precession changes, but a clear signal in monsoonal winds and precipitation can still be seen, see Figures 3.3(c) and 3.3(d). The obliquity signal could be a response to an increased cross-equatorial insolation gradient (see Chapter 5). Both the boreal and austral summer monsoons are stronger during Tmax, because obliquity increases summer insolation as well as the cross-equatorial insolation gradient. During boreal summer, the largest precipitation increase is over North-Africa, while the Asian and North-American monsoons are stronger as well. Again, the response over North-Africa is stronger in EC-Earth as in EC-Bilt (Tuenter et al., 2003). Changes over the Pacific are smaller than over the monsoonal areas, with a drying of the northern tropical Pacific. The southern tropical Atlantic and the south-eastern and northern Indian Ocean are dryer as well, while the northern tropical Atlantic and western tropical Indian Ocean are wetter. In austral summer, insolation is increased over the SH and the largest precipitation increase occurs over monsoonal South-Africa and Australia (Figure 3.3(d)). Over the tropical Atlantic, precipitation changes are opposite to those of boreal summer (3.3(c)), with drying just north and wetter conditions just south of the equator. The western Indian Ocean gets wetter, while the western Pacific gets drier.

Overall, we find that in EC-Earth the summer monsoons respond to both the precession- and obliquity-induced insolation changes, with stronger (weaker) monsoons when summer insolation is increased (decreased), i.e. an opposite effect on both hemispheres for precession while obliquity has the same effect. Also, the re-

sponse to precession changes is stronger, as is the forcing, but an obliquity signal is present despite the small obliquity-induced insolation changes over the tropics.

In the next sections we will focus on the North-African monsoon, which responds strongly to both precession and obliquity changes. Orbitally induced changes of the Asian monsoons will be presented in a separate publication.

3.3.2 The North-African Monsoon: Precession

There are large differences in precipitation over North-Africa during the summer monsoon between Pmin and Pmax, see Figure 3.3(a). During Pmin, summer precipitation maxima occur over the continent at 5-15°N, with rates of 10 mm/day and higher. Precipitation extends far north into the Sahara; the 1 mm/day contour extends up to 20-25°N in the north-eastern Sahara and up to the Atlas mountains in the west (see Appendix, Figure 3.8). During Pmax, summer precipitation occurs mostly over the Atlantic, while over land the precipitation rate is only 2-6 mm/day over the south-western coast. Precipitation does not reach further north than 15°N (see Figure 3.8). The difference in terms of percentage is as large as 471% (averaged over 0°N:30°N, 20°W:50°E, land only, JJA), while the precession-induced insolation increase is 21% over this area.

The difference between Pmin and Pmax is also evident from the yearly cycle of precipitation over tropical North-Africa, shown in Figure 3.4(a). Summer monsoonal precipitation is much larger during Pmin, reaching over 8 mm/day (averaged over 10°W:40°E, 5°N:20°N). During Pmax, the summer precipitation over the continent is small, and in contrast to Pmin, precipitation maxima occur in spring and autumn, not summer (Figure 3.4(a)). This suggests that precipitation responds strongly to the local insolation forcing over the tropics, which has a single strong peak in summer during Pmin and two peaks in spring and autumn during Pmax (Figure 3.4(c)). North of the Tropic of Cancer both Pmin and Pmax show a single summer insolation peak.

To further investigate the differences between Pmin and Pmax, we look into changes in temperature, the surface energy balance, pressure, and winds at the surface. Figures 3.5(a) and 3.9 show that JJA surface air temperatures are higher during Pmin, especially over land, with the exception of the continental monsoon region. There, temperatures are up to 5° lower, which can be explained by feedbacks from monsoon intensification. Increased cloud cover reduces the surface downward shortwave radiation by 59.3 Wm^{-2} (averaged over 10°W:40°E, 5°N:20°N, JJA, land only), despite the 90 Wm^{-2} increase in downward shortwave radiation at the top of the atmosphere. Also, increased evaporation leads to an increased surface latent heat flux of 52.9 Wm^{-2} (a difference of more than 150%). These changes are only partly compensated by increased surface downward thermal radiation due to increased cloud cover (49.8 Wm^{-2}) and decreased surface upward shortwave radiation (14.0 Wm^{-2}). Due to the cooler surface, there is a smaller surface sensible heat flux (37.9 Wm^{-2}) and less surface upward thermal radiation (11.6 Wm^{-2}). See Table 3.1 for a summary. These changes in the surface energy balance completely

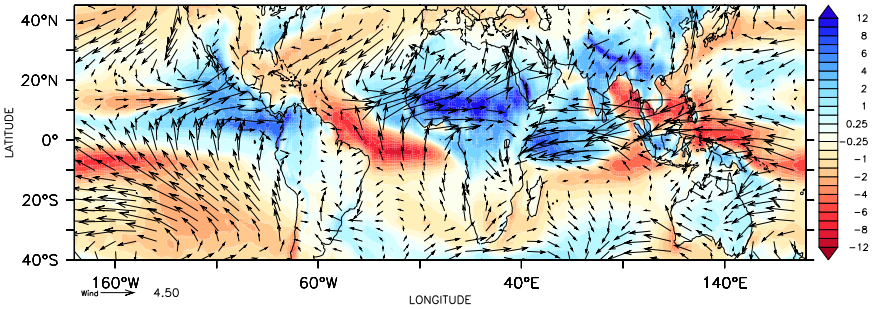

(a) Pmin-Pmax JJA precipitation (mm/day), wind (m/s)

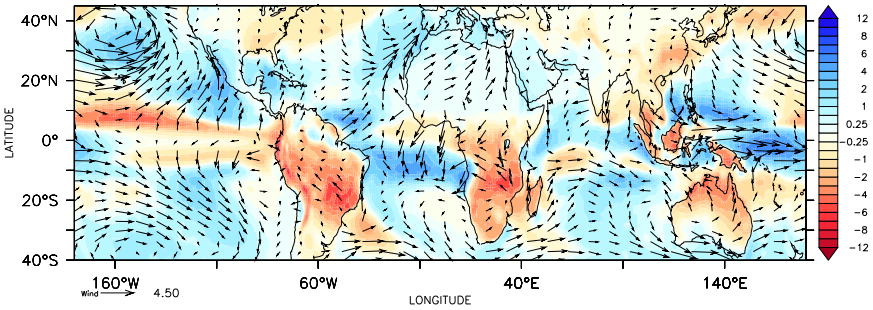

(b) Pmin-Pmax DJF precipitation (mm/day), wind (m/s)

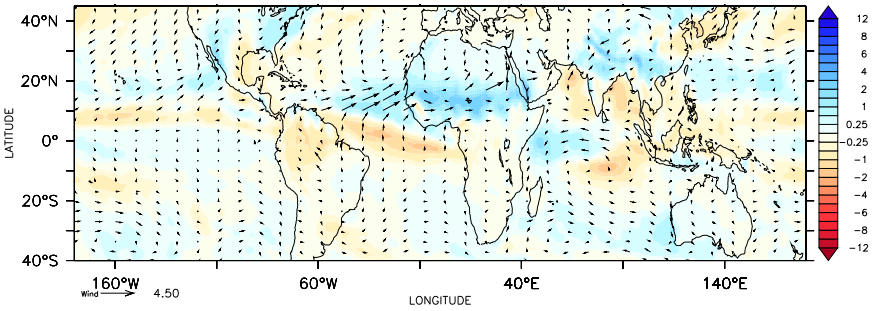

(c) Tmax-Tmin JJA precipitation (mm/day), wind (m/s)

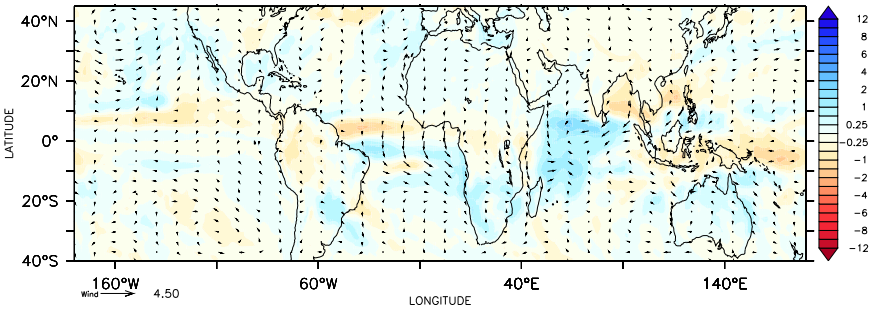

(d) Tmax-Tmin DJF precipitation (mm/day), wind (m/s)

Figure 3.3: (Caption on the following page)

Table 3.1: Overview of surface energy balance terms per experiment and differences, averaged over 10°W:40°E, 5°N:20°N, JJA, land only, in Wm^{-2}. SSRD is surface shortwave radiation downward, STRD is surface thermal (longwave) radiation downward, SLHF is surface latent heat flux, SSHF is surface sensible heat flux, SSRU is surface shortwave radiation upward, STRU is surface thermal (longwave) radiation upward. Positive values of the energy budget terms indicate a flux from the atmosphere towards the surface

	Pmin	Pmax	Pmin-Pmax	Tmax	Tmin	Tmax-Tmin
SSRD	205.6	264.9	-59.3	226.6	247.3	-20.7
STRD	398.7	348.9	49.8	378.9	376.8	2.1
SLHF	-82.9	-30.1	-52.9	-71.9	-66.3	-5.5
SSHF	-26.4	-64.3	37.9	-36.7	-46.2	9.5
SSRU	-50.3	-64.3	14.0	-55.8	-60.8	5.0
STRU	-443.4	-455.0	11.6	-440.6	-449.9	9.3

counteract the direct warming effect of increased insolation.

During Pmin, sea surface temperatures are generally higher in summer due to increased insolation (not shown), but the changes are smaller than over land due to the ocean's larger heat capacity. Near the south-west coast of North-Africa SSTs are lower during Pmin. Increased winds over this region (see Figure 3.3(a)) create stronger upwelling, cooling the surface.

The increased monsoonal winds into North-Africa are a response to changes in surface pressure. Figure 3.5(c) illustrates that surface pressure in JJA is reduced by up to 8 hPa over the north-eastern Sahara, associated with intensified heat lows, and up to 7 hPa over the north-western coast, where the Azores High is shifted northwestward. The pressure response over tropical North-Africa is small due to the temperature decrease over the monsoon area (Figure 3.5(a)). The pressure response to the insolation changes is therefore not a simple intensification of the land-sea pressure gradient. During Pmin, the low pressure areas are stronger and located further north than during Pmax, drawing in stronger monsoon winds and allowing them to penetrate further north (Figure 3.10). Also, a stronger South-Atlantic subtropical high further increases the pressure gradient between the (southern) Atlantic and the northern Sahara, causing more southerly winds to cross the equator into the monsoon area. The increased pressure over tropical eastern North-Africa (Figure 3.5(c)) is related to the northward shift of the Saharan lows. Near the west coast, the trade winds at 10-20°N are turned more landward during Pmin (Figures 3.3(a), 3.10).

Figure 3.3: (Figure on page 45) Differences in precipitation and surface winds for precession (a, b) and obliquity (c, d) for boreal summer (JJA, a, c) and boreal winter (DJF, b, d). Note that the precipitation scale does not have equally sized steps. The unit vector length is 4.5 m/s. These are averages of the last 50 years of the experiments

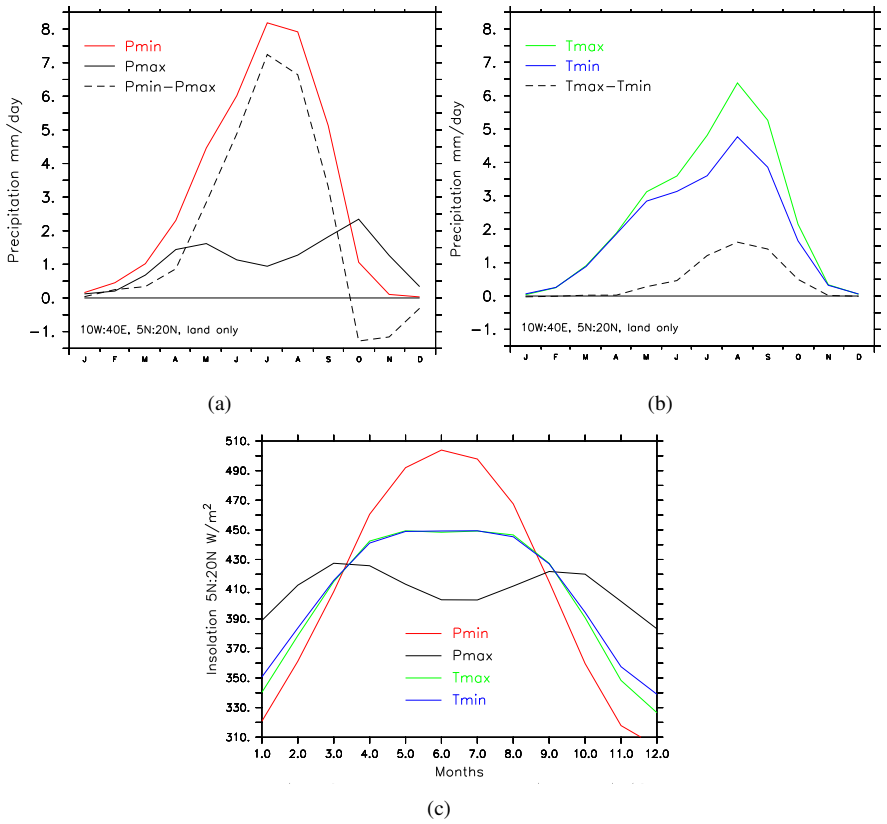

Figure 3.4: Precipitation over North-Africa, land only, in mm/day for precession (a) and obliquity (b). Differences are given by the dashed lines. Insolation over the tropics (5-20°N averaged) is given in (c) for each experiment

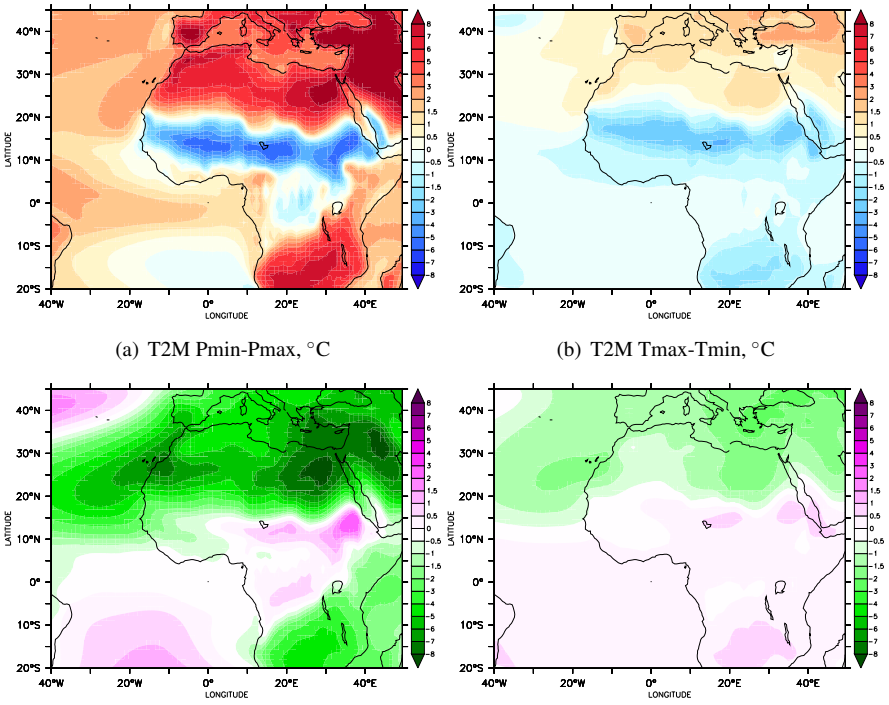

(a) T2M Pmin-Pmax, °C

(b) T2M Tmax-Tmin, °C

(c) SLP Pmin-Pmax, hPa

(d) SLP Tmax-Tmin, hPa

Figure 3.5: Differences in surface air temperature (T2M; a, b) and sea level pressure (SLP; c, d) for the two precession (a, c) and obliquity (b, d) extremes. All are JJA averages

Northerly winds into the north-eastern Sahara are stronger as well, in response to the strengthened low pressure areas over the Sahara.

The strong increase in the monsoonal south-westerlies (Figure 3.3(a)) suggests that the tropical Atlantic is the major source for the enhanced precipitation. To investigate this, we examine changes in precipitation, evaporation and moisture transport. Over the continent, changes in local recycling play only a small role; evaporation is increased over the continent by only 2-3 mm/day (Figure 3.6(c)). Although this evaporation increase is an important factor cooling the surface (see above), the changes are not large enough to explain the precipitation changes (up to 10-12 mm/day, Figure 3.6(a)). Calculating (ΔP - ΔE)/ΔP, where Δ is the Pmin-Pmax difference for 10°W:40°E, 5°N:20°N, land only, shows that during JJA 72% of the precipitation increase is due to moisture advection from outside this area. Increased evaporation over the nearby Atlantic could explain enhanced moisture advection into North-Africa. However, evaporation is reduced at 10-20°N over the Atlantic (Figure 3.6(c)), where the trade winds turn more landward and lose some of their speed. Near the south-western coast evaporation is reduced as well, due to increased

upwelling and lower SSTs. Over the western tropical Atlantic there is an increase in evaporation (up to 1.5 mm/day) which, together with the decrease in precipitation (up to 8 mm/day) over the south-western tropical Atlantic (see Figures 3.6(a), 3.6(c)), results in a larger moisture transport towards the continent. Figure 3.6(e) shows the changes in moisture transport **Q**, the mass-weighted vertical integral of specific humidity q multiplied by horizontal wind **v**. There is more moisture transport into North-Africa over the south-west, in agreement with the stronger monsoonal south-westerlies (Figure 3.3(a)) and increased specific humidity over North-Africa and the eastern Atlantic (not shown). Southerly cross-equatorial moisture transport is increased in relation to the increased cross-equatorial southerly winds and a reduction in precipitation as well as a slight increase in evaporation over the tropical southern Atlantic. Moisture advection from the north over north-eastern North-Africa is also slightly increased. Changes in specific humidity over the Mediterranean and Europe are small (not shown) so increased moisture transport from the north is mainly due to increased northerly winds. Over north-western North-Africa the increased precipitation (Figure 3.3(a)) is related to increased moisture transport from the Sahara and the northern monsoon region (Figure 3.6(e)), not to increased moisture transport from the Atlantic trade winds. (ΔP - ΔE)/ΔP over 15°W:0°E, 25°N:35°N, land only, is 25%, indicating that local recycling plays a large role over this region. Changes in net precipitation, P-E, shown in Figure 3.6(e), are very similar to the changes in precipitation over North-Africa (Figure 3.6(a)), again illustrating that evaporation changes do not play a large role.

Changes in the upper level circulation also play a fundamental role in the precipitation changes at the surface. Most of the monsoon precipitation is convective, so it is no surprise that upward velocities over land are increased while over the ocean there is a reduction in upward velocities (Figure 3.7(a)). During Pmin, maximum convection occurs over the continent at 10-15°N at 400-500 hPa height, extending north up to 20°N, while during Pmax convection maxima lie over the tropical Atlantic at 700-800 hPa (see Figures 3.12 and 3.13 for vertical velocity in each experiment). Over land, convection does not occur north of 15°N during Pmax. Like precipitation, convection over continental tropical Africa follows the local insolation forcing and shows a double peak in spring and autumn during Pmax, and a single peak in summer during Pmin (see Figures 3.4(a) for precipitation and 3.4(c) for insolation). Over the north-eastern Sahara, subsidence is weaker during Pmin in summer.

Figure 3.7(a) suggests a northward shift of convection (indicated by negative values), which is consistent with the northward shift of the monsoon rains and the northward shift of the Saharan surface lows. At these lows the south-easterly monsoon winds converge with the dry northerly winds to form the ITCZ, the InterTropical Convergence Zone. The ITCZ is located roughly 5° further north during Pmin, at ∼22°N. Convection over the ITCZ is shallow and most precipitation is associated with a core of stronger and deeper ascent south of the ITCZ, at ∼10°N (Figure 3.13). During Pmax, convection is strongest in the lower troposphere at 10-15°N, roughly overlying the ITCZ, but there is barely any precipitation at this latitude (Figure 3.8).

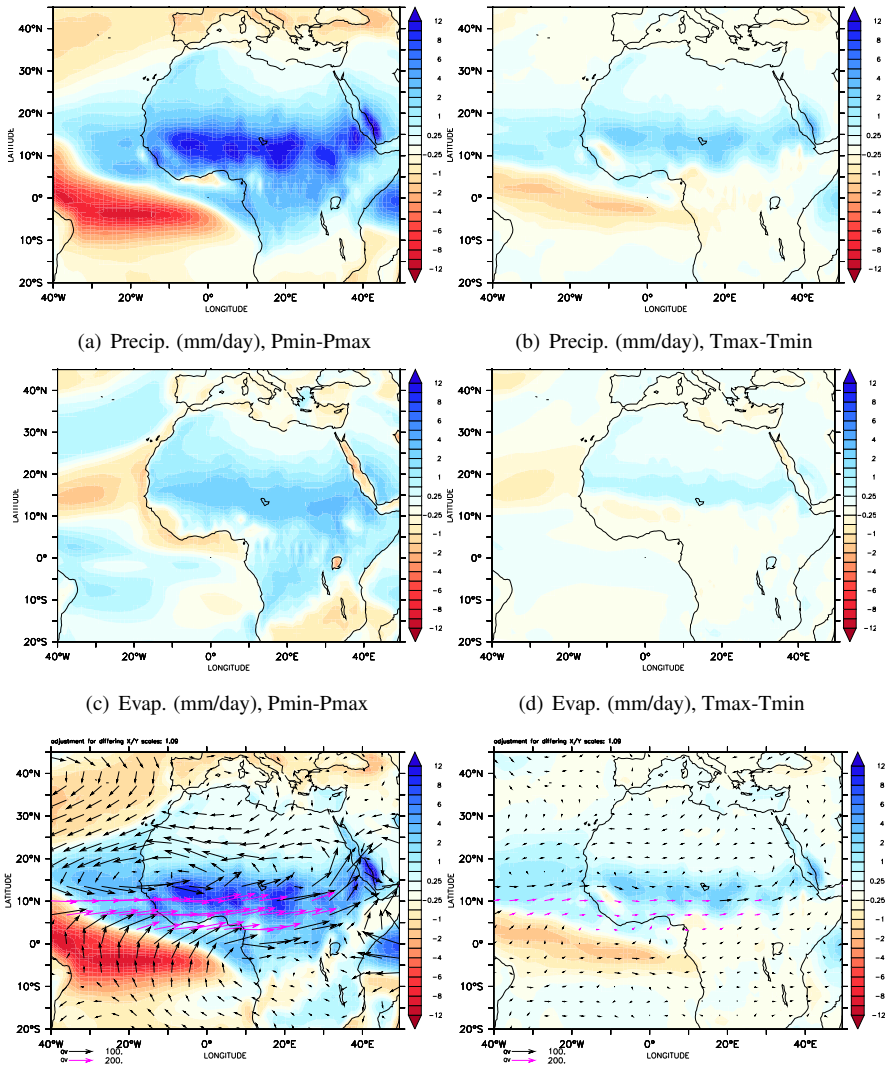

(a) Precip. (mm/day), Pmin-Pmax

(b) Precip. (mm/day), Tmax-Tmin

(c) Evap. (mm/day), Pmin-Pmax

(d) Evap. (mm/day), Tmax-Tmin

(e) P-E (mm/day) and **Q** (kg/(ms)), Pmin-Pmax

(f) P-E (mm/day) and **Q** (kg/(ms)), Tmax-Tmin

Figure 3.6: Differences in JJA precipitation (a,b), evaporation (c,d), net precipitation (P-E, colours) and moisture transport (**Q**, vectors, integrated from the surface to 10 hPa) in (e,f) for precession (a,c,e) and obliquity (b,d,f). Notice that two vector lengths are used in (e,f): purple vectors indicate **Q** larger than 200 kg/(ms)

Most of the precipitation occurs over the Atlantic, consistent with the pattern of vertical motion at 500 hPa (Figures 3.8, 3.12). In agreement with the northward shift of convection during Pmin the African Easterly Jet (Nicholson, 2009) is located further north, at 15-20°N and 500 hPa. During Pmax, the AEJ is located at 5-10°N and 600-700 hPa, but it is stronger (not shown), further decreasing the moisture content over continental North-Africa.

Changes in circulation are summarised in Figure 3.7(c). It shows the northward shift in convection, with reduced convection over the ocean and increased convection over land (Figure 3.7(a)). Convection is stronger in the upper troposphere at 10-15°N during Pmin, while below that the positive contours indicate the stronger but shallow convection during Pmax (Figure 3.13). North of the monsoon region, at 20-30°N, shallow convection is larger during Pmin, when the Saharan surface lows and the ITCZ are located further north. In the upper troposphere, the negative contours indicate reduced subsidence over the Sahara.

3.3.3 The North-African Monsoon: Obliquity

The obliquity-induced insolation changes over the tropics during boreal summer are small, (< 5 Wm^{-2}, see Figures 3.1(b) and 3.4(c)). In terms of percentage the insolation difference is less than 1% (0.27% for JJA 0°N:30°N). Nonetheless, the obliquity-induced precipitation change is 25% (averaged over 0°N:30°N, 20°W:50°E, land only, JJA). This precipitation change (Figure 3.3(c)) must therefore either originate at higher latitutes, as suggested by Tuenter et al. (2003), or be induced by changes in the meridional insolation gradient (Chapter 5), which is stronger during Tmax when NH summer insolation is increased and SH winter insolation is decreased. The JJA averaged insolation gradient between 23°N and 23°S is 17.5 Wm^{-2}stronger during Tmax.

The climatologies of Tmax and Tmin are overall much more alike than those of Pmin and Pmax, because of the small insolation differences over the tropics. For precipitation, the annual cycle is slightly stronger during Tmax (Figure 3.4(b)). Precipitation also extends further north during Tmax, reaching just over 20°N (based on the 1 mm/day contour for JJA, see Figure 3.8). Along the western coast precipitation is increased by 0.5-1 mm/day up to the Atlas mountains. During Tmin, precipitation reaches just north of 15°N. Over land, the differences are up to 2-3 mm/day at 10-15°N (see Figure 3.3(c)).

Changes in temperature show a meridional pattern, see Figure 3.5(b). Temperatures on the southern hemisphere are reduced due to lower insolation, while on the northern hemisphere temperatures are increased due to higher insolation (Figure 3.9). Over North-Africa, lower temperatures extend up to 20-25°N, as the surface is cooled through feedbacks within the monsoon system, similar to the response to precession, see Section 3.3.2. There is a reduction in surface downward shortwave radiation of 20.7 Wm^{-2} (an order of magnitude larger than the local insolation increase) due to increased cloudiness and a stronger surface latent heat flux of 5.5 Wm^{-2} due to increased evaporation (see Table 3.1), resulting in surface temperat-

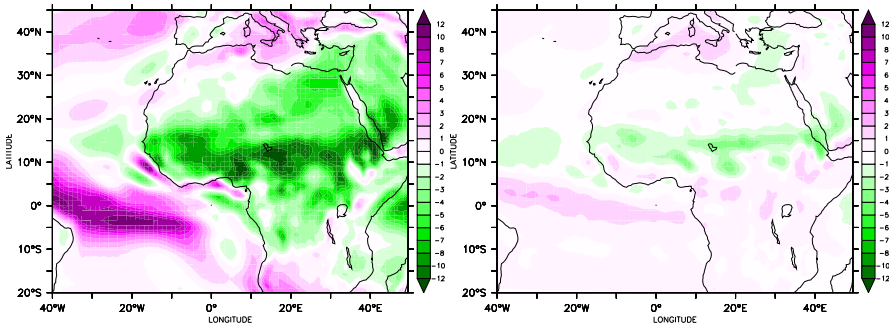

(a) ω (500 hPa) Pmin-Pmax, 10^{-2} Pa/s

(b) ω (500 hPa) Tmax-Tmin, 10^{-2} Pa/s

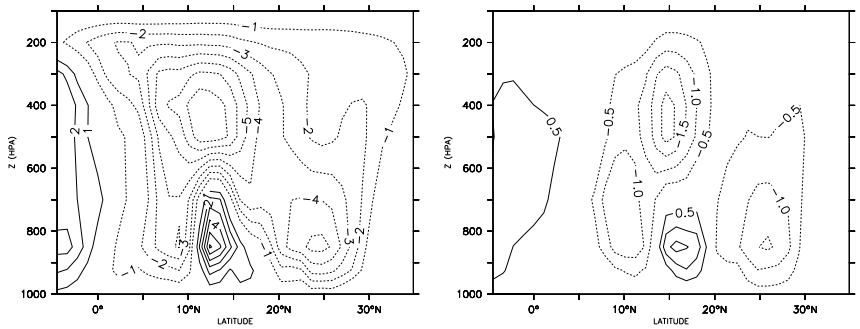

(c) ω 30°W:40°E Pmin-Pmax, 10^{-2} Pa/s

(d) ω 30°W:40°E Tmax-Tmin, 10^{-2} Pa/s

Figure 3.7: Differences in ω, vertical velocity in pressure coordinates at 500 hPa (a, b) and zonally averaged (30°W:40°E; c, d) for precession (a, c) and obliquity (b, d). Negative values indicate an increase in upward motion. All are JJA averages. Note that the contour interval in Figure 3.7(d) is smaller than in Figure 3.7(c)

ures of up to 3° lower. Sea surface temperatures (not shown) show a response very similar to surface air temperature, with further lowering of SSTs along the coast of North-Africa due to increased upwelling related to increased surface winds.

Pressure changes closely follow the temperature changes (Figure 3.5(d)). Pressure is up to 2 hPa lower over the north-east and over the western coast, where the Azores High is weakened. The monsoon winds are stronger and drawn slightly further north in response to the reduced pressure over the northern Sahara, see Figures 3.3(c) and 3.10. A strengthened South Atlantic subtropical high strengthens the cross-equatorial pressure gradient and forces more southerly cross-equatorial winds into the monsoon region, in agreement with a stronger cross-equatorial insolation gradient (Chapter 5).

Similar to the monsoonal response to precession, the increased south-westerlies into North-Africa and the reduced precipitation over the tropical Atlantic (Figure 3.3(c)) suggest that the tropical Atlantic is the main moisture source for the enhanced monsoonal precipitation. Indeed, moisture transport **Q** is increased over the south-west coast into North-Africa, see Figure 3.6(f). A small part of this increase comes from the southern tropical Atlantic due to the stronger cross-equatorial southerly winds. Specific humidity over the SH, where insolation is decreased, is lower (not shown). The increased landward moisture transport is therefore mostly due to stronger monsoonal winds and a decrease of precipitation over most of the tropical and southern Atlantic, and for a small part increased evaporation over the tropical Atlantic (Figure 3.6(d)). Over the north-eastern Sahara there is a slight enhancement of northerly moisture transport, which is mainly due to increased northerly winds. Specific humidity is only slightly higher over the Mediterranean and Europe, the largest changes in specific humidity, q, occur over the monsoon region. Over the north-west, moisture transport is more north-westward during Tmax and moisture transport in the trades is weaker (Figure 3.11). Increased precipitation over north-westernmost North-Africa (Figure 3.6(b)) is therefore related to increased moisture transport from the Sahara and northern monsoon region, as well as increased evaporation; (ΔP - ΔE)/ΔP is 14% over 15°W:0°E, 25°N:35°N (land only). Over the monsoon region, increased moisture advection is the main reason for increased precipitation. (ΔP - ΔE)/ΔP is 81 % (for 10°W:40°E, 5°N:20°N, land only). The pattern of changes in net precipitation, P-E, is very similar to the pattern of changes in precipitation (Figures 3.6(b) and 3.6(f)), further indicating that evaporation changes are of minor importance within the monsoon region.

Changes in the upper atmosphere consist of reduced convection over the tropical Atlantic, where precipitation is reduced, and increased convection over land (Figure 3.7(b)) during Tmax. Convection is slightly stronger ($\sim$1-2 10^{-2} Pa/s) and extends slightly further north over the continent than during Tmin (Figure 3.12), while convection is weaker over the Atlas mountains. Decreased subsidence occurs over the north-eastern Sahara and eastern Mediterranean. Similar to the precession-induced changes there is a northward shift in the ITCZ, overlaying the Saharan surface lows where the monsoon winds converge with the drier northerly winds, as well as a northward shift of the band of precipitation (Figure 3.6(b)), associated with

a deeper core of ascent (Figure 3.13). Maximum ascent occurs at approximately 500 hPa, just north of 10°N during Tmax and just south of 10°N during Tmin (Figure 3.13). This is consistent with a more northward location of the AEJ, which is also slightly stronger during Tmax (not shown).

Figure 3.7(d) shows the changes in ω in the vertical, also illustrating the northward shift of convection. Convection is generally stronger during Tmax, but during Tmin shallow but stronger convection occurs at 15-20°N over land (Figure 3.13). Subsidence north of the monsoon is weaker while shallow convection over the ITCZ is stronger during Tmax.

3.4 Discussion & Conclusions

This study is the first to investigate the response of the North-African monsoon to the separate precession and obliquity signals using a fully coupled, high-resolution GCM (EC-Earth). We find both signals in the monsoon, with a stronger monsoon when Northern Hemisphere summer insolation is higher. During Pmin and Tmax monsoonal precipitation is stronger and further northward due to stronger monsoonal south-westerlies, corresponding to stronger heat lows over the Sahara and a stronger cross-equatorial pressure gradient. Precipitation over the tropical Atlantic is reduced, and more moisture is transported landwards. There is also slightly more moisture advection from the north, but this increase plays a smaller role than the increased moisture advection from the tropical Atlantic. The upper level circulation generally shifts northward, with the ITCZ, the African Easterly Jet (AEJ) and the the belt of convective precipitation located further north during Pmin and Tmax than during Pmax and Tmin.

The precession-induced insolation changes consist of a large increase in NH summer insolation (Figure 3.1(a)) of up to 100 Wm^{-2}. An insolation increase of 21% causes a precipitation increase of 471% (averaged over 0°N:30°N JJA). The similarity of the seasonal cycles of precipitation and convection to the seasonal cycle of insolation over the tropics, with a single summer peak during Pmin and two peaks in spring and autumn during Pmax, suggests that precipitation responds strongly to the local insolation forcing. However, we also find an increased South Atlantic subtropical high, pushing more southerly winds and more moisture from the SH into the North-African monsoon region during Pmin.

For obliquity, the insolation change over the tropics during NH summer is very small (< 5 Wm^{-2}). Insolation is increased by 0.27% during Tmax, while precipitation is enhanced by 25% (averaged over 0°N:30°N, JJA). The cross-equatorial insolation gradient, increased by 17.5 Wm^{-2} during Tmax (23°N:23°S JJA), may therefore play an important role for obliquity. The South Atlantic subtropical high is stronger, pushing more southerly winds into the monsoon region. Specific humidity over the southern Atlantic is lower because of reduced SH austral winter insolation, but a slight increase in equatorial Atlantic evaporation on both sides of the equator results in increased moisture transport from both the southern and northern equat-

orial Atlantic into the monsoon region. For precession, specific humidity over the southern Atlantic is increased during JJA due to higher insolation. Therefore the precession-induced increase in moisture transport into the monsoon region is larger than the obliquity-induced increase, not only because of the stronger response of the monsoonal south-westerlies and a stronger evaporation increase over the equatorial Atlantic, but also because of increased humidity over the SH.

The increased south-westerly monsoon winds and moisture flux, as well as the redistribution of precipitation from ocean to land is in agreement with previous studies, such as Braconnot et al. (2008); Clement et al. (2004); Erb et al. (2013); Khon et al. (2010); Mantsis et al. (2013); Merlis et al. (2013b); Prell and Kutzbach (1987); Tuenter et al. (2003). There are differences, however. None of these studies show a summer precipitation increase over north-westernmost Africa, which we find in EC-Earth mostly for precession. Given the patterns of wind and moisture transport we suggest that this precipitation increase could be the result of enhanced moisture advection from the monsoon region, opposite to the findings of van der Laan et al. (2005). However, further investigation is necessary to quantify the role of moisture transport from the Atlantic through low pressure systems, which are not visibile in the monthly averages used here. Prell and Kutzbach (1987) and Tuenter et al. (2003) suggest that the increased south-westerly monsoon winds into North-Africa are remotely forced by reduced pressure over Asia. In EC-Earth we also find a pressure reduction over northern Africa as well as over continental Asia (not shown), but we do not see continued south-westerly / westerly winds or moisture transport reaching from the south-west coast of North-Africa into Asia. This could be related to the relatively low resolution, and therefore reduced orography, in the models used by Prell and Kutzbach (1987) and Tuenter et al. (2003). Low resolution could also explain why the double precipitation peak over tropical North-Africa during a precession maximum is not present in EC-Bilt (Tuenter et al., 2003), because in EC-Bilt the tropics consist of only a few grid boxes. The higher resolution of EC-Earth enables the model to respond better to the different annual cycle in insolation forcing within and outside of the tropics. Also, EC-Bilt shows a smaller precipitation response to the insolation forcing, 101% and 8.9% for precession and obliquity respectively (E. Tuenter pers.comm.), for insolation changes of 20.1% and 0.27%, compared to 471% and 25.1% for EC-Earth (0°N:30°N JJA).

Another notable difference with Tuenter et al. (2003) is that in their study increased moisture transport from the north plays an important role in bringing the precession and obliquity signals into the monsoon region. They used a quasi-geostrophic model that has very little transport of moisture and energy across the equator, which could explain the importance of remote high latitude forcing as well as the smaller precipitation change in their study. In EC-Earth, humidity changes north of the monsoon region are small, and increased moisture transport from the north is much less important than the increased transport from both the northern and southern tropical Atlantic for both precession and obliquity.

Moreover, EC-Earth v2.2 lacks dynamic ice sheets, so the obliquity signal in the North-African monsoon in our study does not originate from (high-latitude) glacial

fluctuations, as is often assumed in the interpretation of paleoclimate records. Our findings imply a more direct response of tropical climate to obliquity changes, in agreement with studies that find only a short time lag with respect to obliquity and those that find obliquity signals in warm climate conditions (i.e. prior to ice age dominated climates of the past 3 Ma). A more detailed discussion on how obliquity influences low-latitude climate at all longitudes can be found in Chapter 5.

An important component that is not yet included in the EC-Earth model, besides dynamic ice sheets, is dynamic vegetation, which could alter the monsoonal response to orbital forcing. Especially over the Sahel and the Sahara vegetation is likely to increase given the large orbital-induced precipitation enhancement (Figures 3.3(a), 3.3(c)). Several studies show, for the Mid-Holocene, the positive feedbacks of a lower albedo (e.g. Bonfils et al., 2001) as well as an increased sensible heat flux due to increased roughness length and an increased latent heat flux due to increased evapotranspiration (e.g. Levis et al., 2004; Texier et al., 2000). Thus, including vegetation would likely increase the monsoonal response to orbital forcing.

To conclude, we argue that both the precession and obliquity signal in the North-African summer monsoon originate from enhanced moisture transport from the tropical Atlantic. The precession-induced changes are stronger, as the insolation change is much larger than for obliquity. Considering the near-zero obliquity-induced tropical insolation changes, we propose that the cross-equatorial insolation gradient may play an important role for obliquity. We therefore disagree with the remote mid- to high-latitude forcing of Tuenter et al. (2003).

3.A Appendix: absolute figures

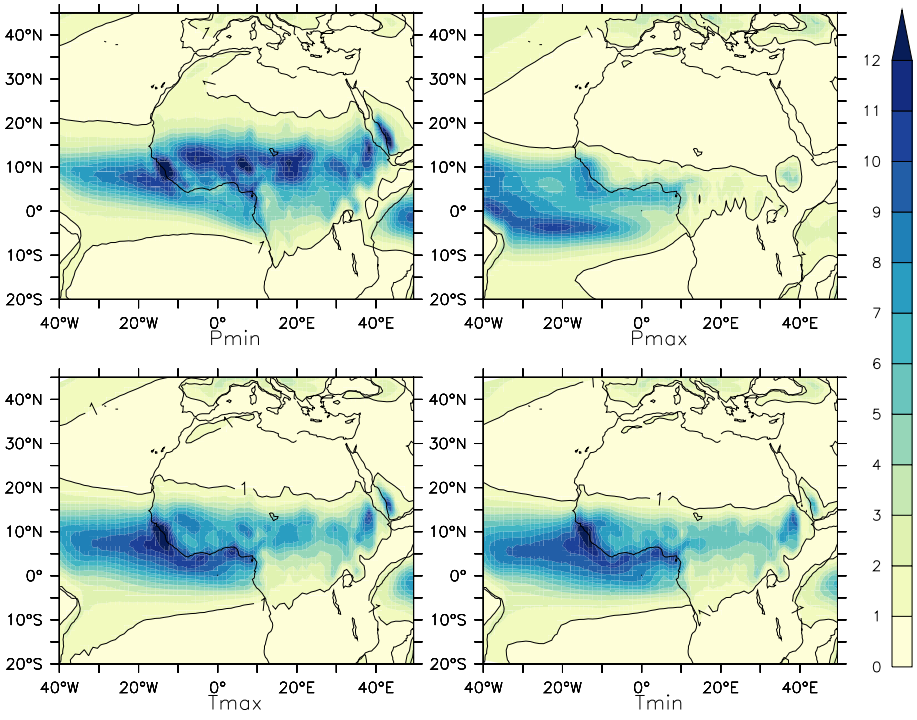

Figure 3.8: JJA precipitation in each experiment, mm/day. The 1 mm/day contour is given for each experiment

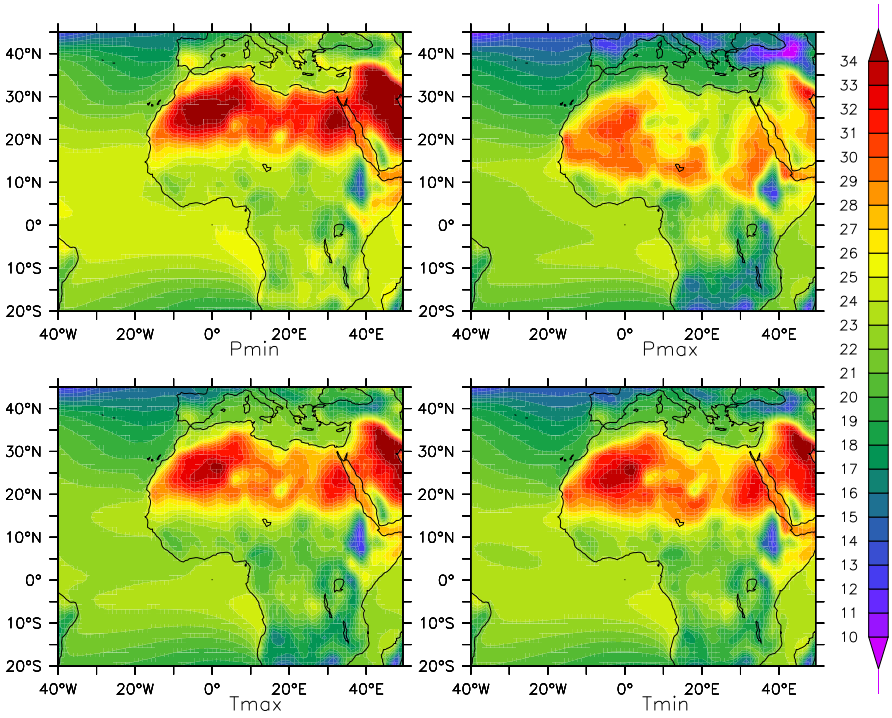

Figure 3.9: JJA surface air temperature in each experiment, °C

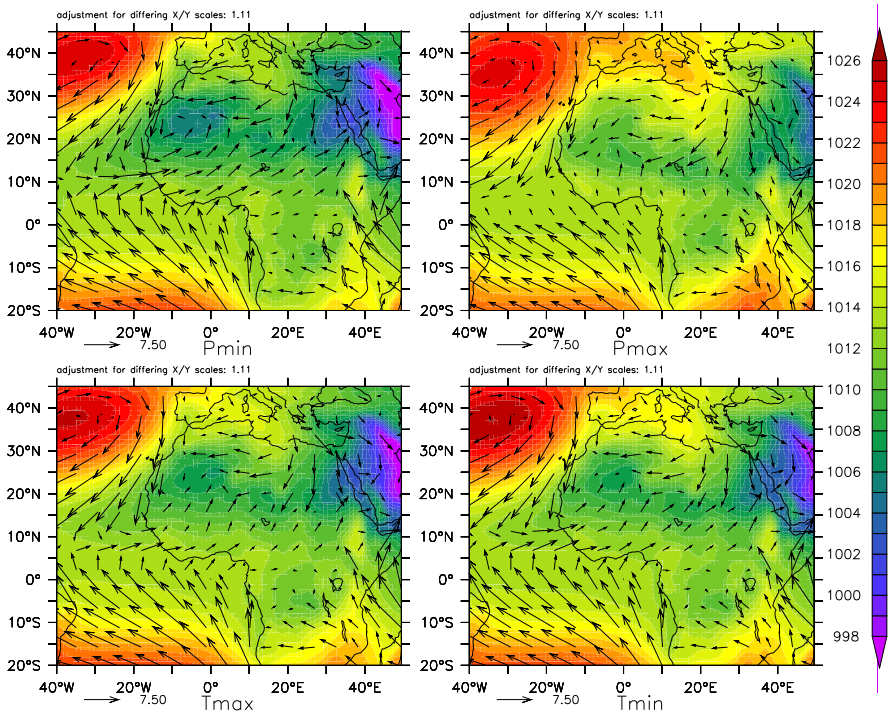

Figure 3.10: JJA sea level pressure (colour scale, hPa) and surface wind (vectors, m/s) in each experiment

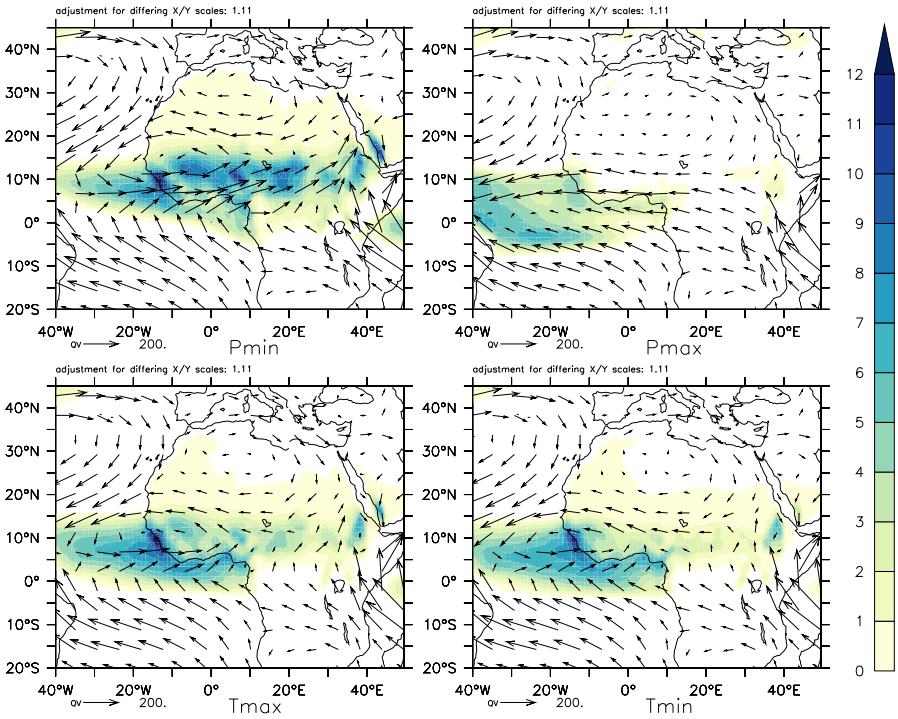

Figure 3.11: JJA moisture transport **Q** (vectors, kg/(ms), integrated from the surface to 10 hPa) and net precipitation P-E (colour scale, mm/day) in each experiment

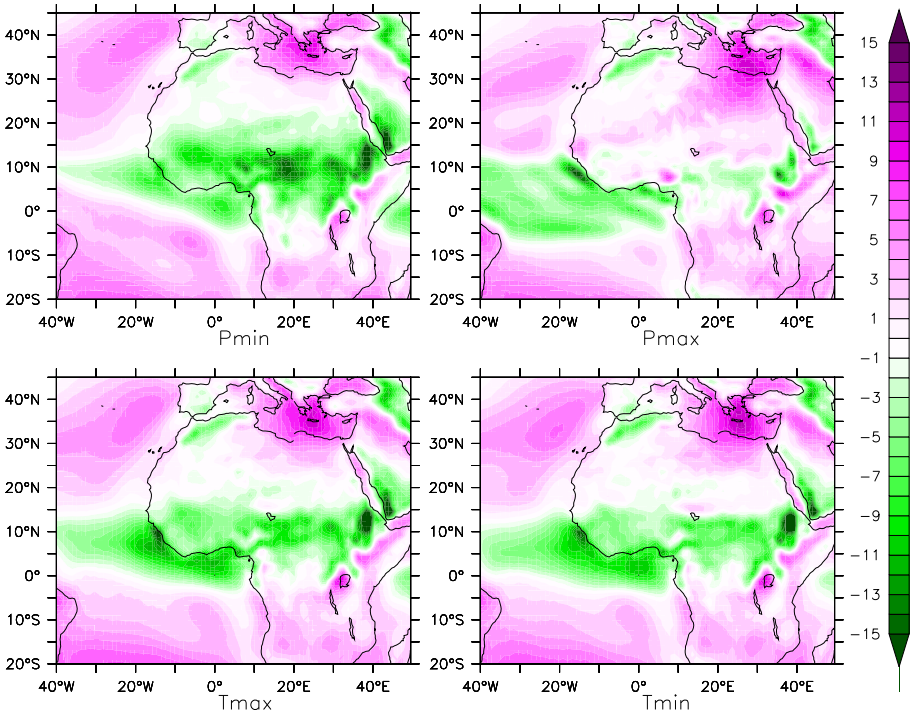

Figure 3.12: JJA vertical velocity at 500 hPa, in each experiment, 10^{-2} Pa/s. Positive values indicate subsidence, negative values indicate upward motion

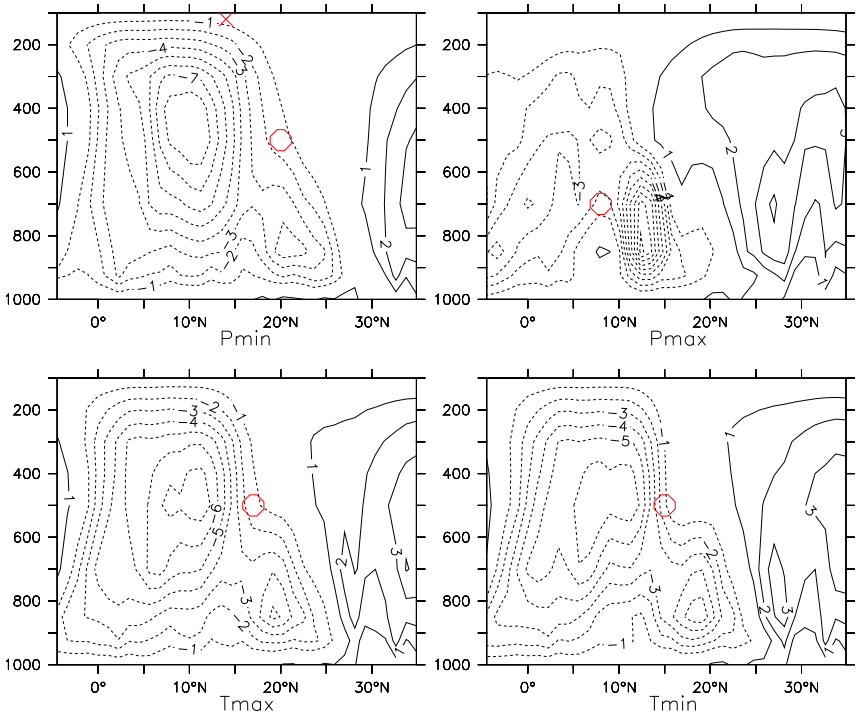

Figure 3.13: JJA vertical velocity, 30°W:40°E averaged, in each experiment, 10^{-2} Pa/s. Negative contours indicate upward motion. The locations of the African Easterly Jet and Tropical Easterly Jet are indicated by the red circle and cross, respectively, based on maxima in JJA 10°W:10°E easterly winds. The tropical easterly jet is only well-defined in experiment Pmin

4

Response of the Asian summer monsoons to extreme precession and obliquity forcing

Abstract

We examine the response of the Indian and East Asian summer monsoons to separate precession and obliquity forcing using a fully coupled high-resolution model, EC-Earth. We focus on the effect of insolation changes on monsoon precipitation and underlying circulation changes. Our results show increased summer monsoon precipitation at times of increased summer insolation, i.e. minimum precession and maximum obliquity, accompanied by a redistribution of precipitation and convection from ocean to land. Southerly monsoon winds over East Asia are strengthened as a consequence of an intensified land-sea pressure gradient. The response of the Indian summer monsoon is more complex, there is no simple intensification of the land-sea pressure gradient. Surface pressure is enhanced over south-east Asia and an Indian Ocean Dipole pattern emerges, with increased precipitation and convection over the western tropical Indian Ocean. Increased temperatures and reduced surface pressure occur during minimum precession, but not during maximum obliquity when insolation is reduced over the tropics and southern hemisphere during northern hemisphere summer. Evaporation is reduced over the northern Indian Ocean, which together with increased precipitation over the western Indian Ocean damps the increase of monsoonal precipitation over the continent. The southern tropical Indian Ocean acts as a moisture source for enhanced monsoonal precipitation. Our results show a direct response of both Arabian Sea upwelling and southern Indian Ocean evaporation, which is in contrast to what proxy climate records suggest.

This chapter is in preparation for publication as: Bosmans, J.H.C., S.S. Drijfhout, E. Tuenter, F.J. Hilgen and L.J. Lourens (2014). Response of the Asian summer monsoons to extreme precession and obliquity forcing

4.1 Introduction

Monsoon systems play a key role in Asian climate, representing a strong seasonal climate signal over an area spanning from the Arabian to the Chinese Seas. The summer monsoon is driven by the seasonal cycle of incoming solar radiation, the land/sea thermal contrast and the release of latent heat through condensation. On time scales of 10^3-10^5 years the Asian monsoons are dominated by changes in the distribution of incoming solar radiation (insolation) over seasons and latitudes, the so-called orbital or Milankovitch cycles. Precession controls the seasonality of insolation at all latitudes and is modulated by the eccentricity of the Earths orbit, while obliquity (tilt) affects mostly high latitude summer insolation and meridional insolation gradients. All three orbital parameters (precession, eccentricity and obliquity) are observed in proxy climate records of monsoon strength. Examples of such records are oxygen isotope stalagmite records from east China (e.g. Wang et al., 2008), dominated by precession cyclicity, as well as the multi-proxy stack of Indian summer monsoon circulation strength from the western Arabian Sea, where southwesterly summer monsoon winds influence upwelling, productivity and sedimentation (e.g. Clemens and Prell, 2003). The latter shows a strong obliquity signal, despite the dominance of precession in low-latitude summer insolation.

Modelling studies corroborate the strengthening (weakening) of summer monsoons at times of orbitally forced high (low) summer insolation. In some of the earliest paleoclimate modelling studies, atmosphere-only models showed a strengthened thermal low over the continents and a stronger land/sea thermal contrast, causing increased summer monsoon precipitation at times of high summer insolation (e.g. Kutzbach and Guetter, 1986; Kutzbach and Otto-Bliesner, 1982; Prell and Kutzbach, 1987). More recently several studies of the Mid-Holocene, a time of enhanced Northern Hemisphere insolation seasonality, were performed within the framework of the Paleoclimate Modelling Intercomparison Project (Braconnot et al., 2007a). During the Mid-Holocene, models show a stronger Indian Summer Monsoon (ISM) and East Asian Summer Monsoon (EASM). The EASM strengthening is related to a stronger land/sea pressure gradient (Jiang et al., 2013; Wang and Wang, 2013; Zheng et al., 2013). Strengthening of the ISM may be affected by mechanisms such as the Indian Ocean Dipole (Abram et al., 2007; Zhao et al., 2005). Other studies of periods with a precession-induced increase in insolation seasonality have also demonstrated a strengthening of the ISM (Braconnot and Marti, 2003; Braconnot et al., 2008).

Only a few studies have investigated the separate precession and obliquity forcing instead of focussing on a specific time with combined precession and obliquity forcing. Tuenter et al. (2003) showed a deepening of the convergence zone over southern Asia and increased summer precipitation over the Asian monsoon regions during both minimum precession and maximum obliquity (both times of increased summer insolation). Similar precipitation changes are identified by Erb et al. (2013). Mantsis et al. (2013) report increased precipitation during minimum precession as

well, which for East Asia is related to an increased land/sea pressure gradient. Chen et al. (2011) focus solely on obliquity, showing that the ISM and the South-EASM are stronger during maximum obliquity, while the North-EASM is weaker. This weakening of the North-EASM arises through a teleconnection linked to the formation dynamics of the Bonin High, implying that orbital forcing of monsoon strength is more complicated than only changing the large scale land/sea thermal contrast. Other studies have also found that the orbital-induced changes in surface pressure over the Asian monsoon regions do not show a simple change in land/sea pressure differences (Chen et al., 2011; Mantsis et al., 2013; Zhao et al., 2005).

The link between orbitally forced changes in insolation and monsoon strength has thus been established by both proxy climate records and modelling studies. Questions however remain, concerning the timing with respect to the forcing (e.g. Braconnot and Marti, 2003; Clemens and Prell, 2003; Wang et al., 2008), the detailed pattern of monsoon response (e.g. Zhao et al., 2005) and the role of obliquity, which has very little influence on low-latitude insolation yet strongly affects monsoon strength (e.g. Tuenter et al., 2003).

In this study we address the latter two questions by assessing the detailed pattern of the ISM and EASM response to both precession and obliquity forcing using a high-resolution fully coupled general circulation model, EC-Earth. With its sophisticated parametrizations (Hazeleger et al., 2010, 2011) and unprecedented atmospheric resolution in paleo-climate modelling ($\sim$1.125°) EC-Earth has already shed new light on the response of the North-African monsoon to orbital forcing (Chapter 3, Bosmans et al. 2014). Here we address the response of ISM and EASM precipitation and the underlying mechanisms, and give a brief comparison to the response of the North-African monsoon (Section 6.4).

This paper is organised as follows: Section 6.2 describes the EC-Earth model and the experimental set-up. Section 4.3 shows the changes in monsoon precipitation and associated circulation, with Section 4.3.1 focussing on precession and Section 4.3.2 focussing on obliquity. A discussion and conclusion are given in Sections 6.4 and 6.5.

4.2 Model and Experiment set-up

4.2.1 The model: EC-Earth

EC-Earth is a fully coupled ocean-atmosphere GCM (general circulation model, Hazeleger et al. 2010, 2011). The atmospheric part of EC-Earth 2.2 is based on the Integrated Forecasting System (IFS), cycle 31R1, of the European Centre for Medium-range Weather Forecast (ECMWF). Its horizontal resolution is T159 (roughly 1.125°x1.125°) with 62 vertical levels. IFS cycle 31R1 has the Bechtold et al. (2008) convection scheme and the Balsamo et al. (2009) land surface scheme H-TESSEL, which includes surface runoff. The ocean component consists of NEMO, version 2, running at a horizontal resolution of nominally 1° with 42 vertical levels. NEMO in-

corporates the sea-ice model LIM2 (Madec 2008; Sterl et al. 2011). The ocean, ice, land and atmosphere are coupled through the OASIS3 coupler (Valcke and Morel, 2006).

EC-Earth performs well for the present-day compared to CMIP3 models and data in terms of climatology as well as interannual, spatial and temporal variability (Hazeleger et al., 2010, 2011). More importantly, we have previously shown that monsoons are represented well in both the pre-industrial and the Mid-Holocene paleo-experiment (Chapter 2, Bosmans et al. 2012).

4.2.2 Experimental set-up: insolation forcing and boundary conditions

This study is based on the same experiments as those described and used in Chapter 3; a brief overview of the experiments is repeated here. Four time-slice experiments are performed to examine the separate precession and obliquity signals, details of which can be found in Table 1.1.

During a precession minimum (Pmin) the summer solstice occurs in perihelion (the point closest to the Sun), so seasonality is enhanced on the Northern Hemisphere and reduced on the Southern Hemisphere. The opposite occurs during a precession maximum (Pmax), when winter solstice occurs in perihelion. In the obliquity experiments, eccentricity is set to zero to completely eliminate the effect of precession. During an obliquity maximum (Tmax, T for tilt), both northern and southern hemisphere (NH, SH) summers receive more insolation, especially at the poles, while during an obliquity minimum (Tmin) summer insolation is reduced. During NH summer, insolation is increased on both hemispheres during Pmin compared to Pmax, while during Tmax insolation is increased on the NH and decreased on the SH compared to Tmin. Insolation differences at $\sim$40°N can be as large as 100 Wm^{-2} for precession and 20 Wm^{-2} for obliquity (see Figure 3.1). The values of the orbital parameters in each experiment is given in Table 1.1. These are the same as the P-T-, P+T-, P0T+, P0T- experiments in Tuenter et al. (2003), and are based on the extreme values of the orbital parameters occuring in the last 1 Ma (Berger, 1978).

Within each experiment, the orbital forcing is fixed. All other boundary conditions (e.g. greenhouse gas concentrations, orography, ice sheets, vegetation) are kept constant at pre-industrial levels. We keep vernal equinox fixed at 21 March and use the present-day calendar. This introduces some errors in the precession experiments, because the lengths of the seasons and the dates of the equinoxes and solstices change along the precession cycle (Joussaume and Braconnot, 1997). A celestial calendar, using angular months, would be more appropriate. However, because Tuenter et al. (2003), and others (e.g. Braconnot et al., 2008; Chen et al., 2011), also use the present-day calendar, we maintain this calendar to facilitate comparison.

In this study we compare Pmin to Pmax, and Tmax to Tmin, i.e. we investigate

the effect of increased summer and decreased winter insolation. These experiments were initiated from a pre-industrial control experiment. Each experiment is run for 100 years, of which the last 50 years are used to create the climatologies shown in this study. This is long enough for top-of-atmosphere net radiation as well as atmospheric and surface variables that are of interest to equilibrate to the forcing (see Chapter 3). The globally averaged tendency term of surface air temperature, dT/dt, is near-zero and shows no trend in all experiments (not shown).

4.3 Results

In this section we first investigate the precession-induced changes in the Asian monsoons (Section 4.3.1), followed by the obliquity-induced changes (Section 4.3.2). We compare maximum to minimum NH summer insolation, i.e. Pmin to Pmax and Tmax to Tmin, using JJA averages.

4.3.1 Precession

The precession-induced insolation change reaches 100 Wm^{-2} in June (Figure 3.1, Bosmans et al. 2014; Tuenter et al. 2003). The JJA averaged insolation between 10°N and 40°N is ∼80 Wm^{-2} higher during Pmin than Pmax. Figure 4.1(a) shows that the average summer precipitation over monsoonal Asia is up to 3 mm/day higher during Pmin. Furthermore, in line with the insolation forcing, the seasonality is greater in Pmin. The largest precipitation changes occur over the Himalaya, with differences reaching up to 15 mm/day in JJA over the eastern end of the Himalaya, see Figure 4.2. The rest of India, as well as most of the Asian Peninsula and China are wetter as well. Over the eastern Indian Ocean, Bay of Bengal and the Chinese Seas precipitation is weaker during Pmin; these areas receive more precipitation during Pmax. However, the increased monsoonal precipitation over the continent during Pmin is not simply due to a redistribution of precipitation from ocean to land, as the western Indian Ocean and the Arabian Sea are wetter during Pmin, up to 6 mm/day.

To assess the precipitation changes in more detail, we first investigate changes in surface temperature, surface pressure and surface winds. The hydrological cycle and upper level circulation features will be discussed in later paragraphs.

For precession, higher summer insolation results in higher surface air temperatures (Figure 4.3), except for monsoonal North-Africa / westernmost Arabic Peninsula and northwest India / Pakistan. Strong increases in cloud cover over these areas (not shown) decrease the amount of solar radiation reaching the surface. In addition, increased evaporation cools the surface. These monsoon-intensification feedbacks thus completely overcome the direct warming effect of increased insolation. The rest of the continent warms up strongly, up to 8°C over continental Asia and 10°C over the Middle East. Warming over the ocean is smaller due to its large heat capacity. Over south-east Asia, the temperature response over land (south of ∼25°N) is

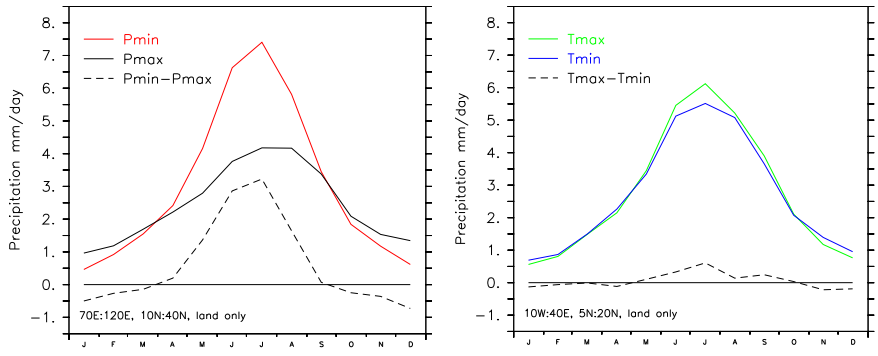

(a) Precipitation Pmin, Pmax

(b) Precipitation Tmax, Tmin

Figure 4.1: Precipitation over Asia, in mm/day, averaged over 70°E:120°E, 10°N:40°N land only for precession (a) and obliquity (b). Differences are given by the dashed lines.

damped by a small increase in cloud cover and increased evaporative cooling.

In response to increased summer temperatures over the continent, sea level pressure over these regions is reduced (Figure 4.4), mostly over continental Asia and the Middle East. Over the Tibetan Plateau, southern India, the Bay of Bengal, South-East Asia and the Chinese Seas, sea level pressure is higher during Pmin. The area of higher surface pressure over South-East Asia is connected to a strengthened North Pacific High (not shown). The pressure gradient between eastern Asia and the Pacific is therefore stronger during Pmin (Figure 4.4, top left), strengthening the southerly winds over the eastern Asia monsoon area (Figure 4.5). Over most of the northern Indian ocean winds are weaker and directed in a more westward direction during Pmin by the high pressure anomaly over South-East Asia. Monsoonal winds over the northernmost Arabian Sea and Bay of Bengal are stronger.

To investigate the source of the increased monsoon precipitation during Pmin, we first consider evaporation. Figure 4.6 shows that evaporation over land is increased in most areas. This increase, up to 3 mm/day, is small compared to the precipitation increase, which reaches 15 mm/day (Figure 4.2). Local recycling therefore plays a small role: (ΔP - ΔE)/ΔP is 78% for 70°E:120°E, 10°N:40°N, JJA, land only, so most of the increased precipitation originates elsewhere. Precipitation is redistributed with less precipitation over the surrounding oceans and more over land during Pmin (Figure 4.2). There is no additional moisture source from ocean evaporation over the northern Indian Ocean (Figure 4.6), where evaporation is slightly reduced in relation to reduced wind speed (Figure 4.5). Just south of the equator evaporation and wind speed are higher during Pmin, so this southern hemisphere region is a source of enhanced monsoonal precipitation over the northern hemisphere Asian continent. The surface latent heat flux over this SH region is enhanced (following the same patterns as evaporation, Figure 4.6).

Despite the lack of increased evaporation, moisture transport from the Arabian

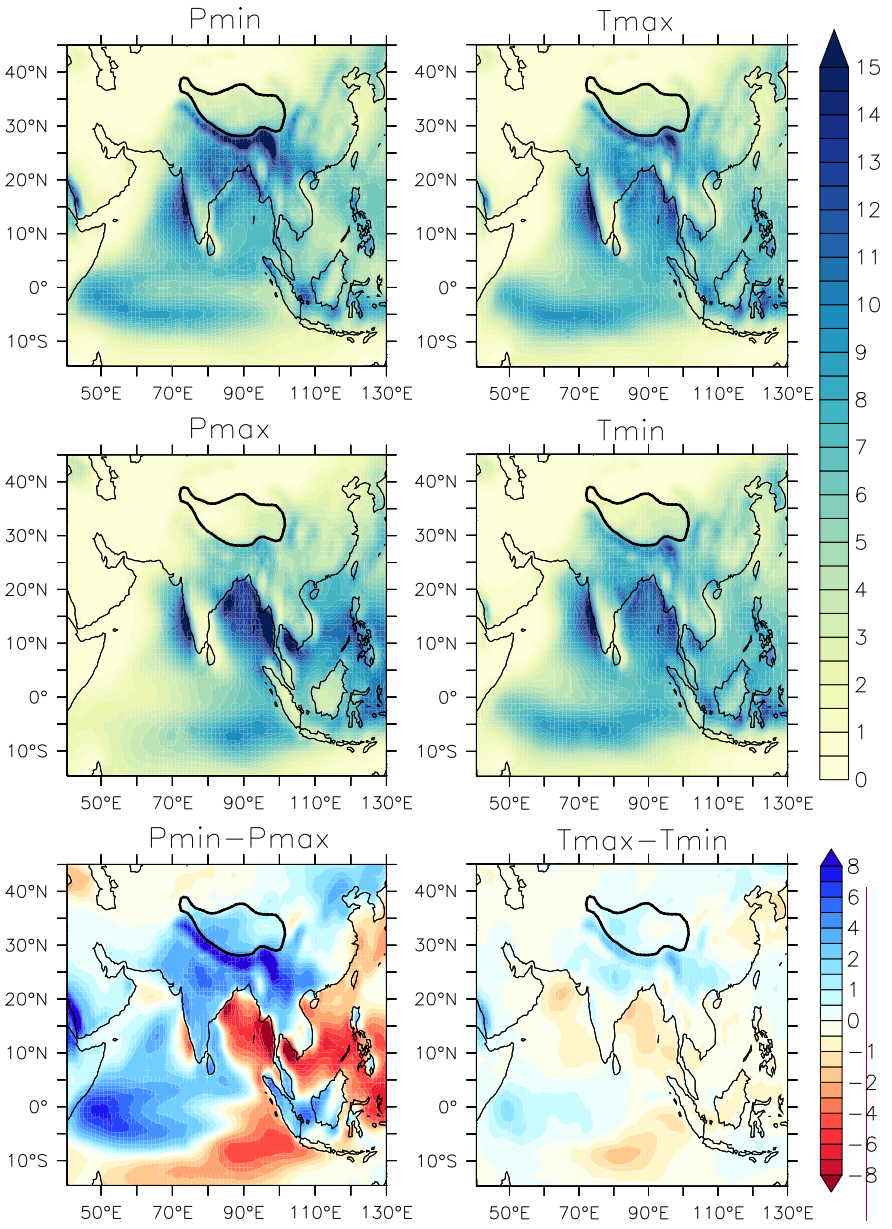

Figure 4.2: June-July-August average precipitation in mm/day during Pmin (top left), Pmax (middle left), Tmax (top right) and Tmin (middle right). Differences are given in the lower left panel for precession and the lower right panel for obliquity. The 4000m contour line is given to indicate the Tibetan plateau.

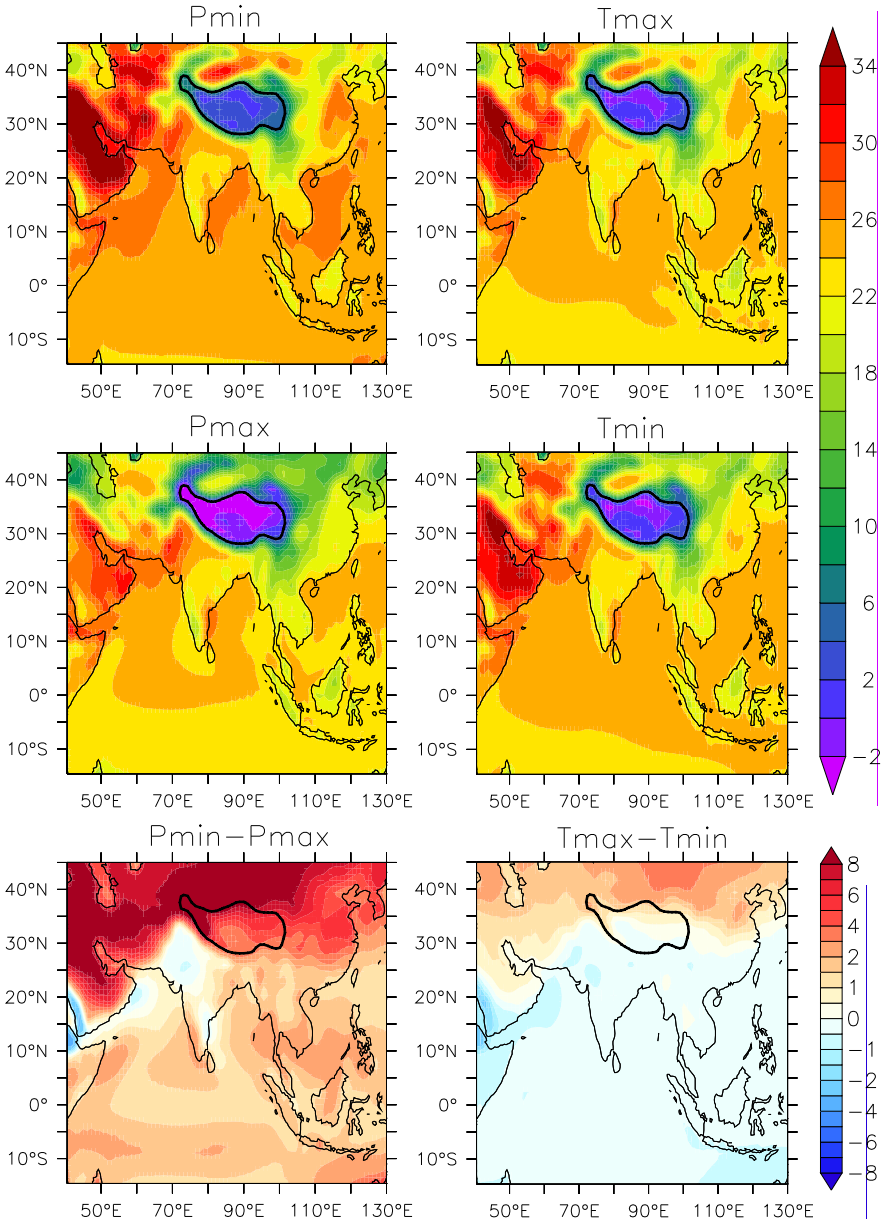

Figure 4.3: June-July-August average surface air temperature in °C during Pmin (top left), Pmax (middle left), Tmax (top right) and Tmin (middle right). Differences are given in the lower left panel for precession and the lower right panel for obliquity. The 4000m contour line is given to indicate the Tibetan plateau.

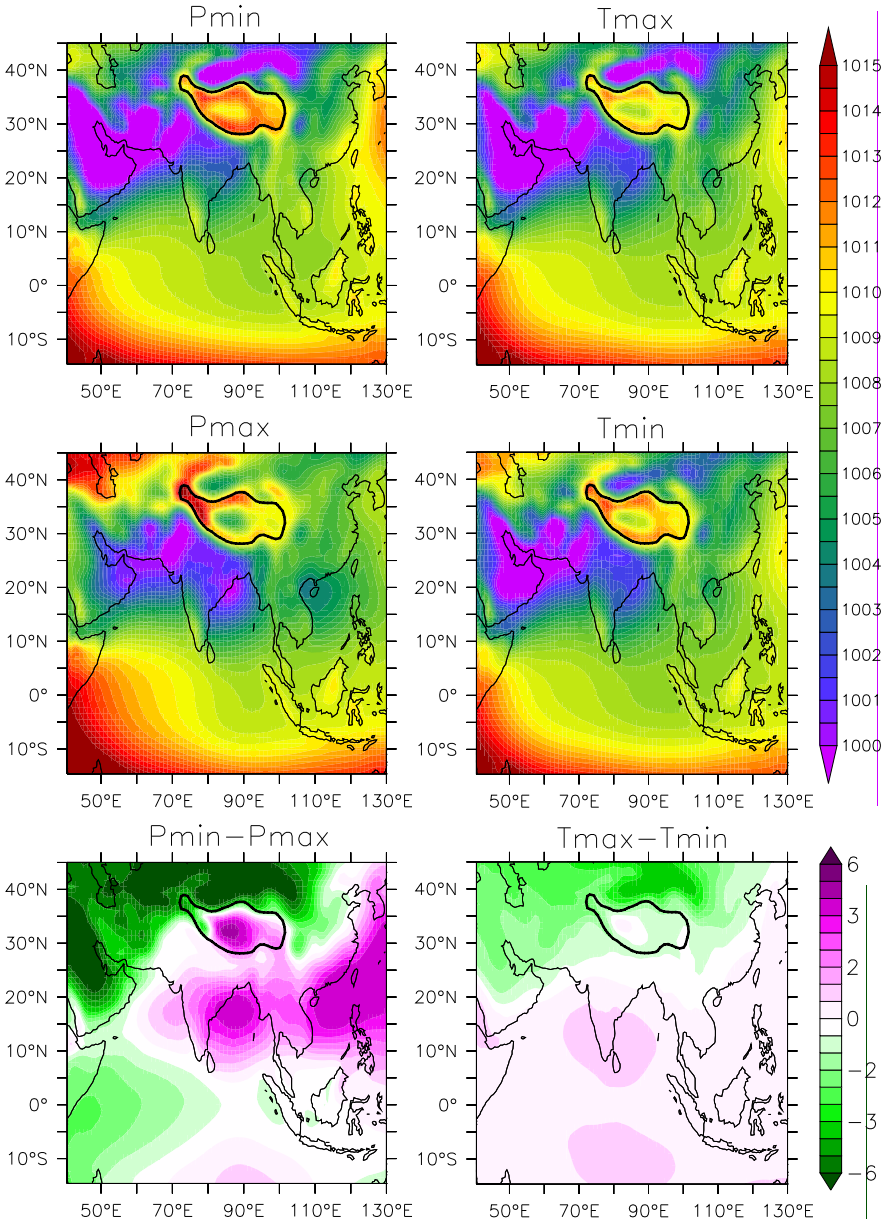

Figure 4.4: June-July-August average sea level pressure in hPa during Pmin (top left), Pmax (middle left), Tmax (top right) and Tmin (middle right). Differences are given in the lower left panel for precession and the lower right panel for obliquity. The 4000m contour line is given to indicate the Tibetan plateau.

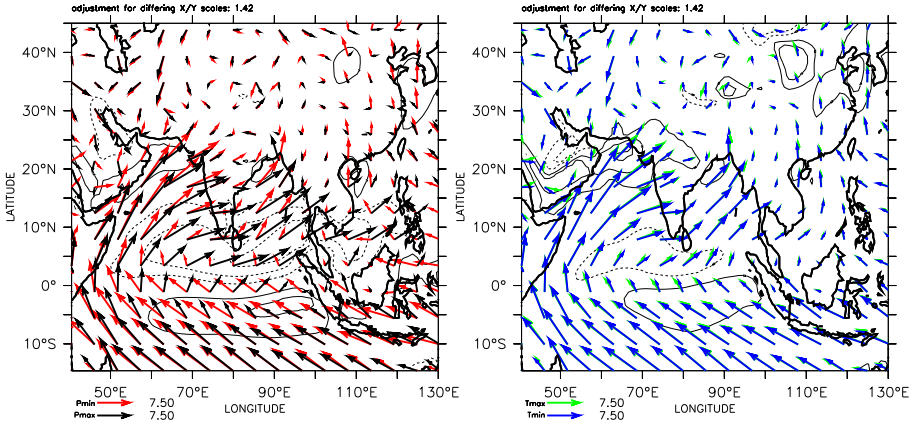

Figure 4.5: June-July-August average surface wind in m/s during Pmin (red) and Pmax (black, left), Tmax (green) and Tmin (blue, right). Contours indicate windspeed differences. Positive (negative) values are given by solid (dashed) lines. For precession the contour inverval is 2 m/s (left), for obliquity 0.5 m/s (right).

Sea onto the continent is increased (Figure 4.7). This is mostly related to an increased specific humidity over this area (not shown) due to increased temperatures; wind speed over this area is slightly reduced (Figure 4.5). Northward moisture transport over East Asia is increased in association with both stronger winds and higher specific humidity. Over the southern tropical Indian Ocean moisture transport is stronger and more westward, in line with the surface winds (Figures 4.7, 4.5). Moisture transport is strengthened as well over the areas north of $\sim$10-15°N. Changes over the continental interior are small, moisture transport from continental regions are minor. Net precipitation, also shown in Figure 4.7 is very similar to precipitation, again indicating the small role of evaporation. Reduced evaporation over most of the northern Indian Ocean further increases net precipitation.

Changes in the upper atmosphere are consistent with the surface precipitation changes. Figure 4.8 shows stronger convection (upward motion) along the Himalayas during Pmin, as well as stronger convection over the rest of monsoonal Asia and the western Indian Ocean. Over the drier ocean regions, convection is reduced. Areas of increased (decreased) upward motion also match with areas of reduced (increased) surface pressure (Figure 4.4).

The increased precipitation, reduced surface pressure and increased convection over the western Indian Ocean during Pmin are characteristic of a positive Indian Ocean Dipole (IOD) pattern (Saji et al., 1999). Surface winds along the equator are more westward (Figure 4.5), conceivably forced westward by the high surface pressure anomaly over south-eastern Asia (Figure 4.4). Because of the more westward winds, there is more upwelling in the east near Sumatra, and warm waters reach further west, reducing the east-west sea surface temperature gradient over the

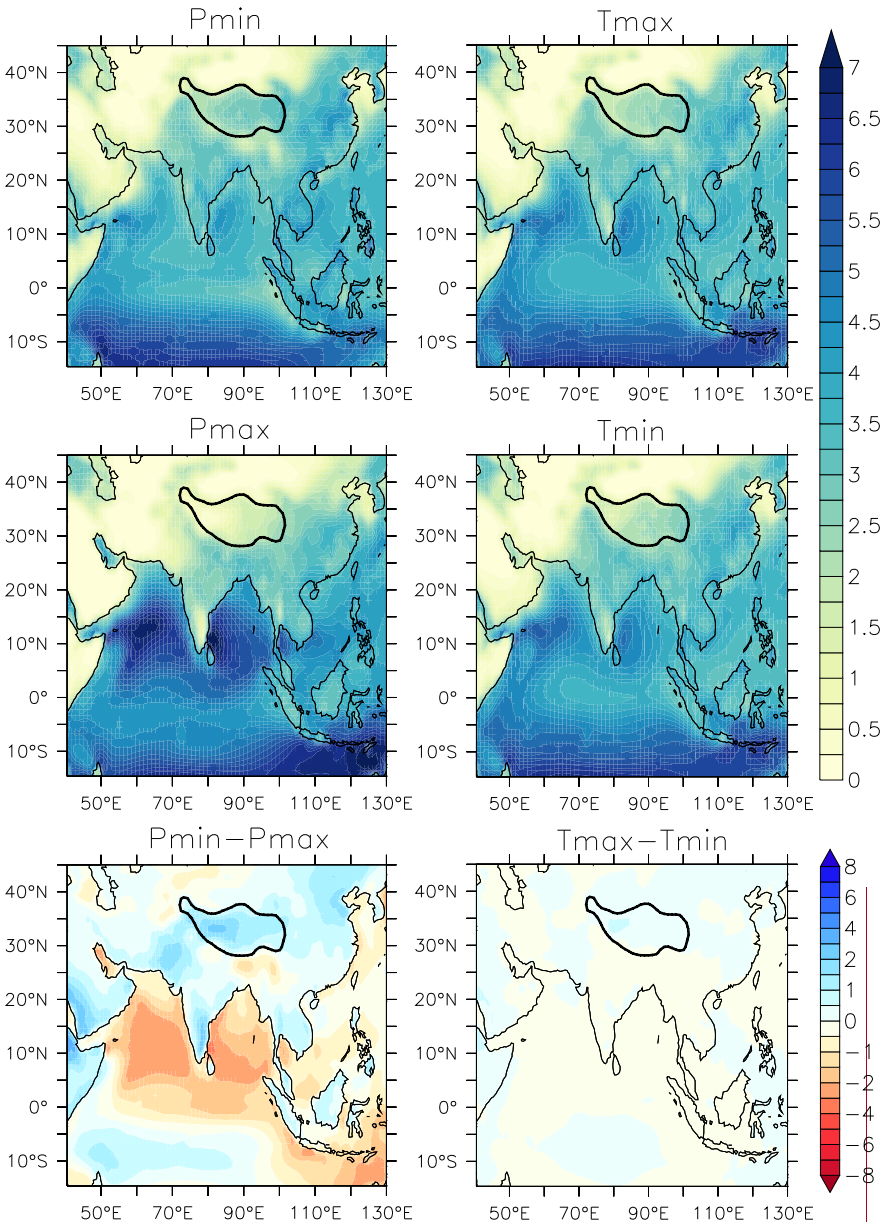

Figure 4.6: June-July-August average evaporation in mm/day during Pmin (top left), Pmax (middle left), Tmax (top right) and Tmin (middle right). Differences are given in the lower left panel for precession and the lower right panel for obliquity, where positive values (blue) indicate increased evaporation. The 4000m contour line is given to indicate the Tibetan Plateau.

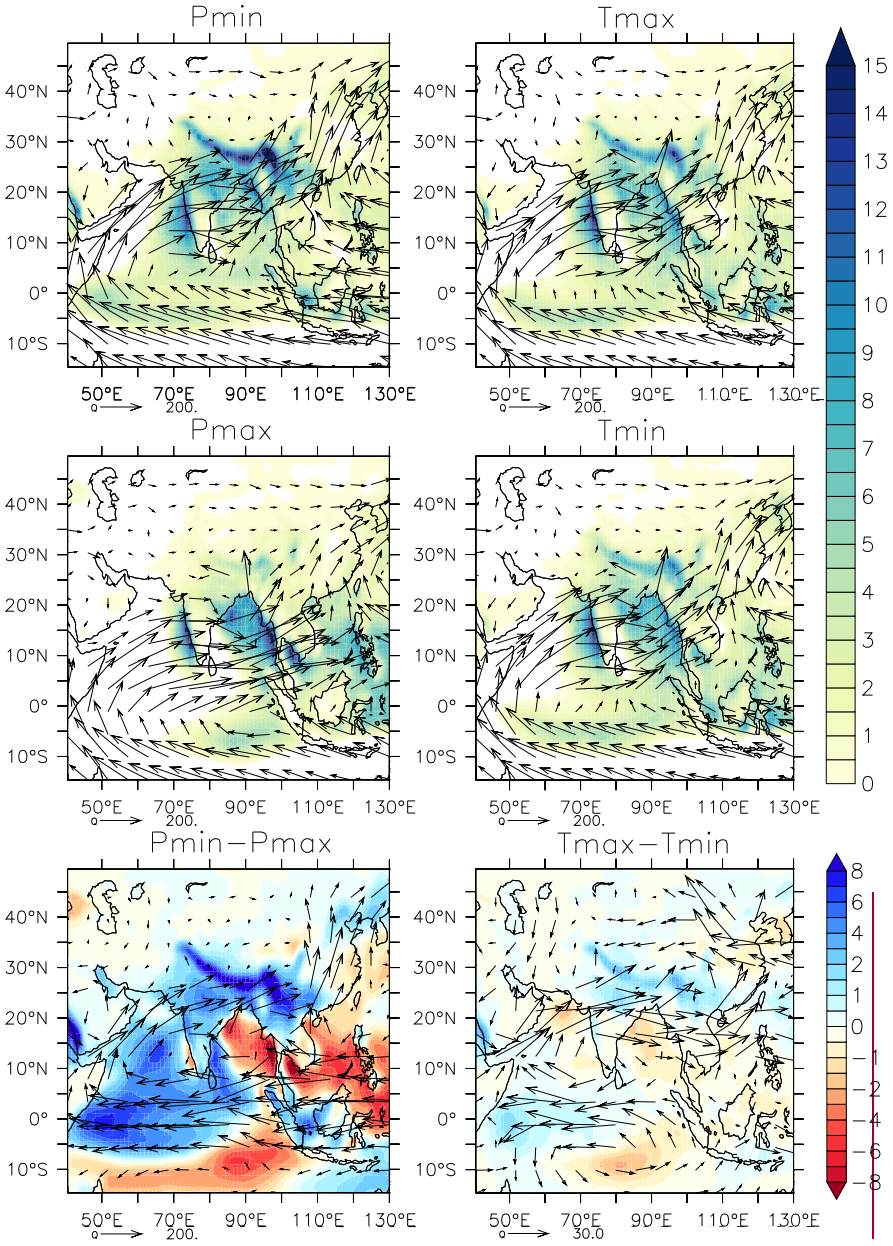

Figure 4.7: June-July-August average net precipitation in mm/day during Pmin (top left), Pmax (middle left), Tmax (top right) and Tmin (middle right). Differences are given in the lower left panel for precession and the lower right panel for obliquity, where positive values (blue) indicate increased net precipitation. The vectors indicate moisture transport **Q**, the vertical integral of q**v** in kg/(ms). Unit vector length is 200 kg/(ms), except for the lower right where it is set to 30.

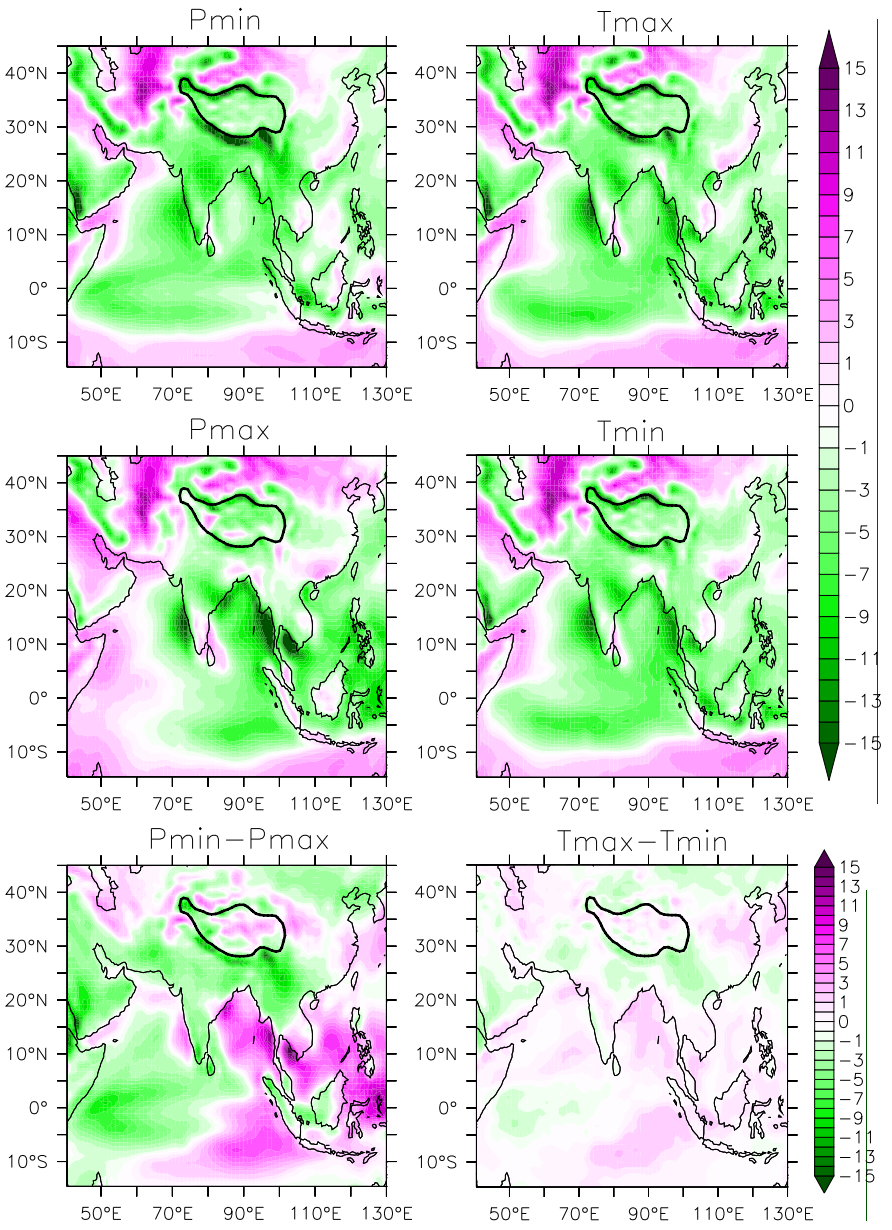

Figure 4.8: June-July-August average vertical velocity at 500 hPa in 10^{-2} Pa/s during Pmin (top left), Pmax (middle left), Tmax (top right) and Tmin (middle right). Differences are given in the lower left panel for precession and the lower right panel for obliquity. Green indicates upward motion, purple indicates downward motion. The 4000m contour line is given to indicate the Tibetan plateau.

tropical Indian Ocean (Figure 4.9). Warmer sea surface temperatures in the western Indian Ocean reduce surface pressure and support increased convection. Furthermore, cooler sea surface temperatures in the north-western Arabian Sea, at the coast of Oman, are indicative of more upwelling due to stronger north-eastward monsoon winds during Pmin.

4.3.2 Obliquity

Obliquity-induced insolation changes are smaller than the changes induced by precession, in line with the insolation forcing. The JJA averaged insolation between 10°N and 40°N is $\sim$6 Wm^{-2} higher during Tmax than Tmin. At the same time SH insolation is reduced, creating an increased interhemispheric insolation gradient.

Summer precipitation is slightly higher during Tmax over monsoonal Asia, on the order of 0.5 mm/day (Figure 4.1(b)). Precipitation patterns during Tmax and Tmin are quite similar (Figure 4.2). Like Pmin, most of the precipitation increase during Tmax occurs just south of the Tibetan Plateau and the eastern end of the Himalaya, where JJA precipitation is 3 mm/day higher. The western Indian Ocean is wetter as well during Tmax, while the Arabian Sea, Bay of Bengal and South China Sea are drier.

Summer temperatures are higher north of 25-30°N during Tmax, because of the small heat capacity of the continent and the fact that the NH insolation increase is stronger towards the higher latitudes. Over India and South-East Asia temperatures are slightly lower because of increased cloud cover, especially over Pakistan / western India (Figure 4.3). On the SH temperatures are lower due to decreased JJA insolation during Tmax.

Changes in surface pressure roughly follow the temperature changes; surface pressure is lower over the continent north of $\sim$25°N and higher south of $\sim$25°N (Figure 4.4). As during Pmin, the North Pacific High is stronger during Tmax (not shown). Over southern India / the northern Indian Ocean pressure is also slightly increased, forcing the southerly monsoon winds in a more westward direction during Tmax at $\sim$0-10°N (Figure 4.5). Wind speed over this area is slightly lower. Over the coastal areas in the northern Arabian Sea, Bay of Bengal and over the East Asian Coast the pressure gradient is slightly increased, in agreement with stronger landward monsoon winds over these areas.

The stronger monsoon winds over the coasts bring more moisture into the continent; moisture transport over these regions is increased (Figure 4.7). Over the western tropical Indian Ocean moisture transport is slightly reduced, due to both weaker winds and reduced specific humidity (not shown). The latter is related to reduced JJA insolation and lower temperatures over the tropics and the SH during Tmax. Furthermore, there is very little obliquity-induced change in evaporation over both land and sea (Figure 4.6). Therefore the increased monsoonal precipitation during Tmax is not related to increased local recycling over land nor to enhanced ocean evaporation. (ΔP - ΔE)/ΔP for 70°E:120°E, 10°N:40°N, JJA, land only is 98%, so the monsoon precipitation increase results from a redistribution of precipitation

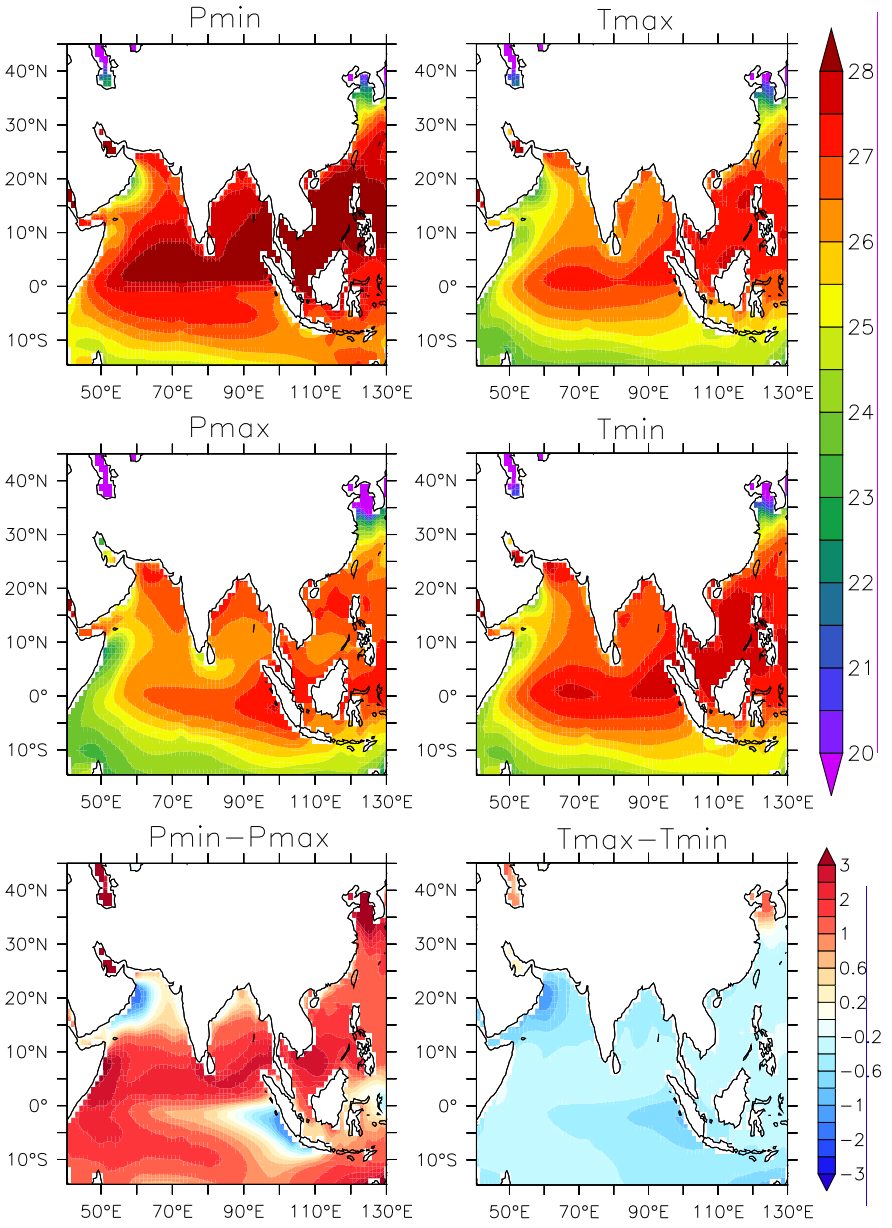

Figure 4.9: June-July-August average sea surface temperature in °C during Pmin (top left), Pmax (middle left), Tmax (top right) and Tmin (middle right). Differences are given in the lower left panel for precession and the lower right panel for obliquity.

from the surrounding oceans onto the monsoonal land areas. A small increase in evaporation and moisture transport occurs over the southern tropical Indian Ocean (Figures 4.6, 4.7).

The vertical velocity at 500 hPa (Figure 4.8) further shows the redistribution of precipitation: upward velocities (convection) is reduced over the oceans and increased over land, mostly over the regions with the strongest precipitation increase (Figure 4.2). The exception is the western tropical Indian Ocean, where during Tmax convection is slightly stronger and precipitation is higher. This IOD-like pattern is similar to the Pmin-Pmax anomalies described in Section 4.3.1, with more westward winds along the equator and a reduced east-west sea surface temperature gradient. Sea surface temperatures are overall lower during Tmax due to reduced JJA insolation over the tropics and SH. A colder sea surface is also a reason for the lack of decreased surface pressure over the western Indian Ocean (Figure 4.4). Nonetheless the cooling effect of increased upwelling during Tmax can be seen in the east, near Sumatra, as well as over the north-western Arabian Sea, near the coast of Oman where winds are stronger (Figure 4.9, 4.5).

4.4 Discussion

We have shown, using EC-Earth, that monsoon precipitation is enhanced over Asia when summer insolation on the Northern Hemisphere (NH) is increased, during minimum precession and maximum obliquity (Pmin and Tmax). This is the first study to investigate the separate effects of precession and obliquity at high resolution. Here we discuss how our results compare to previous model studies, how the responses to precession and obliquity differ, how our results compare to those for the North-African monsoon (Chapter 3) , and how our results compare to proxy climate studies of the Asian monsoons.

4.4.1 Previous model studies

Overall, the strengthening of the Asian monsoons at times of precession-induced increased NH summer insolation is recognized in many paleoclimate modelling studies. Nearly all paleoclimate models run at lower resolution than EC-Earth. Often used for orbital forcing studies is the Mid-Holocene, a selected timeslice of the Paleo Modelling Intercomparison Project (PMIP), when perihelion occurred in autumn and the insolation difference compared to present-day is similar to but of smaller amplitude than the Pmin-Pmax difference used here. In a Mid-Holocene study performed with the same model we therefore found similar but smaller changes compared to the precession-induced changes reported in this present study (Chapter 2, Bosmans et al. 2012). These changes are consistent with other PMIP studies which overall report enhanced southerly monsoon winds over East Asia related to an enhanced land-sea thermal contrast and increased pressure over the Pacific as well as increased convection over land (Jiang et al., 2013; Tian and Jiang, 2013; Wang and

Wang, 2013; Zheng et al., 2013). The increased SLP along south-east Asia and the IOD-like increased precipitation over the western Indian Ocean are reported for the Mid-Holocene as well (Jiang et al., 2013; Wang et al., 2012; Zhao et al., 2005). There is however some model spread (Wang and Wang, 2013; Zhao et al., 2005).

The few studies that also focus on idealized extreme precession forcing report enhanced monsoon precipitation over India and East Asia (Erb et al., 2013; Mantsis et al., 2013), but do not discuss the Asian monsoon in detail. Furthermore, Mantsis et al. (2013) reports an enhanced North Pacific High, partly forced by strengthened monsoons. The surface pressure anomalies in their study are very similar to those found here (Figure 4.4), with the North Pacific High shifted slightly north-westward, during minimum precession, connected to positive SLP anomalies over south-east Asia. Their precipitation anomalies over the tropical Indian Ocean also show an Indian Ocean Dipole (IOD) pattern (Figure 4.2).

In idealized experiments of high (maximum) and low (minimum) obliquity, Erb et al. (2013) find weakened NH monsoons over northern Africa, India, and parts of China during low obliquity. Chen et al. (2011) also investigate the effect of obliquity on the Asian monsoons, reporting increased summer precipitation over India and south-east Asia during high obliquity. They further suggest a dipole pattern over eastern Asia, with decreased north-east Asian precipitation during high obliquity. Although we see a small area of precipitation decrease over north-east Asia during Tmax as well, this "dipole" is not as strong as in Chen et al. (2011). Furthermore, they do not observe enhanced precipitation over the western Indian Ocean and show a different surface pressure and wind anomaly pattern compared to our obliquity results. These differences may be due to model and / or resolution differences; their study uses a coarse resolution of $\sim 7.5^{\circ}$x4° compared to 1.125°x1.125° used here. The obliquity experiments of Tuenter et al. (2003) do not show an IOD-like pattern either, which may be related to model shortcomings (Chapter 3, Bosmans et al. 2014).

Although our model results are in line with other model experiments for precession-induced monsoon changes, the addition of components that are lacking from our model may result in slightly different responses. EC-Earth-2-2 does not include a dynamic vegetation module. Changing vegetation patterns can have a small effect on the monsoonal response to orbital forcing (e.g. Dallmeyer et al., 2010; Tian and Jiang, 2013). Furthermore, EC-Earth-2-2 lacks dynamic ice sheets. Hence changes in ice volume or area do not play a role in the monsoonal response discussed here, and our findings imply that the ISM and EASM can respond directly to (sub-) tropical insolation changes. A more detailed discussion on how obliquity influences low-latitude climate without a high-latitude influence can be found in Chapter 5.

4.4.2 Precession vs. obliquity

The precession-induced changes in insolation are different from those induced by obliquity (Chapter 3, Bosmans et al. 2014; Tuenter et al. 2003). During northern hemisphere summer (JJA), insolation is increased on the northern hemisphere

during both Pmin and Tmax, while at the same time on the southern hemisphere insolation is also increased during Pmin but decreased during Tmax. At first glance the Asian monsoon changes seem very similar, albeit weaker for obliquity. For both a strengthening of the North Pacific High occurs, creating an increased land/sea pressure gradient over East Asia, resulting in stronger northward monsoon winds. There is increased surface pressure over south-eastern Asia, decreased windspeeds over the northern Indian Ocean and increased precipitation over the tropical western Indian Ocean for both precession and obliquity. Changes in sea surface temperature, however, are different due to the JJA southern hemisphere increase in insolation during Pmin and decrease during Tmax. This results in overall warmer sea surface temperatures during Pmin and colder temperatures during Tmax, the latter being the likely cause of the lack of lower surface pressure over the western tropical Indian Ocean during Tmax. Also, lower temperatures result in lower specific humidity and lower moisture transport over the the western Indian Ocean, which were increased for Pmin related to higher JJA insolation and temperatures.

4.4.3 Orbital forcing of the North-African and Asian monsoons

Both the North-African and the Asian monsoons are strengthened during Pmin and Tmax, with the largest changes occuring over North-Africa (Chapter 3). For precession this is contrary to Braconnot et al. (2008), who state that increased insolation in the northern hemisphere in phase with the summer solstice has a larger impact on the Indian monsoon than on the African monsoon, because the Indian monsoon peaks near summer solstice while the African monsoon peaks later. Here, we identified three reasons for a weakened response of the Indian summer monsoon. Firstly, the smaller changes over Asia are related to the increased surface pressure over south-eastern Asia and the Indian Ocean Dipole pattern. Lower wind speeds over the northern Indian Ocean reduce evaporation and the IOD pattern involves increased precipitation over the western Indian Ocean, resulting in a weakened increase in landward moisture transport. For both the North-African and Asian monsoons, however, enhanced evaporation and moisture transport from the southern hemisphere occurs. Secondly, the large precipitation differences between Pmin and Pmax over North-Africa compared to Asia may be related to the more southern location of the North-African monsoon region. Between the equator and the tropic of Cancer, insolation and precipitation peak in summer during Pmin, while during Pmax they peak in spring and autumn. Therefore the summer precipitation difference between Pmin and Pmax over North-Africa is very large (Chapter 3, Bosmans et al. 2014). The Asian monsoon regions are located both south and north of the tropic, and precipitation over the monsoonal continent shows a single peak in summer during both Pmin and Pmax (Figure 4.1). Thirdly, a northward shift of precipitation and convection is seen over the southern Indian Ocean (Figures 4.2, 4.8), but not over the northern continental regions where the Himalayas prevent the area of monsoon precipitation to extend further north. For North-Africa, especially for precession, there is not only an increase in the amount of monsoonal precipitation but also a larger

area under monsoonal influence.

4.4.4 Proxy climate record studies

Our EC-Earth experiments show that the ISM and EASM can respond instantaneously (on orbital time scales) to insolation forcing. In contrast, proxy climate record studies suggest pronounced lags with respect to the orbital forcing, ranging from ∼2.7 kyr for the EASM (e.g. Wang et al., 2008) to ∼7-9 kyr for the ISM in the precession band and from 0 to 6kyr in the obliquity band (e.g. Caley et al., 2011; Clemens and Prell, 2003). These lags are often based on productivity proxies under the assumption that productivity is related to monsoon wind strength and upwelling, so our results suggest that productivity may be related to other processes (Ziegler et al., 2010a). Furthermore, we find that not only upwelling over the western Arabian Sea but also evaporation and latent heat release from the southern tropical Indian Ocean respond instantaneously to increased northern hemisphere insolation. Therefore we do not agree with the pronounced lag and mechanisms of the ISM in the precession band suggested by e.g. Caley et al. (2011); Clemens and Prell (2003), who claim that latent heat export from the southern hemisphere into the ISM region is maximized during Pmax, when SH summer insolation is high. The debate on the monsoonal lag to orbital forcing is ongoing, with our study as well as transient model simulations suggesting an in-phase response (e.g. Kutzbach et al., 2008; Tuenter et al., 2005) and a range of lags being found in paleoclimate proxies (e.g. Clemens and Prell, 2003; Ziegler et al., 2010a,b). Additional time slice or transient experiments, including ice sheets which result in a different and / or lagged response (Weber and Tuenter, 2011), could shed more light on this discussion.

4.5 Conclusion

To conclude, using the fully coupled high-resolution model EC-Earth we demonstrate the effect of both precession and obliquity on the Asian summer monsoons, with increased monsoon precipitation and convection over the continent during minimum precession and maximum obliquity. Over East Asia the southerly monsoon flow and moisture transport is strengthened by an intensified North Pacific High and the subsequent increase in the land/sea pressure gradient. Over the Indian monsoon region changes are more complex. Increased surface pressure over south-east Asia weakens the monsoon winds over most of the northern Indian Ocean, reducing evaporation. Over the tropical Indian Ocean an Indian Ocean Dipole pattern emerges with enhanced precipitation over the western Ocean. Therefore these effects damp the enhanced landward moisture transport and monsoonal precipitation over the continent. The influence of obliquity is smaller than that of precession, and shows a different response in temperature and humidity over the Indian Ocean due to reduced insolation over the southern hemisphere. However, for both precession and obliquity wind speed and evaporation is increased over the southern Indian

Ocean. Wind speed, and therefore also upwelling, is increased as well near the coast of Oman. Our results therefore show a direct response to precession and obliquity forcing, in contrast to proxy climate records.

5

Obliquity forcing of low-latitude climate

Abstract

The influence of obliquity, the tilt of the Earths rotational axis, on incoming solar radiation at low latitudes is small, yet many tropical and subtropical paleoclimate records reveal a clear obliquity signal. Several mechanisms have been proposed to explain this signal, such as the remote influence of high-latitude glacials, the remote effect of insolation changes at mid- to high latitudes independent of glacial cyclicity, shifts in the latitudinal extent of the tropics, and changes in latitudinal insolation gradients. Using a sophisticated coupled ocean-atmosphere global climate model, EC-Earth, without dynamical ice sheets, we performed two experiments of obliquity extremes. Our results show that obliquity-induced changes in tropical climate can occur without high-latitude ice sheet fluctuations. Furthermore, the tropical circulation changes are consistent with obliquity-induced changes in the cross-equatorial insolation gradient, implying that this gradient may be used to explain obliquity signals in low-latitude paleoclimate records instead of the classic 65°N summer insolation curve.

5.1 Introduction

The influence of obliquity (axial tilt) on low-latitude insolation is very small and negligible compared to the influence of the precession of the equinoxes and the solstices (Bosmans et al., 2014; Tuenter et al., 2003) (Figures 3.1, 5.6). Many studies have therefore attributed the relatively strong obliquity signal in low-latitude paleoclimate records to high-latitude mechanisms. For instance, dust flux records from both the Atlantic and Arabian Sea concur with obliquity-paced global climate cycles, suggesting a close link between changes in low-latitude aridity and glacial variability (Bloemendal and deMenocal, 1989; deMenocal, 1995; deMenocal et al., 1993; Tiedemann et al., 1994). Several other proxy studies, however, find

low-latitude obliquity signals at times when glacial cycles were much smaller or even absent (Hilgen et al., 1995, 2000; Lourens et al., 1996, 2001; Sierro et al., 2000). In particular, obliquity-controlled interference patterns in Mediterranean sapropels are not only present in the Pleistocene (Lourens et al., 1996), but also in the warmer Pliocene and Miocene (Hilgen et al., 1995). Sapropels are generally related to African monsoon strength (Rossignol-Strick, 1985), which would indicate that monsoon intensity is affected by obliquity both before and after major Northern Hemisphere (NH) glacial cycles determined global climate. Furthermore, in the late Pliocene and Pleistocene, phase relations suggest that the obliquity influence on sapropel formation and North-African aridity did not proceed indirectly via ice driven responses but more directly via summer insolation (Lourens et al., 2010, 1996). In addition, color changes associated with carbonate dilution cycles in north-western Africa and Spain reveal precession-obliquity interference patterns similar to those found in Mediterranean sapropels (Hilgen et al., 2000; Sierro et al., 2000). Also, others have ruled out global ice volume as a primary forcing mechanism for the occurrence of obliquity-related variability in Indian monsoon strength as inferred from sediment records of the Arabian Sea (Clemens et al., 1991; Clemens and Prell, 2003).

Hence the North-African and Indian monsoons may respond to obliquity independent of high-latitude ice growth and decay. The driving mechanism of obliquity-induced climate change over the tropics is yet poorly understood, since the influence of obliquity on low-latitude insolation is small. Some studies have suggested that the obliquity signal in the tropics is related to a local forcing mechanism. Rossignol-Strick (1985) introduced a monsoon index based on the summer insolation difference between the tropic of Cancer and the equator, recognising that the North-African monsoon depends on the strength of the Saharan heat trough as well as on the pressure gradient between the heat trough and the equator. The summer insolation difference between these two latitudes introduces an obliquity signal, though too small to explain the characteristic obliquity interference patterns in the Mediterranean sapropels. Lourens and Reichart (1996) therefore introduced the Summer Inter Tropical Insolation Gradient (SITIG), $I_{23^\circ N}$-$I_{23^\circ S}$ at June 21^{st}, which shows a better fit to the sapropel record. At times of high obliquity, SITIG is stronger than during low obliquity. This also holds for SITIG in austral summer ($I_{23^\circ S}$-$I_{23^\circ N}$ at December 21^{st}). A strong SITIG may result in an intensified winter Hadley cell, associated with stronger cross-equatorial winds and moisture transport that dominate the boreal and austral summer tropical climate (Lourens and Reichart, 1996). SITIG can therefore explain the obliquity signal in the tropics without high-latitude mechanisms. The effect of SITIG and other insolation gradients on high-latitude climate and glacial cycles has been discussed in several studies (Antico et al., 2010; Leuschner and Sirocko, 2003; Lourens and Reichart, 1996; Mantsis, 2011; Raymo and Nisancioglu, 2003) (see Discussion).

Modelling results suggested that the influence of obliquity on the tropics resulted from high latitude forcing. According to Tuenter et al. (2003), an increase in obliquity results in higher temperature and humidity at high latitudes. The res-

ulting strengthening of southward moisture transport as well as a stronger Asian low pressure system act to strengthen the monsoons. This remote control (north of 30°N) accounts for 80-90% of the total obliquity signal in the North-African monsoon, without any changes in land ice (Tuenter et al., 2003). The model they used is EC-Bilt (Opsteegh et al., 1998), a quasi-geostrophic climate model of intermediate complexity, which is not very suitable for modelling tropical climate adequately.

In this study we use a state-of-the-art high resolution fully coupled ocean-atmosphere model, EC-Earth, to investigate influence of obliquity signal on the tropics (without land ice changes). The model and experimental set-up are described in Section 6.2, followed by results in Section 5.3, a discussion in Section 6.4 and a conclusion in Section 6.5.

5.2 Model and Experiment set-up

Here we use the new, state-of-the-art high resolution fully coupled ocean-atmosphere model, EC-Earth (Bosmans et al. (2012); Hazeleger et al. (2011), also used for the Fifth Assessment Report of the Intergovernmental Panel on Climate Change), to investigate influence of obliquity signal on the tropics. Following Tuenter et al. (2003), we performed two experiments, one with a low obliquity (22.04°, Tmin) and one with a high obliquity (24.45°, Tmax). Eccentricity is set to zero, so the Earths orbit is perfectly round and there is no precession (see Table 1.1). All other boundary conditions are fixed at pre-industrial levels, therefore there are no changes in land ice or in vegetation. For more details see Section 3.2.

5.3 Results

EC-Earth shows considerable differences in net precipitation over the tropics between high (Tmax) and low obliquity (Tmin, Figure 5.1). There is an overall intensification of the North-African and Asian monsoons during boreal summer (June-July-August), with a redistribution of precipitation from ocean to land and stronger landward monsoon winds (Figure 5.1(a)). Over the equatorial and southern Pacific wind speed changes are small while winds around the North Pacific as well as the North Atlantic Highs are generally stronger. During austral summer (December-January-February) the precipitation and wind changes are smaller than during boreal summer, likely related to the smaller land mass and therefore weaker monsoons on the Southern Hemisphere (SH). Precipitation increase occurs primarily on the SH during Tmax, with slightly stronger SH austral summer monsoons, while precipitation over the NH tropics is reduced (Figure 5.1(b)).

Our experiments indicate strengthened surface winds towards the summer hemisphere during Tmax (Figures 5.1(a) and 5.1(b)). The zonal mean cross-equatorial surface winds are northward and they are indeed stronger during boreal summer, extending slightly further into the NH (Figure 5.2(a)). With these stronger surface

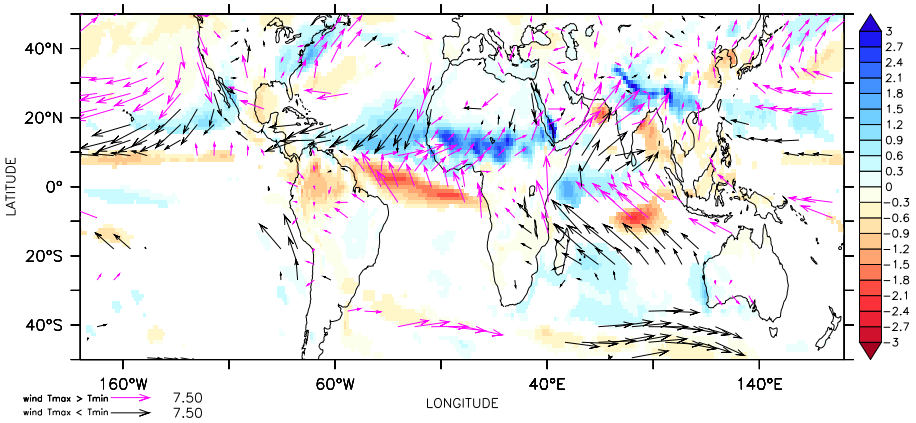

(a) June-July-August

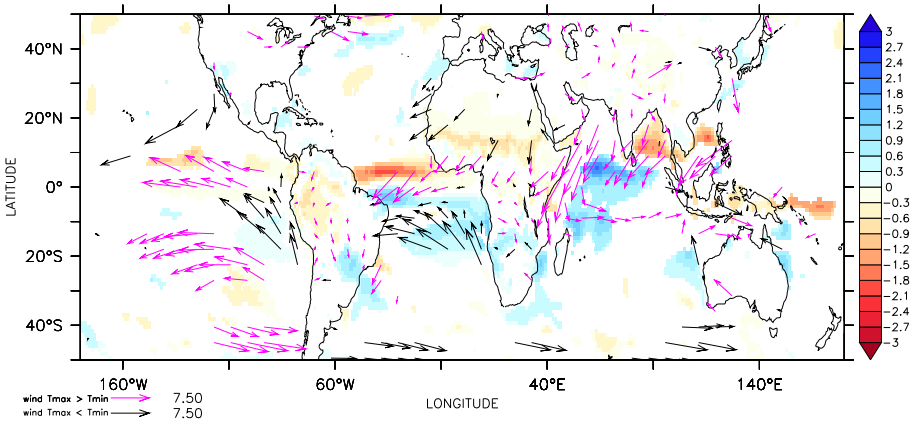

(b) December-January-February

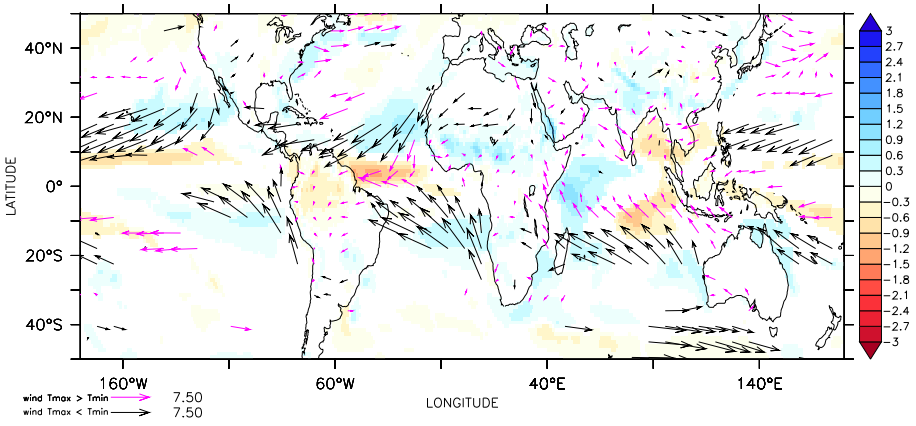

(c) Annual mean

Figure 5.1: (Caption on the following page)

winds the moisture transport into the NH is strengthened as well during Tmax (Figure 5.2(b)). Moisture transport into the North-African and Asian monsoon areas is generally higher during boreal summer, with enhanced northward cross-equatorial transport mostly over the Indian Ocean (see Figure 5.4(a)). Changes over the Pacific are small, which could be related to the absence of land masses which have a stronger response to insolation changes.

During austral summer the zonal mean southward cross-equatorial surface winds are stronger in Tmax, extending slightly further into the SH (Figure 5.2(c)). Therefore more moisture is transported southward across the tropics (Figure 5.2(d)). Most of this increased southward moisture transport occurs over the Indian Ocean (Figure 5.4(b)), where both wind and specific humidity are increased. Over the tropical Atlantic specific humidity is lower during Tmax, so moisture transport is not increased despite the increase in wind speed (Figure 5.1(b)).

The changes in surface winds and moisture transport can be related to changes in the (winter) Hadley cell. During boreal summer, the descending branch, centered at $\sim$20°S, is strengthened, mostly at the northern side, with a slight weakening at the southern side during Tmax (Figure 5.5(a)). The same holds for the ascending branch, centered at $\sim$10°N, so the winter Hadley cell is slightly stronger and extends further into the NH during boreal summer. During austral summer, the winter Hadley cell extends from a descending branch at $\sim$20°N to an ascending branch at $\sim$10°S (Figure 5.5(b)). The additional rising branch at 5-10°N is most likely overestimated in the model due to a double-ITCZ over the Pacific, a feature that many models encounter (Lin, 2007). However, a strengthening of the winter Hadley cell can still be seen: both the descending and ascending branches are slightly stronger and extend further south during Tmax, in line with stronger southward surface winds.

While winds and moisture transport in the tropics are generally stronger during boreal and austral summer, they are weaker in the annual mean for Tmax (Figures 5.1(c), 5.2(e), 5.2(f), 5.4(c)). This weakening can be related to the obliquity-induced redistribution of insolation from low to high latitudes during Tmax, resulting in weakening of the equator-to-pole insolation gradient. Therefore annual mean meridional winds and moisture transport as well as the annual mean Hadley circulation are weaker (Figure 5.5(c)). Annual mean precipitation changes resemble mostly

Figure 5.1: (Figure on page 88) Net precipitation differences and Tmax surface wind for JJA (a), DJF (b) and annual mean (c). For net precipitation (precipitation minus evaporation), the differences (Tmax minus Tmin) are shown in mm/day. Overlain are the wind vectors for Tmax in m/s. Purple vectors indicate larger windspeeds during Tmax than during Tmin. Cross-equatorial winds are stronger in JJA (a) and DJF (b), mostly over the Atlantic and Indian Ocean. Every 7th arrow in the x-direction is drawn and every 4th arrow in the y-direction. Results are only shown where the differences in net precipitation or windspeeds are statistically significant at 95% (based on a two-sided Student t-test). The full wind field is given in Figure 5.3.

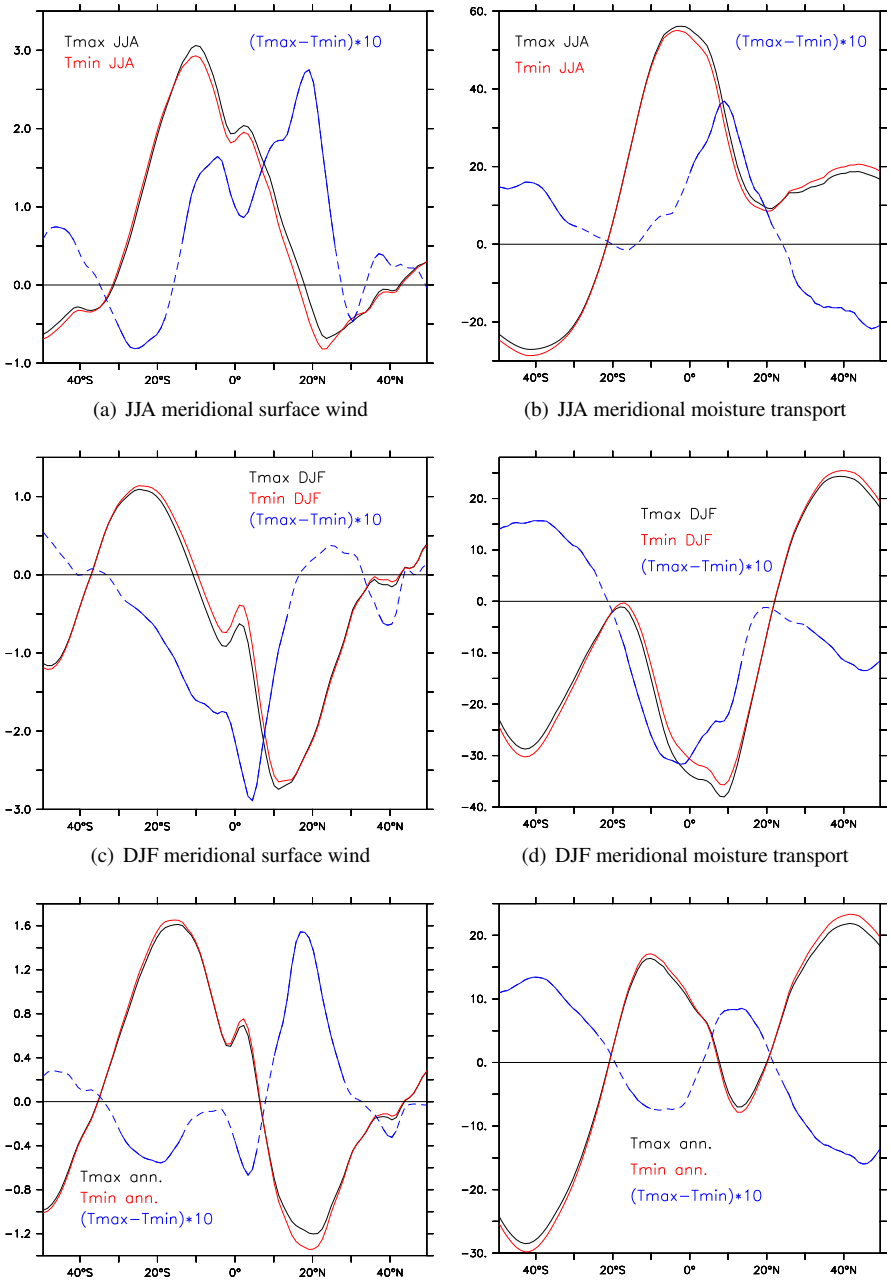

(a) JJA meridional surface wind

(b) JJA meridional moisture transport

(c) DJF meridional surface wind

(d) DJF meridional moisture transport

(e) Annual meridional surface wind

(f) Annual meridional moisture transport

Figure 5.2: (Caption on the following page)

the JJA changes over the continents, and reflect both JJA and DJF changes over the oceans (Figure 5.1(c)).

5.4 Discussion

We have shown that obliquity-induced changes in low-latitude climate arise from a direct response to changes in the cross-equatorial insolation gradient, using the sophisticated model EC-Earth. Here we discuss that these changes support the previously proposed SITIG theory (Leuschner and Sirocko, 2003; Lourens and Reichart, 1996), what the implications are for the interpretation of obliquity signals in low-latitude paleoclimate records and how obliquity-induced gradients may influence global climate.

5.4.1 Model support for the SITIG theory

The simulated changes in winter Hadley cell strength during boreal and austral summer are in accordance with the SITIG theory (Leuschner and Sirocko, 2003; Lourens and Reichart, 1996). The Summer Inter Tropical Insolation Gradient (SITIG, $I_{23^\circ N}$-$I_{23^\circ S}$ at June 21^{st}) theory states that an increased SITIG during Tmax is associated with an intensified winter Hadley cell and stronger cross-equatorial winds and moisture into the summer hemisphere. The winter Hadley cell is not entirely symmetric about the equator (as is assumed in the original SITIG hypothesisLourens and Reichart (1996)), nor are the changes in wind and moisture transport zonally invariant, likely due to differences in the land-sea distribution. Nonetheless, a stronger SITIG during Tmax results in stronger zonal mean winds and moisture transport into the summer hemisphere and a stronger Hadley cell. The Hadley cell as well as the meridional winds and moisture transport also extend further into the summer hemisphere, which is furthermore in agreement with the poleward shift of the latitude of the tropics during Tmax (Larrasoaña et al., 2003; Rossignol-Strick, 1985).

Figure 5.2: (Figure on page 90) Zonal mean meridional surface wind and moisture transport (see Methods) for JJA (a,b), DJF (c,d) and annual mean (e,f). The wind is given in m/s, moisture transport in kg/(ms) for both Tmax (black), Tmin (red) and the difference (blue, multiplied by 10 for clarity). Positive values indicate northward wind or moisture transport, negative values southward. Wind and moisture transport into the summer hemisphere is stronger during Tmax for JJA (a,b) and DJF (c,d). Solid parts of the blue line indicate where the difference is statistically significant at 95% (based on a two-sided Student t-test). Note that the vertical scales are different.

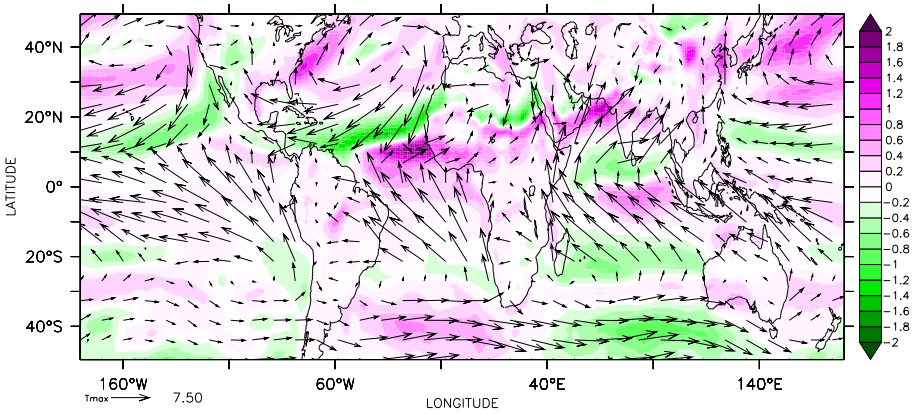

(a) June-July-August

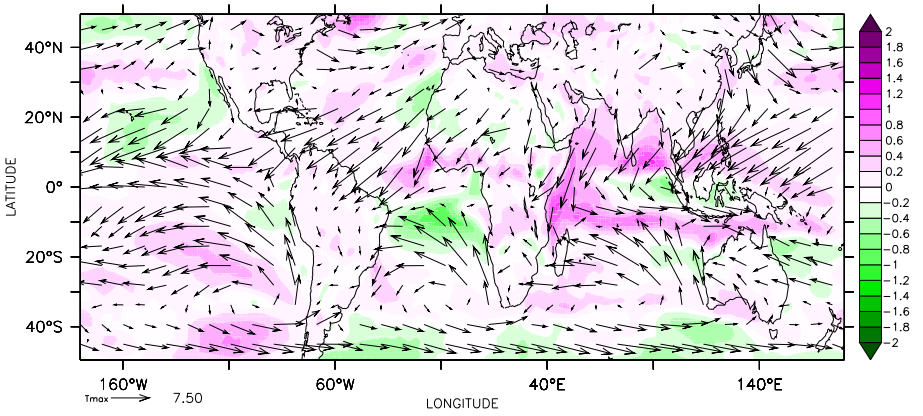

(b) December-January-February

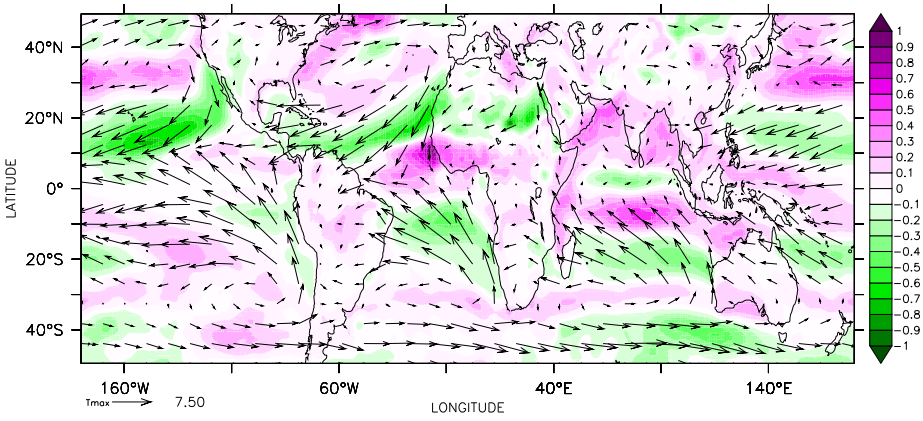

(c) Annual mean

Figure 5.3: (Caption on the following page)

5.4.2 Implications for the interpretation of paleoclimate records

Obliquity signals in low-latitude paleoclimate records are often interpreted using the 65°N 21^{st} June insolation curve based on the matching precession-obliquity interference in the records and the insolation curve. The model study of Tuenter et al. (2003) supported the use of the 65°N 21^{st} June insolation curve, indicating that ∼80-90% of the obliquity signal in the North-African monsoon is due to high latitude influences. Our results, based on a much more sophisticated (and realistic) model with fixed land ice, clearly suggest that these patterns arise from a direct response to changes in the cross-equatorial insolation gradient. Furthermore, there is a strong resemblance between (boreal) SITIG and the 65°N 21^{st} June insolation curve (Figure 5.6, Leuschner and Sirocko (2003); Lourens and Reichart (1996)). Hence, the widely applied 65°N 21^{st} June insolation curve (Hilgen et al., 1995, 2000; Lourens et al., 1996, 2001; Sierro et al., 2000; Tiedemann et al., 1994) needs to be reconsidered in favour of SITIG. SITIG instead of 65°N 21^{st} June insolation relies on a physical basis as described by our model results rather than pattern matching, and explains the obliquity influence on tropical climate independently of glacial-interglacial variability.

5.4.3 Obliquity-induced gradients and their influence on global climate

Lourens and Reichart (1996) and Leuschner and Sirocko (2003) suggested that through monsoon-induced changes in atmospheric moisture content, a strong greenhouse gas, the Summer Inter Tropical Insolation Gradient (SITIG) may drive glacial-interglacial variability. Indeed we find a significant obliquity-induced change in cross-equatorial moisture transport (Figures 2b,d). However, whether changes in atmospheric moisture content resulting from changes in low-latitude atmospheric circulation on orbital time scales can indeed result in global climate change will need to be investigated with longer model experiments including dynamic ice sheets (not included in EC-Earth).

Also, despite having a relatively strong obliquity component, the precession component in SITIG is much stronger (Figure 5.6). If, however, SITIG is equally important for changes in moisture content during both boreal and austral summer, then the precession effect will cancel out due to its opposite effect on both hemispheres. Lourens and Reichart (1996) suggest that in this case SITIG can account for the obliquity-dominated glacial variability between ∼2.7 and 1 million years ago. Given the the larger landmasses, and hence stronger monsoons, on the north-

Figure 5.3: (Figure on page 92) Wind during Tmax in JJA (a), DJF (b) and the annual mean (c), in m/s. The colour scale indicates the difference in windspeed between Tmax and Tmin, in m/s. Note the different colour scale for the annual mean. Every 9th vector is shown in the x-direction, and every 5th in the y-direction.

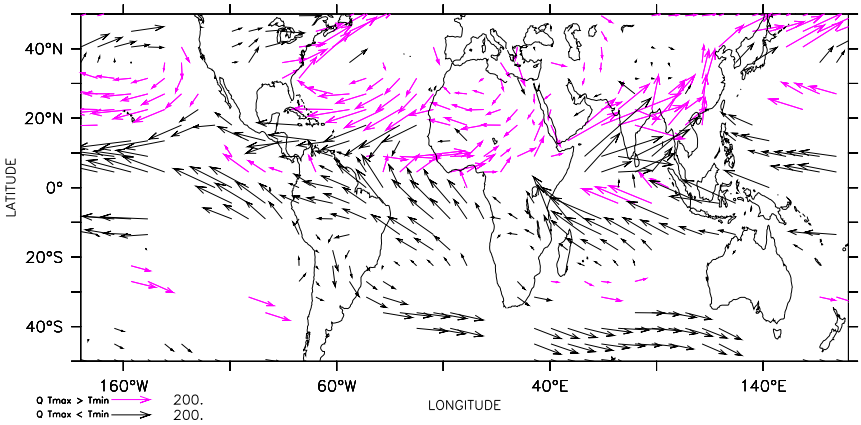

(a) June-July-August

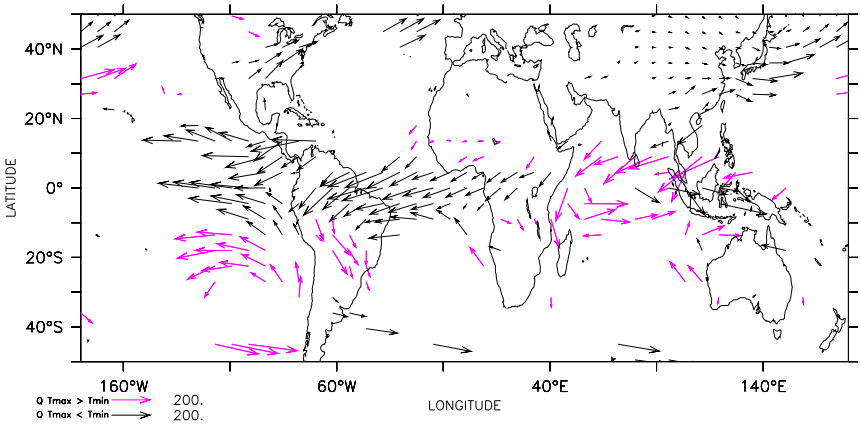

(b) December-January-February

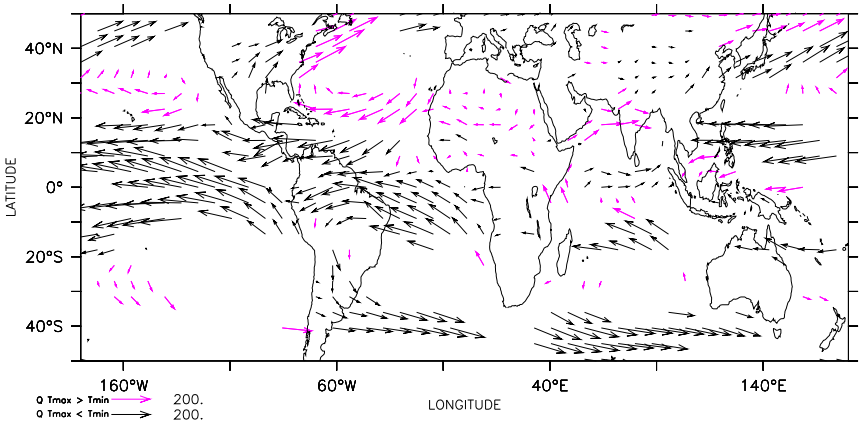

(c) Annual mean

Figure 5.4: (Caption on the following page)

ern hemisphere we do not think that the precession effect cancels out, so SITIG will not result in a pure obliquity-paced signal in moisture content.

Another mechanism by which obliquity can affect high-latitude climate and glacial cycles through latitudinal insolation gradients has been proposed by Antico et al. (2010); Mantsis (2011); Raymo and Nisancioglu (2003). These studies suggest that the poleward transport of heat, moisture and latent energy is increased during minimum obliquity due to the intensified intrahemispheric insolation and temperature gradient between high and low latitudes (Bosmans et al., 2014; Tuenter et al., 2003). The increased moisture transport towards the poles combined with low polar temperatures during low obliquity is favourable for ice growth. In our EC-Earth experiments we also find stronger poleward moisture transport outside the tropics during minimum obliquity (Tmin) during both boreal and austral summer as well as in the annual mean (not shown). Further sensitivity studies with dynamic ice sheets are necessary to determine the role of both changes in tropical circulation through interhemispheric gradients (SITIG, Leuschner and Sirocko (2003); Lourens and Reichart (1996)) and changes in poleward moisture flux through intrahemsipheric gradients in the glacial-interglacial cycles. Not only changes in ice sheets can affect the climatic response to obliquity, but ocean feedbacks may also play a role (Khodri et al., 2001). Our EC-Earth experiments are too short to discuss changes in ocean heat transport and other feedbacks.

5.5 Conclusion

The low-latitude SITIG mechanism proposed here is fundamentally different from high-latitude mechanisms previously proposed to explain the obliquity patterns at low latitudes. Our results, based on the sophisticated model EC-Earth, clearly suggest that these patterns arise from a direct response to changes in the cross-equatorial insolation gradient, i.e. without any influence of ice sheets or other high-latitude mechanisms. Hence, the widely applied 65°N 21^{st} June insolation curve needs to be reconsidered in favour of SITIG.

Figure 5.4: (Figure on page 94) Moisture transport in Tmax for JJA (a), DJF (b) and annual mean (c), vertically integrated (see Methods), in kg/(ms). Purple vectors indicate larger moisture transport during Tmax than during Tmin. Every 7th arrow in the x-direction is drawn and every 4th arrow in the y-direction. Results are only shown where the differences are statistically significant at 95% (based on a two-sided Student t-test).

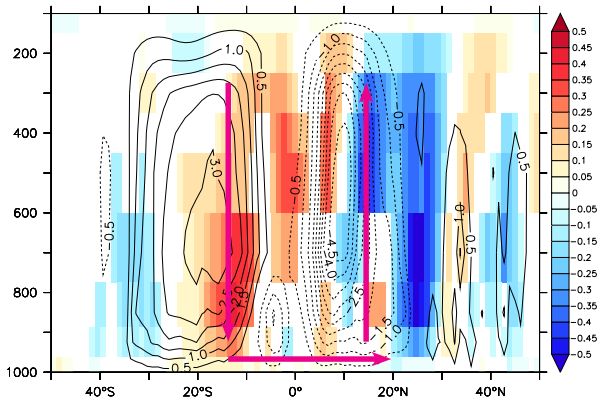

(a) JJA vertical velocity

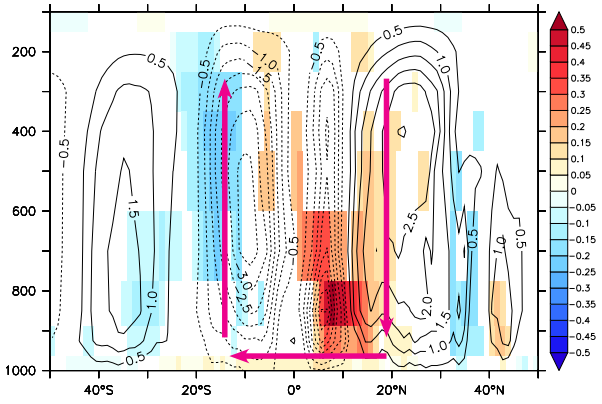

(b) DJF vertical velocity

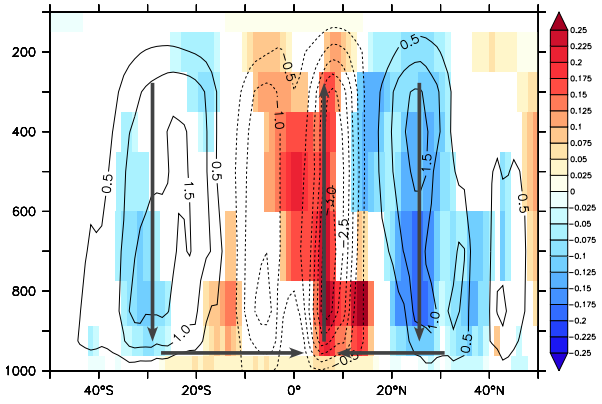

(c) Annual vertical velocity

Figure 5.5: (Caption on the following page)

Figure 5.5: (Figure on page 96) Zonal mean vertical velocity (omega, 10^{-2} Pa/s) during Tmax (contours) for JJA (a), DJF (b) and annual mean (c). Negative contours indicate upward motion (rising), positive contours indicate downward motion (sinking). The vertical scale (y-axis) denotes height in hPa. The colours indicate the differences between Tmax and Tmin, only shown where they are statistically significant at 95% (based on a two-sided Student t-test). The arrows indicate the direction of the air flow and are purple where the flow is stronger during Tmax compared to Tmin, which is the case for boreal and austral summer (a,b). Black arrows indicate where the flow is weaker during Tmax. Note the different colour scale for the annual mean.

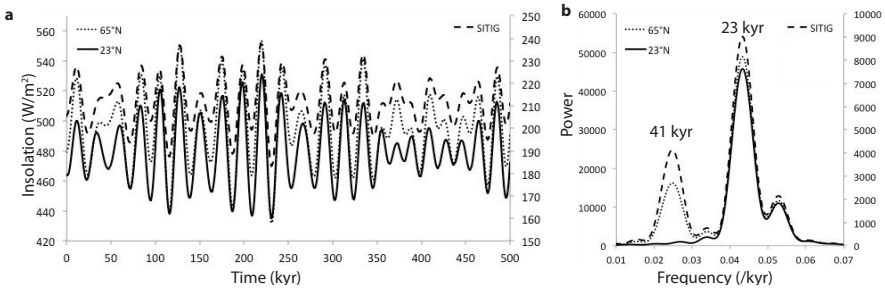

Figure 5.6: Insolation over the past 500 kyr (a) at 23°N (solid line) and 65°N (dotted line) on the left y-axis and SITIG (insolation difference between 23°N and 23°S at June 21^{st}, dashed line) on the right y-axis. (b) shows the power spectra of these three insolation curves, with peaks at 23kyr (precession) and 41kyr (obliquity), again the left y-axis is for 23°N and 65°N insolation, the right y-axis for SITIG.

6

Precession and obliquity forcing of the freshwater budget over the Mediterranean

Abstract

We investigate the separate precession and obliquity forcing of the freshwater budget over the Mediterranean using a high-resolution coupled climate model, EC-Earth. At times of enhanced insolation seasonality, i.e. minimum precession and maximum obliquity, the area was wetter and the Mediterranean Sea surface was less saline. This has been attributed to increased Nile runoff as a consequence of a strengthened North-African monsoon, as well as to increased precipitation over the Mediterranean Sea itself. Our results show that both mechanisms play a role in changing the freshwater budget, with monsoonal summer runoff being most important for precession and winter precipitation being most important for obliquity. We relate changes in winter precipitation to changes in the air-sea temperature difference. The freshening during minimum precession and maximum obliquity has a strong effect on Mediterranean sea surface salinity and mixed layer depth, thereby likely influencing deep sea circulation and sedimentation at the ocean bottom.

6.1 Introduction

The response of Mediterranean climate to orbital forcing is a heavily debated topic in paleoclimatology. A large body of data has shown that at times of enhanced insolation seasonality, i.e. minimum precession and maximum obliquity, the Mediterranean area was wetter and the Mediterranean Sea surface freshwater budget (evaporation minus precipitation and runoff) was reduced. Evidence for a wetter

This chapter is in preparation for publication as: Bosmans, J.H.C., S.S. Drijfhout, E. Tuenter, F.J. Hilgen, L.J. Lourens and E. J. Rohling (2014). Precession and obliquity forcing of the freshwater budget over the Mediterranean

climate and a fresher Mediterranean Sea at these times stems from pollen records (e.g. Rossignol-Strick, 1987), speleothem oxygen isotopes (e.g. Bar-Matthews et al., 2000) as well as sedimentary sequences (e.g. Rossignol-Strick, 1985; van der Laan et al., 2012). The Mediterranean sedimentary record shows numerous dark, organic-rich layers, the so-called sapropels, which formed on the sea floor at times of high northern hemisphere summer insolation. Rossignol-Strick (1985) proposed a physical link between the occurrence of these sapropels and orbitally forced increases in North-African monsoon strength, which consequently strengthens Nile runoff. Such an increase in runoff reduces the surface salinity of the Mediterranean Sea (MS), resulting in a more stable stratification of the MS, thereby reducing (or even eliminating) the formation of intermediate and deep water. Deep water formation supplies oxygen transport to the sea floor, hence a reduction in deep water formation promotes anoxic conditions and organic-rich sediment layers (Rossignol-Strick, 1985). Although the sapropels are mainly paced by precession, an obliquity pattern is present as well (e.g. Lourens et al., 1996).

The strengthening of the North-African monsoon during times of increased insolation seasonality, such as minimum precession and maximum obliquity, has been confirmed by many studies (Chapter 3, Bosmans et al. 2014; Kutzbach et al. 2013 and references therein). The subsequent increase in runoff towards the Mediterranean holds as the most widely adopted hypothesis for the formation of sapropels, appearing in handbooks on paleoclimatology (Ruddiman, 2007). However, other components of the Mediterranean climate may have played a role as well. Increased summer precipitation over the basin itself at times of increased summer insolation has been related to increased activity of summer depressions (Rohling, 1994; Rohling and Hilgen, 1991). This idea has however largely been abandoned in favour of increased winter precipitation, often attributed to increased Mediterranean storm track activity (Brayshaw et al., 2011; Kutzbach et al., 2013; Tzedakis, 2007). Furthermore, strong similarities between the sapropel record in the Mediterranean and sedimentary sequences in western Spain and Morocco suggests that both respond to orbital forcing in similar ways (Sierro et al., 2000; van der Laan et al., 2012). Atlantic storm tracks affect both western Spain and Morocco and can induce increased storm activity over the Mediterranean, hence increased storm track activity can explain wetter conditions at times of increased insolation seasonality in both regions. Increased (net) precipitation over the basin and increased runoff from the northern borderlands of the Mediterranean may be important factors in deep sea circulation (Meijer and Tuenter, 2007).

To summarise, orbitally forced changes in the Mediterranean freshwater budget, and therefore sapropel formation, have been attributed to various sources (for a literature overview see (Kutzbach et al., 2013; Tzedakis, 2007)). Kutzbach et al. (2013) state that not only monsoonal runoff but also winter precipitation at times of a precession minimum could explain humid periods in paleoclimatic records, but give no comparison of precipitation and runoff amounts. Meijer and Tuenter (2007) showed the relative roles of (net) precipitation and runoff from both north and south, but based their result on a low resolution intermediate complexity model. Both studies

focus on precession forcing, while obliquity leaves an imprint on the sapropel record as well (Lourens et al., 1996). In this study, we use a high-resolution general circulation model, EC-Earth, to investigate changes in the Mediterranean freshwater budget due to changes in both precession and obliquity. Specifically, we aim to determine the relative roles of precipitation, evaporation and runoff. Also, we examine the causes behind changes in these freshwater budget terms, in order to determine whether changes in the Mediterranean freshwater budget are mainly driven by the North-African monsoon, (Atlantic) storm tracks or local changes.

This paper starts with an overview of the model, EC-Earth, and a description of the experimental design (Section 6.2). We then briefly discuss the freshwater budget in a pre-industrial control experiment in Section 6.3.1, as an evaluation of EC-Earths capability of modelling Mediterranean climate. The main results are shown in Sections 6.3.2, 6.3.3 and 6.3.4, where we examine changes in (net) precipitation and runoff and examine possible causes. We also briefly touch upon the possible effects of the freshwater budget changes on deep water formation in Section 6.3.5. Section 6.4 provides a discussion; this study is concluded in Section 6.5.

6.2 Model and Experiment set-up

6.2.1 EC-Earth

EC-Earth is a fully coupled ocean-atmosphere GCM (general circulation model, Hazeleger et al. 2010, 2011). The atmospheric part of EC-Earth 2.2 is based on a weather forecast model, the Integrated Forecasting System (IFS), cycle 31R1, of the European Centre for Medium-range Weather Forecast (ECMWF). It runs at a resolution of roughly 1.125°x1.125° (T159) with 62 vertical levels. IFS cycle 31R1 has the Bechtold et al. (2008) convection scheme and the Balsamo et al. (2009) land surface scheme H-TESSEL, which includes a revised infiltration scheme with a subgrid surface runoff scheme. EC-Earth 2.2 does not include dynamic vegetation. The ocean component consists of NEMO (Nucleus for European Modelling of the Ocean), version 2, running at a horizontal resolution of nominally 1° with 42 vertical levels (Madec 2008; Sterl et al. 2011). The Mediterranean consists of 363 surface gridboxes in the horizontal on a curvilinear C-grid. NEMO incorporates the sea-ice model LIM2. The ocean, sea-ice, land and atmosphere are coupled through the OASIS3 coupler (Valcke and Morel, 2006).

EC-Earth performs well for the present-day compared to CMIP3 models and data in terms of climatology as well as interannual, spatial and temporal variability (Hazeleger et al., 2010, 2011). In Section 6.3.1 we briefly discuss the model's capability over the Mediterranean for a pre-industrial control experiment (as described in Chapter 2, Bosmans et al. 2012).

6.2.2 Experiments

In this study we use four experiments in which the precession and obliquity effects can be studied separately. The orbital configuration used in each experiment is summarised in Table 1.1.

During minimum precession (Pmin), when the precession parameter $e \sin(\pi+\tilde{\omega})$ is at its minimum value, Northern Hemisphere summer solstice occurs at perihelion (the point closest to the Sun). Seasonality of insolation is enhanced on the Northern Hemisphere and decreased on the Southern Hemisphere. During maximum precession (Pmax), Southern Hemisphere summer occurs at perihelion. Insolation differences at $\sim$40°N can be as large as 100 Wm^{-2} for precession and 20 Wm^{-2} for obliquity (see Figure 3.1). Only orbital parameters, and thus insolation, vary amongst the experiments, all other boundary conditions are kept at pre-industrial values. More details can be found in Chapter 3, where the same experiments are used to investigate the orbital forcing of the North-African monsoon. Furthermore, we briefly discuss a pre-industrial control experiment using boundary conditions as prescribed by the Paleoclimate Modelling Intercomparision Project (see http://pmip3.lsce.ipsl.fr). This pre-industrial experiment is described in Chapter 2 (Bosmans et al., 2012).

In this study we compare Pmin to Pmax, and Tmax to Tmin, i.e. we investigate the effect of increased summer and decreased winter insolation. These experiments were initiated from a pre-industrial control experiment. Each experiment is run for 100 years, of which the last 50 years are used to create the climatologies shown in this study. This is long enough for atmospheric and surface variables that are of interest to equilibrate to the forcing (see Chapter 3, Bosmans et al. 2014). The globally averaged tendency term of surface air temperature, dT/dt, is near-zero and shows no trend in all experiments (not shown).

We keep vernal equinox fixed at the 21^{st} of March and use the present-day calendar. This introduces some errors in the precession experiments, because the lengths of the seasons and the dates of the equinoxes and solstices change along the precession cycle (Joussaume and Braconnot, 1997). A celestial calendar, using angular months based on astronomical positions, would be more appropriate. However, because many others (e.g. Braconnot et al., 2008; Chen et al., 2011; Meijer and Tuenter, 2007; Tuenter et al., 2003), also use the present-day calendar, we maintain this calendar to facilitate comparison.

In order to investigate changes in the freshwater fluxes over the Mediterranean Sea, we discuss precipitation, evaporation and runoff. In EC-Earth, the land area is divided in drainage basins, four of which drain into the Mediterranean: the northern borderlands of the Mediterranean, the Nile, the northern Sahara and the Chad basin (Figure 6.4(c)). The Chad basin is at present an endorheic (closed) basin, draining in continental Lake Chad. EC-Earth, however, does not contain a lake model and therefore runoff from the Chad basin is routed to the Mediterranean (the Gulf of Sirte) in order to close the global water budget. In this study we use pre-industrial boundary conditions and therefore exclude Chad runoff when discussing the fresh-

water fluxes. Accordingly, runoff from the south is composed of Nile runoff and runoff from the northern Sahara (the latter term is very small). In Section 6.3.5 we briefly discuss the effects of changes in the freshwater fluxes on ocean circulation, which responds to the full freshwater flux including Chad runoff.

6.3 Results

6.3.1 Pre-industrial (control run)

Here we briefly describe the Mediterranean freshwater budget (precipitation, evaporation and runoff) for the pre-industrial control experiment, before discussing the orbital-induced changes in the next sections. Figure 6.1 shows that EC-Earth reproduces a typical Mediterranean climate over the basin, with evaporation dominating the freshwater budget, as well as dry summers, wet winters and runoff peaking in late summer / early autumn. Evaporation and precipitation are slightly overestimated in winter compared to the CMAP and ERA-Interim data sets (Dee et al. 2011; Xie and Arkin 1997, respectively), while net evaporation (E-P) is slightly underestimated in summer (not shown).

The spatial variation in precipitation and evaporation, is however captured well in EC-Earth in both the summer and winter half year (Figure 6.2). Most precipitation occurs in winter over the Adriatic Sea, northern Levantine and southern Sea of Sardinia. These are areas where the temperature difference between the relatively warm sea surface and cool air is strong, leading to convective precipitation.

The components of the freshwater budget over the Mediterranean Sea in EC-Earth are summarised in Table 6.1. The annual mean evaporation and precipitation, 3.37 and 1.54 mm/day respectively, are slightly overestimated compared to CMAP and ERA-Interim (Figure 6.1), but fit within the range of values given in literature (2.52 - 4.30 mm/day for evaporation, 0.7 - 1.92 mm/day for precipitation) based on observations and reanalyses (Adloff et al., 2011; Criado-Aldeanueva et al., 2012, and references therein). Annual mean runoff is 0.44 mm/day, mostly coming from the northern borderlands. This is close to, but slightly higher than, the 0.39 mm/day indicated by Ludwig et al. (2009).

The net loss (E-P-R) of 1.38 mm/day is compensated by inflow from the Atlantic and the Black Sea. The in- and outflow through the Strait of Gibraltar is overestimated (1.59 and 1.56 Sv in EC-Earth respectively, 1 Sv = 10^6 m^3/s, compared to 0.82 and 0.78 in Criado-Aldeanueva et al. 2012). This overestimation in the model is due to the strait being one gridbox wide, $\sim$90 km, compared to its actual size of $\sim$15 km (Criado-Aldeanueva et al., 2012; Sterl et al., 2011). The same problem affects the in- and outflow from the Black Sea, 0.144 and 0.138 Sv in EC-Earth respectively, compared to 0.038 and 0.03 Sv in Kanarska and Maderich (2008). The net inflow from the Atlantic, however, of 0.035 Sv fits well within the range of values in literature; the inflow from the Black Sea (0.006 Sv), is on the low end (Criado-Aldeanueva et al., 2012; Soto-Navarro et al., 2010, and references therein).

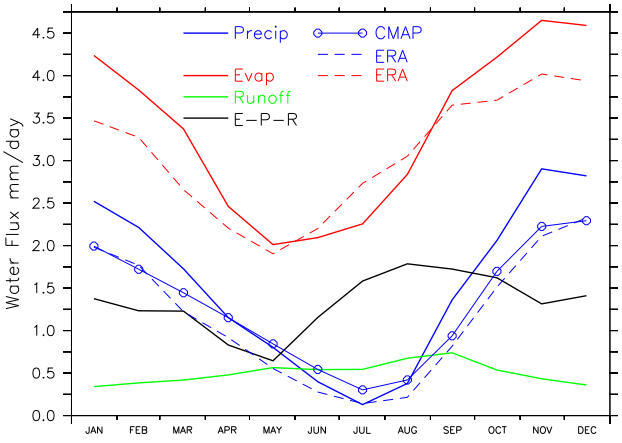

Figure 6.1: Precipitation, evaporation, runoff and E-P-R (net loss) over the Mediterranean Sea for the EC-Earth pre-industrial experiment (solid lines), CMAP (open dots, Xie and Arkin (1997)) and ERAinterim (dashed, Dee et al. (2011)) in mm/day. Only gridpoints over the Mediterranean Sea are taken into account.

In total, the inflow of Atlantic and Black Sea water adds an annual mean of 1.37 mm/day to the Mediterranean Sea, which compensates the net loss through evaporation (E-P-R) of 1.38 mm/day (Table 6.1).

6.3.2 Basin-mean precession- and obliquity-induced changes

The annual- and basin-mean changes over the Mediterranean Sea, as summarised in Table 6.1, indicate a freshening during Pmin and Tmax compared to Pmax and Tmin. For precession, the freshwater flux (P-E+R) is increased by 0.95 mm/day during Pmin, mostly due to increased runoff from the south (0.66 mm/day). Increased precipitation adds another 0.22 mm/day while the annual-mean evaporation change is negligible. For obliquity, evaporation does not contribute either to the annual mean freshwater flux changes (Table 6.1). Precipitation over the basin is increased by 0.16 mm/day during Tmax, making the largest contribution to the 0.25 mm/day total change in freshwater flux, followed by runoff from the south (0.11 mm/day).

The increase in precipitation over the basin is mostly due to increased precipitation in autumn and winter for both precession and obliquity (Figures 6.3(a) and 6.3(b)). During summer precipitation is slightly decreased. For precession, this summer precipitation decrease is compensated by lower evaporation, so net precipitation (P-E) shows only small changes during summer (Figure 6.3(c)). In autumn, increased evaporation overcompensates increased precipitation; P-E is reduced. In winter P-E shows the largest increase due to the combined effect of increased precipitation and decreased evaporation. For obliquity, P-E is increased in nearly all months as precipitation changes are more positive than evaporation changes Figure

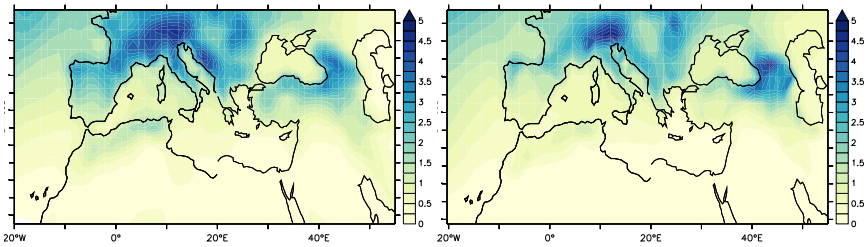

(a) Precip. EC-Earth AMJJAS mm/day

(b) Precip. ERA AMJJAS mm/day

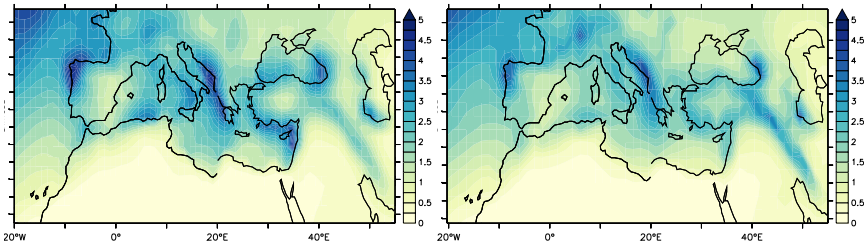

(c) Precip. EC-Earth ONDJFM mm/day

(d) Precip. ERA ONDJFM mm/day

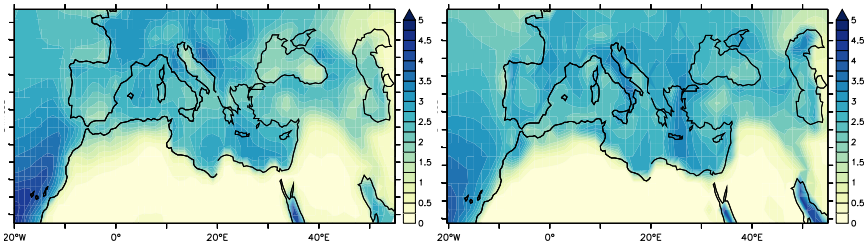

(e) Evap. EC-Earth AMJJAS mm/day

(f) Evap. ERA AMJJAS mm/day

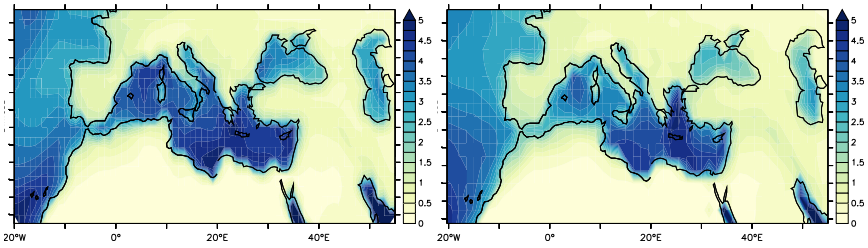

(g) Evap. EC-Earth ONDJFM mm/day

(h) Evap. ERA ONDJFM mm/day

Figure 6.2: Precipitation and evaporation in the EC-Earth pre-industrial experiment (left, a-c-e-g) and the ERA-Interim data set (right, b-d-f-h, Dee et al. 2011) for the summer half year (AMJJAS, a-b-e-f) and winter half year (ONDJFM, c-d-g-h).

Table 6.1: Annual mean values and changes in the components of the freshwater budget in mm/day averaged over the Mediterranean Sea (only gridpoints over the sea are taken into account). Both precipitation ("gain") and evaporation ("loss") are listed as positive values. Runoff from the south is from the Nile and Sahara basins, the runoff (R) and net loss (E-P-R) excludes Chad runoff. The last column shows the % change w.r.t. the pre-industrial.

	Pre-ind [mm/day]	Pmin [mm/day]	Pmax [mm/day]	Pmin-Pmax [mm/day]	(Pmin-Pmax) /PI %
Evaporation (E)	3.37	3.31	3.32	-0.01	-0.3%
Precipitation (P)	1.54	1.59	1.37	0.22	15%
River runoff (R)	0.44	1.02	0.31	0.71	160%
id. from north	0.30	0.31	0.27	0.04	15%
id. from south	0.14	0.70	0.04	0.66	474%
id. from Chad	0.06	0.95	0.01	0.94	1591%
Net loss (E-P-R)	1.38	0.70	1.65	-0.95	-72%
Net loss (with Chad)	1.33	-0.25	1.63	-1.89	-142%
Net inflow Gibraltar	1.17	-0.33	1.44	-1.77	-150%
Net inflow Black Sea	0.20	0.12	0.24	-0.12	-60%
	Pre-ind [mm/day]	Tmax [mm/day]	Tmin [mm/day]	Tmax-Tmin [mm/day]	Tmax-Tmin /PI %
Evaporation (E)	3.37	3.38	3.35	0.03	1.0%
Precipitation (P)	1.54	1.63	1.47	0.16	10%
River runoff (R)	0.44	0.60	0.47	0.13	29%
id. from north	0.30	0.32	0.30	0.02	7%
id. from south	0.14	0.28	0.17	0.11	79%
id. from Chad	0.06	0.34	0.10	0.24	402%
Net loss (E-P-R)	1.38	1.16	1.41	-0.25	-19%
Net loss (with Chad)	1.33	0.82	1.31	-0.49	-37%
Net inflow Gibraltar	1.17	0.77	1.21	-0.45	-38%
Net inflow Black Sea	0.20	0.12	0.16	-0.04	-20%

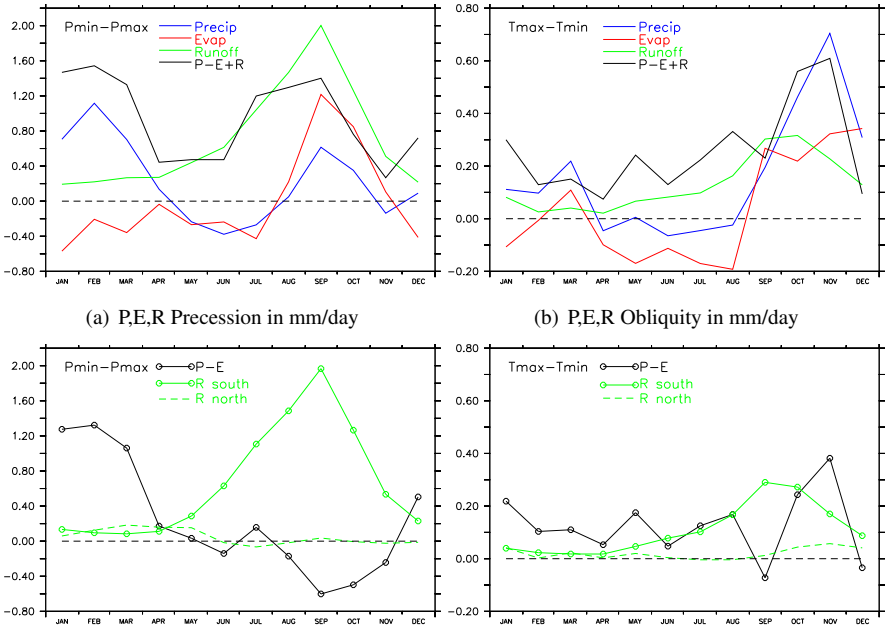

(a) P,E,R Precession in mm/day

(b) P,E,R Obliquity in mm/day

(c) P-E, R Precession in mm/day

(d) P-E, R Obliquity in mm/day

Figure 6.3: Precipitation, evaporation, runoff, P-E+R and P-E over the Mediterranean Sea, differences between experiments Pmin and Pmax (left), Tmax and Tmin (right) in mm/day. Note that the scales on the y-axes of a,c are different than those of b,d. Only gridpoints over ocean are taken into account.

6.3(d)).

Runoff is increased in all months, predominantly from the south in summer and early autumn (Figures 6.3(c), 6.3(d)). This increase in runoff is mostly from the Nile river (runoff from the Chad basin is ignored in Figure 3, see Section 6.2). There is a small increase in runoff from the north in late winter / early spring during Pmin, and during winter for Tmax (Figures 6.3(c), 6.3(d)).

Hence there is an overall increase in the freshwater budget (P-E+R), dominated by runoff from the south during Pmin and by winter precipitation during Tmax. In the next sections we focus on the mechanisms behind these freshwater budget changes. First we briefly look at the summer half year (AMJJAS), then we focus on the changes in winter half year (net) precipitation, which dominate the changes in winter freshwater flux (winter half year: ONDJFM).

6.3.3 Summer

The increased runoff from the south during Pmin and Tmax is in line with a strengthening of the North-African monsoon (Chapter 3, Bosmans et al. 2014 and references therein). Increased monsoonal precipitation results in increased surface runoff in the monsoon region, especially in the Nile and Chad drainage basins, see Figure 6.4 and Table 6.1. Runoff changes are especially large between Pmin and Pmax, due to strong differences in monsoon strength between Pmin and Pmax (Chapter 3, Bosmans et al. 2014). Runoff from the northern Mediterranean borderlands shows vary little change compared to that from monsoonal North-Africa (see also Figure 6.3).

Summer precipitation over the basin itself is lower during Pmin and Tmax (Figures 6.3(a), 6.3(b)). The increased summer insolation leads to higher air temperatures, resulting in lower relative humidity as well as a smaller air-sea temperature difference (Figures 6.8(a), 6.8(c)). The latter gives rise to a more stable (lower) atmosphere, giving less precipitation. Precipitation is reduced even more over southern Europe for precession (Figure 6.5(a)), explaining the (small) decrease in summer runoff from the north. At the same time precipitation over northern Africa and the Middle-East is increased for both precession and obliquity. Overall, net precipitation (P-E) is slightly reduced during summer for Pmin (Figure 6.3(c)). For obliquity, evaporation is reduced more than precipitation, resulting in a small increase in summer P-E (Figure 6.3(d)). Over the eastern Mediterranean, reduced evaporation (Figures 6.5(c), 6.6(c)) leads to increased P-E for both Pmin and Tmax (not shown).

6.3.4 Winter

The increase in (net) precipitation during Pmin and Tmax, occurs mostly in the winter months (Figure 6.3). Precipitation increases most over the eastern Mediterranean, over the Ionian and Levantine Seas (Figures 6.5(b), 6.6(b)), as well as near the coasts of Spain and Morocco. Winter precipitation increases have previously been attributed to increased storm track activity over the Mediterranean (e.g. Kutzbach et al., 2013). Here we find a reduced equator-to-pole winter temperature gradient and reduced storm tracks over the North Atlantic during Pmin and Tmax. Over the Mediterranean area the storm track activity, as indicated by the standard deviation of the 500 hPa geopotential height (Kaspar et al., 2007), is also reduced (Figures 6.7(a), 6.7(b)). Lower relative vorticity over the Mediterranean during Pmin further indicates reduced storm track activity (not shown). During Tmax there is a slight increase in storm activity west of Spain / Morocco (Figure 6.7(b)), where winter precipitation is increased (Figure 6.6(b)).

Using variance of sea level pressure (SLP) instead of 500 hPa geopotential height as a measure for storm track activity yields similar results, except that SLP variance is increased over western Spain / Morocco during Pmin (Figure 6.7(c)). Perhaps more shallow storms occur here, explaining the precipitation increase (Fig-

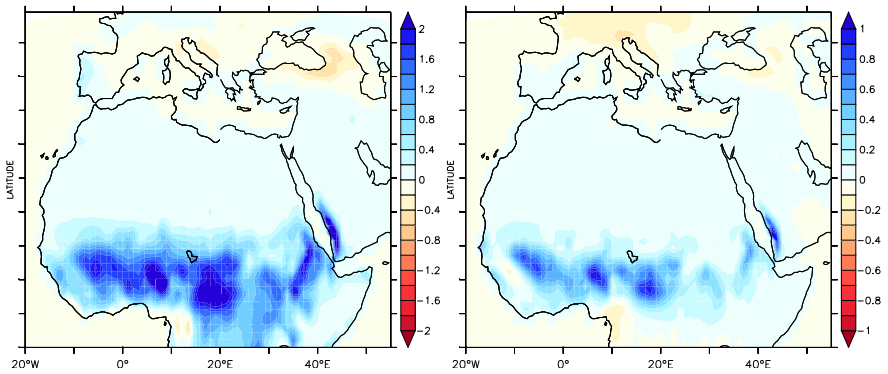

(a) Runoff Pmin-Pmax mm/day

(b) Runoff Tmax-Tmin mm/day

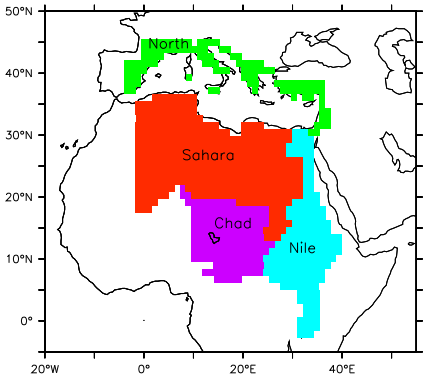

(c) Drainage basins

Figure 6.4: Annual mean runoff change over land for precession (a) and obliquity (b). Note the smaller colour scale in (b) compared to (a). Figure (c) shows the four drainage basins that drain into the Mediterranean in EC-Earth.

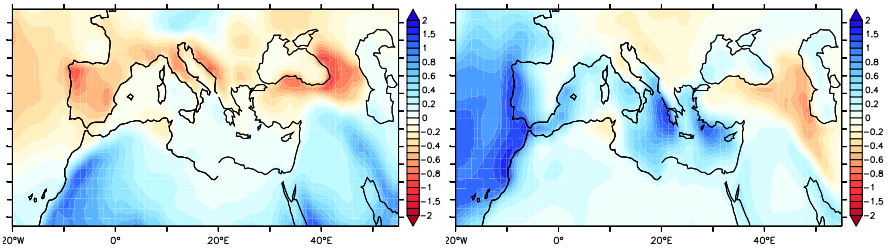

(a) Precip. Pmin-Pmax AMJJAS mm/day

(b) Precip. Pmin-Pmax ONDJFM mm/day

(c) Evap. Pmin-Pmax AMJJAS mm/day

(d) Evap. Pmin-Pmax ONDJFM mm/day

Figure 6.5: Precipitation and evaporation changes Pmin-Pmax in mm/day per half year (AMJJAS is April-September, ONDJFM is October-March). Positive values indicate increased precipitation or increased evaporation, blue colors indicate an increase in freshwater flux towards the surface.

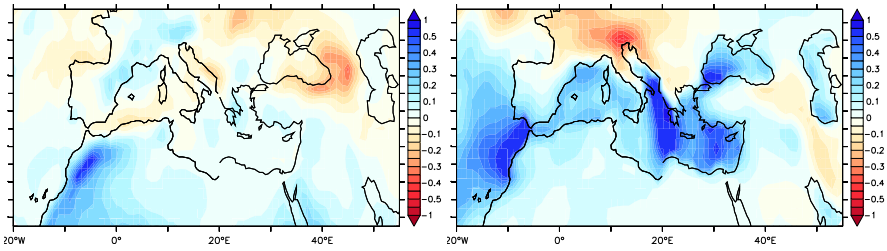

(a) Precip. Tmax-Tmin AMJJAS mm/day

(b) Precip. Tmax-Tmin ONDJFM mm/day

(c) Evap. Tmax-Tmin AMJJAS mm/day

(d) Evap. Tmax-Tmin ONDJFM mm/day

Figure 6.6: Precipitation and evaporation changes Tmax-Tmin in mm/day per half year (AMJJAS is April-September, ONDJFM is October-March). Positive values indicate increased precipitation or increased evaporation, blue colors indicate an increase in freshwater flux towards the surface.

ure 6.5(b)). During Tmax the increased storm tracks over this area are less clear from SLP (Figure 6.7(d)) during the winter half year, but during November-December (when precipitation changes for obliquity are largest) the increased storm track activity over Spain / Morocco appears in both the Z500 and SLP analyses.

Moreover, there is quite a contrast in precipitation changes over land and sea, which would not be the case if precipitation changes were due to increased storm track activity. A possible mechanism explaining the winter precipitation increase is a stronger contrast in sea surface and air temperatures (Figures 6.8(b), 6.8(d)). Both SST and surface air temperatures are reduced in winter due to reduced insolation, but surface air temperature decreases more strongly than SST. The latter lags the insolation forcing due to a strong heat capacity, increasing the temperature contrast and leading to more unstable conditions. Indeed most of the precipitation increase is convective, not large scale (the latter would be expected from increased storm activity), occuring over areas where the temperature contrast is reduced most. Only the precipitation increase near the coast of Spain / Morocco is partly large scale, in agreement with increased SLP variance over this area.

For precession, net precipitation is increased due to increased precipitation as well as reduced evaporation, while for obliquity increased evaporation counteracts the precipitation increase, especially in autumn / early winter (Figure 6.3(a), 6.3(b)).

6.3.5 Possible effects of changes in the freshwater budget on deep water formation

Here we briefly show changes in surface salinity and mixed layer depth, in order to describe possible effects of the above-mentioned precession- and obliquity-induced changes in the surface freshwater budget on ocean circulation. The general hypothesis is that at times of increased NH summer insolation, increased runoff from North-Africa into the Mediterranean reduces the surface salinity, resulting in a more stable stratification. With a more stable stratification there is a reduction (or even elimination) of intermediate and deep water formation, and therefore less supply of oxygen to the deep ocean, favouring the development of sapropels (Rossignol-Strick, 1985).

In the pre-industrial experiment, the mixed layer is deepest in winter in the southern Aegean Sea / northern Levantine and in the Gulf of Lyon (not shown), i.e. locations of intermediate and deep water formation, in line with the climatology of D'Ortenzio et al. (2005). The model does not reproduce a deep mixed layer in the Adriatic Sea, where small-scale ventilation is known to occur.

In the above we found an increased freshwater budget (P-E+R) during Pmin and Tmax, due to enhanced runoff and winter precipitation. Further freshening occurs through increased runoff from the Chad basin towards the Mediterranean (Table 6.1, Section 6.2). This freshening results in reduced salinity, as shown in Figures 6.9(a) and 6.9(b). These figures show the annual surface salinity changes; the pattern of salinity changes hardly varies per season (not shown). During Pmin, surface salinity

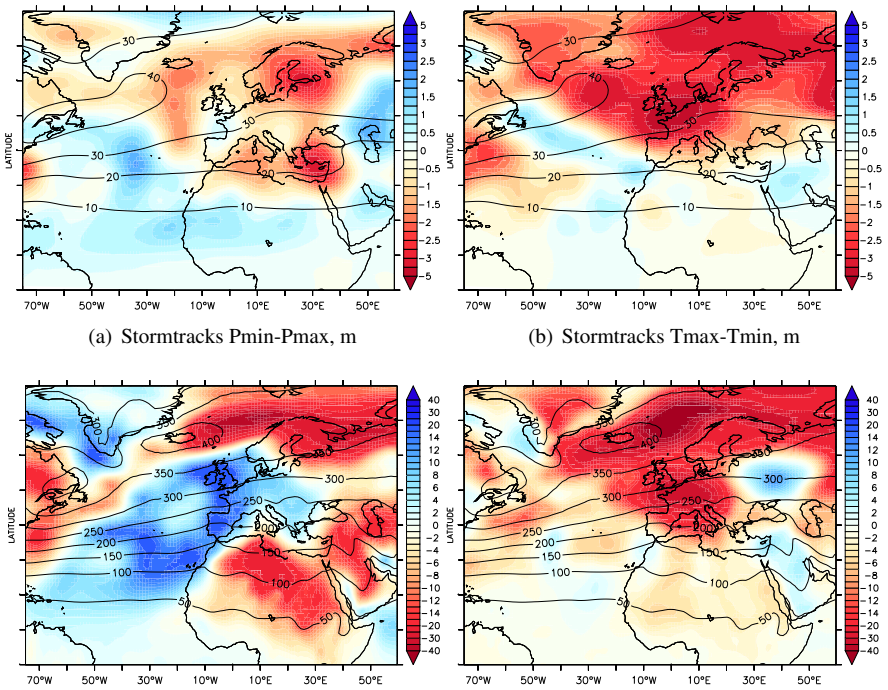

(a) Stormtracks Pmin-Pmax, m

(b) Stormtracks Tmax-Tmin, m

(c) Stormtracks Pmin-Pmax, Pa

(d) Stormtracks Tmax-Tmin, Pa

Figure 6.7: Storm track activity changes based on the standard deviation of 2.5 - 8 day filtered 500 hPa geopotential height for winter (a,b in meter) (ONDJFM). Also shown is storm track activity based on the variance of 2.5 - 8 day filtered sea level pressure for ONDJFM (c,d in Pa).

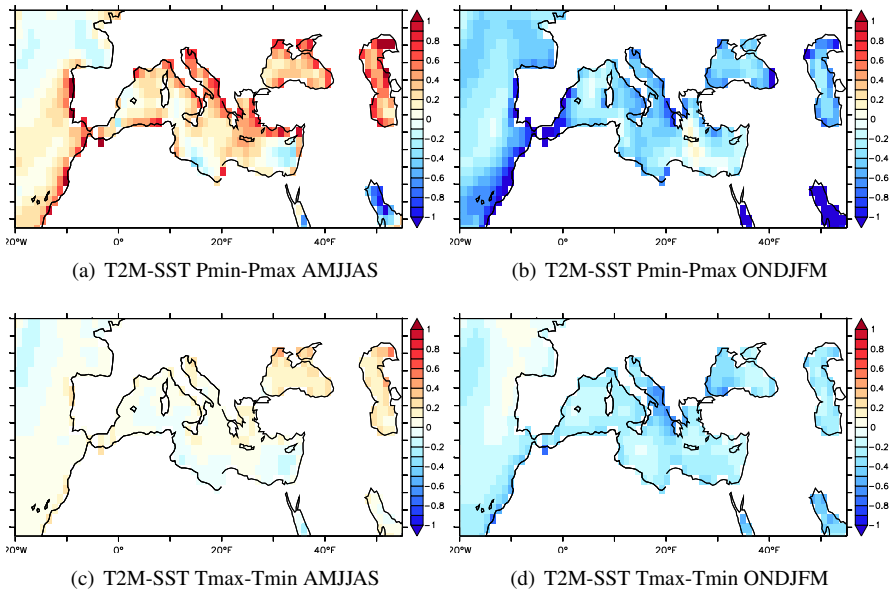

(a) T2M-SST Pmin-Pmax AMJJAS

(b) T2M-SST Pmin-Pmax ONDJFM

(c) T2M-SST Tmax-Tmin AMJJAS

(d) T2M-SST Tmax-Tmin ONDJFM

Figure 6.8: Differences in the T2M-SST difference in degrees. T2M is generally lower than SST, so negative values indicate a stronger difference, i.e. a more unstable condition.

is lower over the whole basin, mostly near the entrance points of runoff from the Nile and the Chad basin (the Nile delta and Gulf of Sirte, Figure 6.9(a)). During Tmax, salinity is decreased in the south-eastern part of the basin as well, while the western basin experiences little change (Figure 6.9(b)).

The freshening at the surface reduces the formation of intermediate and deep water, as exemplified by a reduction in the mixed layer depth during Pmin and Tmax (Figures 6.9(c), 6.9(d)). These figures show the mixed layer depth changes in February, which is when the mixed layer is deepest and most intermediate and deep water is formed. For precession, the largest changes occur at the area of intermediate water formation in the southern Aegean Sea / northern Levantine and in the Gulf of Lyon, a location of deep water formation. In the latter region the decrease in surface salinity is not as large as in the east, but a reduction in the northwesterly winds over this area in winter (not shown) further helps to reduce vertical mixing. During Tmax, the mixed layer depth in the Gulf of Lyon is increased compared to Tmin, while a shallower mixed depth occurs in the south-east where surface salinity is decreased.

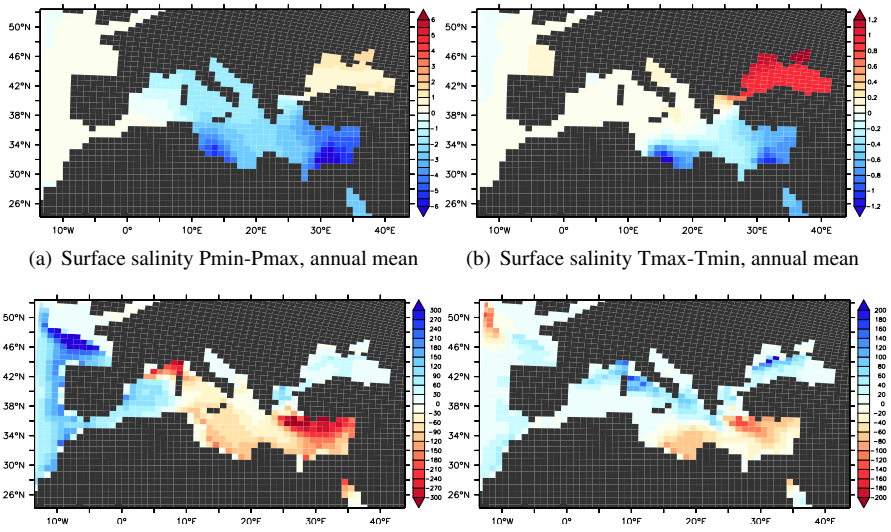

(a) Surface salinity Pmin-Pmax, annual mean

(b) Surface salinity Tmax-Tmin, annual mean

(c) Mixed layer depth Pmin-Pmax, February

(d) Mixed layer depth Tmax-Tmin, February

Figure 6.9: Surface salinity changes (a, b, annual) and changes in mixed layer depth (where density exceeds the surface density by 1%) (c,d, February). For mixed layer depth, negative values (red colours) indicate shallower depth. Note the salinity changes in the Gulf of Sirte due to increased runoff from the Chad basin, which was ignored in the freshwater flux discussed in this study. The colour key is larger for the precession than for the obliquity figures.

6.4 Discussion

In this study we have investigated orbitally forced changes in (net) precipitation and runoff over the Mediterranean. It is the first study of this subject to use a high resolution fully coupled GCM applying separate precession and obliquity forcing. We find that runoff from the south in summer and autumn dominates the changes in the freshwater budget, especially for precession. Increased winter precipitation over the basin also plays an important role, especially for obliquity.

6.4.1 Summer (monsoonal) runoff and precipitation

The strengthening of the North-African monsoon during Pmin and Tmax, forcing enhanced runoff from the south into the Mediterranean during summer and autumn, is in line with previous studies (Chapter 3, Bosmans et al. 2014; Kutzbach et al. 2013 and references therein). Over the basin itself precipitation is slightly decreased during summer, as opposed to the findings of Rohling (1994); Rohling and Hilgen (1991); Rossignol-Strick (1985). More recently, increased precipitation at times of high insolation seasonality has been attributed to winter precipitation instead of summer precipitation (Kutzbach et al., 2013; Tzedakis, 2007, and references therein), which is corroborated by our study. Tzedakis (2007) further notes that while palynological evidence suggests summer drought in the Mediterranean, isotopic evidence from Israeli speleothems suggest increased precipitation (Bar-Matthews et al., 2000). This apparent contradictory is resolved either by attributing increased precipitation in the Middle-East to winter precipitation, or by taking into account the strong land-sea contrast in the precipitation changes shown in our model results; while precipitation over the basin was lower in summer during Pmin and Tmax, the Middle East is slightly wetter in both summer and winter.

6.4.2 Winter precipitation

We find that changes in winter precipitation can be of the same order of magnitude as changes in (monsoonal) runoff, playing an important role in the freshwater budget changes, especially for obliquity. The simultaneous occurence of increased summer runoff and winter precipitation was also pointed out by Kutzbach et al. (2013); Meijer and Tuenter (2007). Meijer and Tuenter (2007) also point at enhanced winter runoff from the north during minimum precession, but in our experiments runoff from the north shows very little change. Kutzbach et al. (2013) attribute increased winter precipitation during Pmin to increased storm track activity, as do Brayshaw et al. (2011) for the Mid-Holocene. In our experiments, storm track activity is weakened over both the Mediterranean as well as the North-Atlantic during both Pmin and Tmax, presumably related to weaker meridional temperature gradients. There is as of yet no consensus on orbitally forced changes in the storm tracks: Kaspar et al. (2007) find increased Atlantic storm tracks and weakened Mediterranean storm tracks during the Eemian (a time of minimum precession), Hall and Valdes

(1997) show a slightly stronger Atlantic storm track during the Mid-Holocene, while Brayshaw et al. (2011) state that a southward shift and therefore reduced North-Atlantic and an increased Mediterranean storm tracks occur during the Early Holocene. In precession experiments similar to ours, Kutzbach et al. (2013) find increased Mediterranean storm tracks. These different findings may be related to differences in model parametrisations and resolution. Kutzbach et al. (2013) base their findings on a low resolution model ($\sim$3.75°), and note that in higher-resolution Eemian and Mid-Holocene experiments with the same model the changes in Mediterranean precipitation and surface pressure are similar, but not completely identical to changes in the extreme precession experiments. Our high-resolution model is better able to capture the storm tracks over both the North-Atlantic and the Mediterranean well. In this study we attribute increased winter precipitation to an increased temperature difference between the sea surface and overlaying air, causing more unstable conditions and more convective precipitation.

The assumption that increased winter precipitation is caused by increased storm track activity at times of enhanced insolation seasonality has also risen from the similarity between sapropel sequences in the Mediterranean and sedimentary sequences in western Spain and Morocco (Sierro et al., 2000; van der Laan et al., 2012). Both regions were wetter at times of enhanced insolation seasonality; increased storm track activity would provide more moisture to both regions. Here we show that the two regions might indeed receive more moisture simultaneously but for different reasons; at least part of the winter precipitation change increase over western Spain and Morocco may be related to storm tracks, while precipitation change over the Mediterranean basin is driven by local mechanism. Also, monsoonal precipitation may reach Morocco in summer (Chapter 3, Bosmans et al. 2014).

6.4.3 Mediterranean Sea deepwater formation

Both the increased winter precipitation and summer (monsoonal) runoff result in a fresher Mediterranean freshwater budget in all months during both Pmin and Tmax. The oceanic response to the increased freshwater flux is a reduction in salinity and mixed layer depth, indicating stronger stratification and less intermediate and deep water formation. Such changes are in line with the formation of sapropels at times of enhanced insolation seasonality (e.g. Rossignol-Strick, 1985). We cannot determine whether summer runoff or winter precipitation is the dominant forcing of changes in stratification and deep water formation. Winter precipitation may be more important for deep water formation, as the latter occurs in the winter months and winter precipitation changes are strong over the northern Levantine and the Adriatic / Ionean sea, regions of intermediate- and deepwater formation. Further investigation with a regional ocean model could shed more light on the dominant mechanism of changes in salinity and stratification. This was previously endeavored by Meijer and Tuenter (2007). However, the freshwater forcing in their study derived from a intermediate complexity model (EC-Bilt), which showed a different response to the same orbital forcings as EC-Earth (Chapter 3, Bosmans et al. 2014), and their ocean model did

not simulate the full circulation. Also, the oceanic response in EC-Earth includes a response to changes in Chad runoff, which could be excluded in a future sensitivity study in order to investigate the oceanic response to precession and obliquity under more realistic (geologically recent) boundary conditions. Further back in time, during the late Miocene, Chad runoff may have entered the Mediterranean (Gladstone et al., 2007; Griffin, 2011). Our study shows that Chad runoff could play a large role in the Mediterranean freshwater budget and therefore the ocean circulation. However the Mediterranean topography was quite different during the Miocene, so the role of Chad runoff at that time needs to be investigated using Miocene boundary conditions.

6.5 Conclusions

Based on our EC-Earth experiments of the separate precession and obliquity signals, we conclude that orbitally forced changes in the Mediterranean freshwater budget are mainly driven by river runoff from the south and winter precipitation over the basin itself. River runoff from the south, related to the strength of the North-African monsoon, dominates the freshwater budget changes for precession. Changes in winter precipitation, which we relate to a stronger air-sea temperature difference instead of storm track activity, dominate freshwater budget changes for obliquity. The freshening during minimum precession and maximum obliquity have a strong effect on Mediterranean surface salinity and mixed layer depth, and may therefore lead to stratification and consequently sapropel formation.

A

Appendix: From orbital parameters to insolation

A.1 Introduction

This document describes which equations and variables are necessary to compute the insolation, the incoming solar radiation, at any time and latitude. Firstly the six orbital parameters needed to uniquely specify the Earth's orbit will be discussed in section A.2. From these parameters the insolation is calculated, which is explained in section A.3. Section A.4 elaborates on the astronomical functions in EC-Earth and how and where insolation is calculated.

A.2 The six orbital parameters

The well-known parameters in the Milankovitch theory are eccentricity, obliquity and precession. However, in general Keplerian astronomy there are six parameters which together uniquely define the orbit of a planet around a sun. The eccentricity e describes how elliptic the orbit is. The earth's eccentricity varies from 0.0034 to almost 0.058 due to gravitational interactions with other planets. The second parameter is the semi-major axis of the ellipse a. In combination with the ellipticity and the true anomaly (discussed below), the Earth-Sun distance can be calculated at each point of the orbit. The inclination i is the angle between the plane of the Earth's orbit and the ecliptic plane. The longitude of the ascending node, Ω, is in the plane of reference and is the angle between a reference direction (vernal point) and the ascending node (where the orbit intersects upwards through the plane of reference). The argument of periapsis (perihelion), ω, is the angle between the ascending node and the periapsis (or the semi-major axis). This determines the position of the elliptic orbit with respect to the reference plane, and therefore also in which seasons the equinoxes and solstices occur. The last of the six parameters

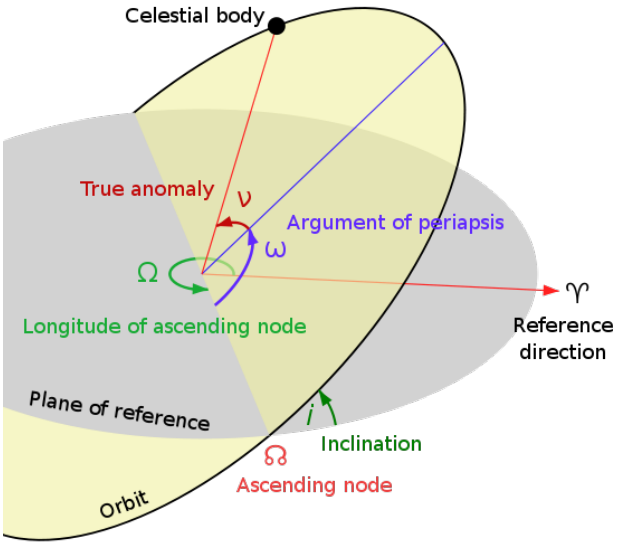

Figure A.1: A schematic drawing of the orbital parameters. In this case the orbit is around the Sun, the Earth being the 'celestial body' and the plane of reference being the ecliptic.

of Keplerian orbits is the mean anomaly M. This is the time since the last passing of the perihelion multiplied by $2\pi/T$, where T is the duration of a full orbit. It increases uniformly during the orbit and can also be seen as the true anomaly (see below) when i and eccentricity are zero.

Besides these six parameters there are others that are used in orbital calculations. One that was mentioned already is the true anomaly ν, the angle in the orbital plane between the Earth and perihelion (as seen from the Sun). This parameter is also shown in Figure A.1. It is also sometimes referred to as θ. Due to the eccentricity of the orbit, ν does not increase uniformly during the orbit, as opposed to M. To calculate ν from M, the equation of centre is used. This will be discussed in Section A.3.

From the argument of periapsis ω and the longitude of the ascending node Ω, the longitude of periapsis (perihelion) is calculated: $\bar{\omega} = \omega + \Omega$. This is the angle (or longitude, measured counter clockwise) at which the periapsis would occur as seen from vernal equinox, if i=0. For the Earth, $i \neq 0$, so $\bar{\omega}$ is a 'broken' angle as it is the sum of ω in the orbital plane and Ω in the reference plane. Then there is also $\widetilde{\omega}$, also the angle between vernal equinox and perihelion, but in the orbital plane. It is a measure of climatic precession. Currently the NH winter occurs close to perihelion, so $\widetilde{\omega}$ is around 270°.

Of the variables discussed so far, some can be considered constant throughout

an Earth-year: eccentricity e, the semi-major axis a, inclination i, longitude of the ascending node Ω, the argument of periapsis ω, the longitude of perihelion $\bar{\omega}$, climatic precession $\widetilde{\omega}$ and the positions of the equinoxes and solstices. Variables that do change over the year are the mean anomaly M, true anomaly ν, true longitude λ, mean longitude λ_m and declination δ. The true longitude is the angle between vernal equinox and the position of the planet, measured counter clockwise. The mean longitude λ_m is the same angle if e and i are zero. Therefore, λ_m changes uniformely with time, whereas λ does not ($\frac{\delta\lambda}{\delta t}$ is not constant). The solar declination δ determines at which latitude the Sun is perpendicular to the surface. It depends on true longitude λ and obliquity ε, the tilt of the earth, and its maximum value is $\pm\varepsilon$ at the solstices.

To calculate the insolation received by the Earth during the day, two more variables are needed. The hour angle H is the time since the Sun was at the local meridian. It ranges from $-\pi$ at sunrise to π at sunset. The zenith angle θ (sometimes z) is the angle between the zenith (pointing upwards perpendicular to the surface) of an observer and the Sun. It is therefore 0° for an observer on the equator at noon during the equinoxes.

A.3 Calculation of insolation

This part follows from Berger (1978), Tuenter (2004) and the EC-Bilt and EC-Earth models.

In the EC-Earth model it is necessary to know the incoming solar radiation at every latitude at every time step. This insolation is calculated from the solar constant (S, roughly 1365 Wm^{-2}) and the zenith angle. This may seem straightforward, but for the calculation of the zenith angle many of the parameters mentioned above need to be calculated first. This section discusses the necessary equations, the next section will explain how EC-Earth deals with these equations.

The zenith angle z and the solar constant determine the incoming radiation as follows:

$$W(\phi,\lambda,H) = S_a(\frac{a}{r})^2 cosz \tag{A.3.1}$$

In this equation, S_a is the solar energy per unit of time on a surface of unit area perpendicular to the Sun's rays and a the semi-major axis of the orbit. r is the actual distance from the Sun and z is the zenith angle, depending on the latitude on Earth ϕ, the hour angle H (a measure of time of day) and declination δ. The zenith angle is determined as follows:

$$cosz = sin\phi\ \sin\delta + cos\phi\ \cos\delta\ \cos H \tag{A.3.2}$$

Declination δ is related to true longitude λ (a measure of time of year) and obliquity ε as follows:

$$sin\delta = sin\lambda \sin\varepsilon \tag{A.3.3}$$

Besides the zenith angle, the Earth-Sun distance r is also necessary to calculate the insolation using Equation A.3.1. This varies throughout the year:

$$r = \frac{a(1-e^2)}{1+e\cos\nu} \tag{A.3.4}$$

where ν can be calculated from the true longitude and the climatic precession:

$$\nu = \lambda - \widetilde{\omega} \tag{A.3.5}$$

All of the above equations can be combined to find that the insolation depends on the solar constant, eccentricity, true longitude, climatic precession, latitude, obliquity, declination and hour angle:

$$W(\phi,\lambda,H) = S_a(\frac{(1+e\cos(\nu))^2}{(1-e^2)^2} sin\phi \sin\lambda \sin\varepsilon + cos\phi \cos\delta \cos H \tag{A.3.6}$$

In climate models, a calculation of the true longitude is needed to solve Equation A.3.6. This calculation starts with letting the origin of time be the 21^{st} of March, the vernal equinox. This way, $\lambda_{t=0} = 0$. Then the mean longitude at the vernal equinox is computed (it is not zero at the same time as λ due to inclination):

$$\begin{aligned}\lambda_{m0} = \lambda_0 - 2[&(\frac{1}{2}e + \frac{1}{8}e^3)(1+\beta)sin(\lambda_0 - \widetilde{\omega}) - \\ &\frac{1}{4}e^2(\frac{1}{2}+\beta)sin2(\lambda_0-\widetilde{\omega}) + \frac{1}{8}e^3(\frac{1}{3}+\beta)sin3(\lambda_0-\widetilde{\omega})]\end{aligned} \tag{A.3.7}$$

where

$$\beta = \sqrt{1-e^2} \tag{A.3.8}$$

Now that the 'starting value' is known, each value of λ_m can be determined through an increment $\Delta\lambda_m$, because the rate of increase of λ_m is constant. For instance, daily increments can be used:

$$\lambda_m = \lambda_{m0} + l\frac{\pi}{180} \tag{A.3.9}$$

where l is the number of days since the vernal equinox. This mean longitude is used to find the true longitude:

$$\lambda = \lambda_m + (2e - \frac{1}{4}e^3)sin(\lambda_m - \widetilde{\omega}) + \frac{5}{4}e^2 sin2(\lambda_m - \widetilde{\omega}) + \frac{13}{12}e^3 sin3(\lambda_m - \widetilde{\omega}) \quad \text{(A.3.10)}$$

Another point of consideration is that Equation A.3.6 has to be adapted for latitudes north / south of the polar circles at $90^\circ - \varepsilon$ N / S. In these areas there is no sunset in summer time and no sunrise in winter time (W=0).

A.4 How to model paleo-insolation in EC-Earth

Section A.3 described how insolation W can be calculated from various parameters. This section shows how these calculations are incorporated in EC-Earth. This model is currently not suitable for paleo-experiments because only insolation for present-day $\pm$ a few hundred years is calculated. The second subsection will explain what needs to be changed in EC-Earth to allow for paleo-experiments.

A.4.1 Insolation in the 'present-day' version

There is a header file called fcstast.h (see A), which includes astronomical functions that can only be used for dates no more than a few centuries before or after 2000. It uses 'PTETA', which is the fractional date in years since 2000. Mean longitude λ_m is calculated using an empirical function derived from Equation A.3.7 and only depends on PTETA. This is a good indication that the model is only dealing with present-day condition: λ_m is calculated using a constant value for eccentricity and precession. The Earth-Sun distance is changed throughout the year depending on λ_m. The mean anomaly M is also calculated as an angle as a function of PTETA. The true longitude λ is a function of λ_m, with contants derived from Equation A.3.10; also using constant values for eccentricity and precession. From the true longitude λ and the eccentricity ε (a prescribed constant in EC-Earth), the declination δ follows.

The last calculation in fctast.h concerns the equation of time, which gives the difference between solar time and GMT. Due to eccentricity the Earth's angular velocity is not constant and the length of a solar day changes throughout the year. This follows from Kepler's second law (the line between the Earth and the Sun sweeps out equal areas per unit time). A solar day can be up to 15 minutes longer or shorter than a 'GMT day' of 24 hours. Part of the equation of time is the equation of centre:

$$C = \nu - M \quad \text{(A.4.1)}$$

This equation is used to find the true anomaly ν from M, which changes uniformly in time, whereas ν doesn't. This is an approximation of C to the third order:

$$C = 2e\ \sin M + \frac{5}{4}e^2 \sin\ 2\mathrm{M} + \frac{1}{12}e^3(13\ \sin\ 3\mathrm{M}\ -\ 3\ \sin\ \mathrm{M})\ldots \tag{A.4.2}$$

Combining Equations A.4.1 and A.4.2 leads to ν. The second part of the equation of time, *R* is as follows:

$$R = -\ \tan^2\frac{e}{2}\ \sin\ 2\ \lambda + \frac{1}{2}\tan^4\frac{e}{2}\sin\ 4\ \lambda \tag{A.4.3}$$

Because *M* changes uniquely in time throughout the year while λ doesn't, it's most likely that *C* is the GMT-part of the equation of time and *R* the solar part. The equation of time (solar time - GMT) is:

$$\mathrm{Eq.Time} = \frac{86400}{2\pi}(R - C) \tag{A.4.4}$$

where the factor in front of (R-C) is seconds/radians.

These calculations, in fctast.h, are called at various points in EC-Earth. Here is a list of routines that use RRS (earth-sun distance), RDS (declination) and RET (equation of time) or only RDS and RET from fctast:

ifs/src/ifs/phys_dmn/suphmnh.F90 uses declination and equation of time in initialisation of surface scheme.

ifs/src/ifs/phys_dmn/updtier15.F90 updates time for full radiation computations, using all three variables.

ifs/src/ifs/phys_ec/updtier.F90 similar to updtier15.F90.

ifs/src/ifs/pp_obs/fpcincape.F90 includes fctast but subsequently does not use the computed variables.

ifs/src/ifs/setup/sucst.F90 defines lenght of day in seconds, the semi-major axis and obliquity. From fctast it defines Earth-Sun distance, declination and equation of time.

ifs/src/ifs/utility/reset_accfie_vareps.F90 includes fctast but subsequently does not use the computed variables.

ifs/src/ifs/utility/tsl.F90 calculates lengths of days and nights, including polar days and nights using solar angle μ.

ifs/src/ifs/utility/updtim.F90 updates model time. Uses all three variables to define Earth-Sun distance, declination and equation of time three times in this routine.

ifs/src/ifs/adiab/cppsolan.F90 computes mean solar angle μ.

The equations from fctast.h also included in the routine soilinc.F90. This includes a subroutine calculating the solar angle and a subroutine SUCONS, where a value of obliquity, semi-major axis and a solar constant is given. The subroutine 'solar_angle' uses the same calculations that are also in fctast.h and fcttim.h and then calculates solar angle μ (cosine of zenith angle, see Equation A.3.2). Therefore the zenith angle, needed to calculate incoming solar radiation, is calculated at multiple points in the model using latitude, time and declination. Together with the Earth-Sun distance and the insolation at TOA (S) this gives the incoming solar radiation at each time and latitude (Equation A.3.1).

In the routine updrgas.F90, GHG concentrations and monthly and annual values of insolation at TOA are read from either measurements (1850-2000) or based on scenarios (up to 2100). For CMIP runs these values are prescribed by CMIP data sets, otherwise values from Krivova and Solanki (2002) are used. The parameter 'RSOLINC' is the resulting insolation.

A.4.2 How to change EC-Earth for paleo-experiments

The general idea is to set one or more 'paleo-flags', for instance 'paleo_midholocene', 'paleo_maxobl', 'paleo_minprec' etcetera. For each of these flags, the obliquity, precession, eccentricity and GHG concentrations need to be specified. This section describes where to define the flags, and in which routines the flags need to be used in 'IF' statements. An example of the use of flags is calendar.F90.

The routine fctast.h has been rewritten to calculate RDS, RRS and RET for prescribed values of obliquity, precession and eccentricity (see A.6). The new version, fctast_paleo.F90 will be included in the model and called when a 'paleo-flag' is set.

The following flags need to be set:

- NHINCSOL = 0 (No variability of solar constant is accounted for)
- LECO2VAR = True (ERA-40/AMIP2 variability of GHG is off)
- LHGHG = True (variability of GHG (including CO2) is off)
- NSCEN = a number (GHG scenario, A1B etc. necessary if GHG var. is off)
- NRCP = a number (RCP for CMIP5. necessary if GHG var. is off)
- LPAL_INS = True (to acces fctast_paleo and use paleo GHG)
- LCMIP5 = True (flag for CMIP runs)
- AEROCON = 0 (pre-industrial aerosols)

In subroutine SUECRAD.F90, I have set LCMIP5 to True, as well as Leco2var and Lhghg. Nhincsol is set to 0, Nscen to 1 and Rsolinc to RI0. This subroutine also

defines background [GHG], which are set to 1850 values (RCCO2 etc). I have added a flag LPAL_INS, set to TRUE, which is also included in YOERAD and NAERAD. In YOMCST I've added the variables RECC (eccentricity), RPRE (precession, as longitude of perihelion measured from v.e.), PAL_RRS, PAL_RDS and PAL_RET. Obliquity (REPSM) is already included. In sucst.F90 I've added the value declaration of REPSM, RECC and RPRE (if paleo flag is on). Also, when the paleo-flag is on, paleo-values are used for ZRS, ZDE and ZET (from fctast_paleo.f90) and these are written out (if PRINTLEV flag is on). In updtim.F90, updtier.F90, tsl.F90, soilinc.F and cppsolan.F90 a call to fctast_paleo is included now as well for paleo-settings. The calendar is set to Gregorian (as in PI, 365.25 days/year, see module Calendar). RI0 (solar constant) is set to 1365.6 Wm^{-2} in soilinc.F and sucst.F90. This is the 1844-1856 average, also set in updrgas.F90, as well as GHGs. Updrgas.F90 is used because I've kept LECO2VAR and LHGHG as true, but if LPAL_INS is set to TRUE as well, GHG concentrations and insolation are set to paleo-values. LCMIP5 is set to True, Aerocon to 0 (to create conditions most similar to the PI experiment).

A headerfile has been created in ifs/src/include/31r1/ifs and an #include statement has been placed in sucst.F90, updtim.F90, updtier.F90, tsl.F90, soilinc.F and cppsolan.F90.

The subroutine fctast_paleo.F90 itself is based on fctast.h, Berger (1978), and help from A. Voldoire and W.J. van de Berg.

During setup the routine sucst.F90 is called from su0yomb.F90, so values of RRS, RDS and RET can be checked straight away. This call uses a print level of -1, ensuring these values are written out only during setup. Using a test version of fctast_paleo, fctast_test, I've ensured that this subroutine is entered.

A.5 The code in fctast.h

```
!     ------------------------------------------------------------------

! -- Astronomical functions
! RRS is the distance Sun-Earth
! RDS is the declination of the Earth
! RET is the equation of time

! Orbit of the earth

REAL(KIND=JPRB) :: RTETA,REL,REM,RRS,RLLS,RLLLS,RDS,RET
REAL(KIND=JPRB) :: PTIME,PTETA
```

```
!     Modified 24-Jan-2008 C. Severijns - ECEARTH-R0
RTETA(PTIME)=PTIME/(RDAY*Calendar_mean_days_per_year)
! Sources including this file should also use calendar
REL(PTETA)=1.7535_JPRB+6.283076_JPRB*PTETA
REM(PTETA)=6.240075_JPRB+6.283020_JPRB*PTETA
RRS(PTETA)=REA*(1.0001_JPRB-0.0163_JPRB*SIN(REL(PTETA))&
          &+0.0037_JPRB*COS(REL(PTETA)))
! Relative movement Sun/Earth
RLLS(PTETA)=4.8951_JPRB+6.283076_JPRB*PTETA
RLLLS(PTETA)=4.8952_JPRB+6.283320_JPRB*PTETA-0.0075_JPRB&
           &*SIN(REL(PTETA))-0.0326_JPRB*COS(REL(PTETA))&
           &-0.0003_JPRB*SIN(2.0_JPRB*REL(PTETA))&
           &+0.0002_JPRB*COS(2.0_JPRB*REL(PTETA))
RDS(PTETA)=ASIN(SIN(REPSM)*SIN(RLLLS(PTETA)))
RET(PTETA)=591.8_JPRB*SIN(2.0_JPRB*RLLS(PTETA))-&
           &459.4_JPRB*SIN(REM(PTETA))+39.5_JPRB&
           &*SIN(REM(PTETA))*COS(2.0_JPRB*RLLS(PTETA))&
           &-12.7_JPRB*SIN(4._JPRB*RLLS(PTETA))-&
           &4.8_JPRB*SIN(2.0_JPRB*REM(PTETA))
```

A.6 The code in fctast_paleo.h

```
!     ------------------------------------------------------------------
USE PARKIND1   ,ONLY : JPRB
USE YOMHOOK    ,ONLY : LHOOK,    DR_HOOK
USE CALENDAR   ,ONLY : Calendar_mean_days_per_year
USE YOMCST     ,ONLY : RPI, REA, REPSM, RECC, RPRE

IMPLICIT NONE

REAL(KIND=JPRB) :: REL,RRS,RLLLS,RDS,RET
REAL(KIND=JPRB) :: PTETA, PTETA_help
REAL(KIND=JPRB) :: RBETA, REL_0, RLLLS_0, RET_C, RET_R

RLLLS_0          = 0._JPRB
        !IFF V.E. (March 21st) IS 't=0'!!!
        !For this PTETA needs to be adapted, see below

RBETA = SQRT(1-RECC**2)

REL_0 = RLLLS_0 -2*((RECC/2 + RECC**3/8)*(1+RBETA)&
       &*SIN(RLLLS_0-RPRE) -RECC**2/4*(1/2+RBETA)&
```

```
        &*SIN(2*(RLLLS_0-RPRE))+ &
        & RECC**3/8*(1/3+RBETA)*SIN(3*(RLLLS_0-RPRE)))

PTETA_help = PTETA - FLOOR(PTETA)
PTETA_help = PTETA_help * Calendar_mean_days_per_year+1.
PTETA_help = PTETA_help - (31._JPRB+28._JPRB+21._JPRB)
        !shift so that t=0 at v.e.
if (PTETA_help.lt.0) PTETA_help = PTETA_help &
        &+ Calendar_mean_days_per_year

REL     = REL_0 + PTETA_help*RPI*2._JPRB&
        &/Calendar_mean_days_per_year
RLLLS   = REL + (2.*RECC-RECC**3./4.)*SIN(REL-RPRE)&
        &+ 5.*RECC**2./4.*SIN(2.*(REL-RPRE))&
        &+ 13.*RECC**3./12.*SIN(3.*(REL-RPRE))
RDS     = ASIN(SIN(RLLLS)*SIN(REPSM))
RRS     = REA*(1-RECC**2.)/(1+RECC*COS(RLLLS-RPRE))
RET_C   = 2.*RECC*SIN(REL-RPRE) + 5.*RECC**2./4.&
        &*SIN(2.*(REL-RPRE)) + RECC**3./12.&
        &*(13.*SIN(3.*(REL-RPRE))-3.*SIN(REL-RPRE))
RET_R   = -TAN(REPSM/2.)**2.*SIN(2.*RLLLS)&
        &+ 0.5*TAN(REPSM/2.)**4.*SIN(4.*RLLLS)
RET     = -(RET_R + RET_C) * 86400./(2.*RPI)
```

Bibliography

Abram, N. J., Gagan, M. K., Liu, Z., Hantoro, W. S., McCulloch, M. T., and Suwargadi, B. W.: Seasonal characteristics of the Indian Ocean Dipole during the Holocene epoch, Nature, 445, 299–302, 2007.

Adloff, F., Mikolajewicz, U., Kucera, M., Grimm, R., Maier-Reimer, E., Schmiedl, G., and Emeis, K.-C.: Upper ocean climate of the Eastern Mediterranean Sea during the Holocene Insolation Maximum - a model study, Climate of the Past, 7, 1103–1122, doi:10.5194/cp-7-1103-2011, 2011.

Antico, A., Marchal, O., Mysak, L., and Vimeux, F.: Milankovitch Forcing and Meridional Moisture Flux in the Atmosphere: Insight from a Zonally Averaged Ocean-Atmosphere Model, Journal of Climate, 23, 4841–4855, 2010.

Baker, P. A., Seltzer, G. O., Fritz, S. C., Dunbar, R. B., Grove, M. J., Tapia, P. M., Cross, S. L., Rowe, H. D., and Broda, J. P.: The History of South American Tropical Precipitation for the Past 25,000 Years, Science, 291, 640–643, doi: 10.1126/science.291.5504.640, 2001.

Balsamo, G., Viterbo, P., Beljaars, A., van den Hurk, B., Hirschi, M., Betts, A. K., and Scipal, K.: A Revised Hydrology for the ECMWF Model: Verification from Field Site to Terrestrial Water Storage and Impact in the Integrated Forecast System, Journal of Hydrometeorology, 10, 623–643, doi:10.1175/2008JHM1068.1, 2009.

Bar-Matthews, M., Ayalon, A., and Kaufman, A.: Timing and hydrological conditions of Sapropel events in the Eastern Mediterranean, as evident from speleothems, Soreq cave, Israel, Chemical Geology, 169, 145–156, 2000.

Bartlein, P. J., Harrison, S. P., Brewer, S., Connor, S., Davis, B. A. S., Gajewski, K., Guiot, J., Harrison-Prentice, T. I., Henderson, A., Peyron, O., Prentice, I. C., Scholze, M., Seppa, H., Shuman, B., Sugita, S., Thompson, R. S., Viau, A. E., Williams, J., and Wu, H.: Pollen-based continental climate reconstructions at 6 and 21 ka: a global synthesis, Climate Dynamics, 37, 775–802, doi:10.1007/s00382-010-0904-1, 2011.

Bechtold, P., K, M., Jung, T., Doblas-reyes, F., Leutbecher, M., Rodwell, M. J., Vitart, F., and Balsamo, G.: Advances in simulating atmospheric variability with the ECMWF model : From synoptic to decadal time-scales, Quaterly Journal of the Royal Meteorological Society, 134, 1337–1351, doi:10.1002/qj, 2008.

Behling, H.: South and southeast Brazilian grasslands during Late Quaternary times: a synthesis, Palaeogeography, Palaeoclimatology, Palaeoecology, 177, 19–27, 2002.

Berger, A. L.: Long-Term Variations of Daily Insolation and Quaternary Climatic Changes, Journal of the Atmospheric Sciences, 35, 2362–2367, 1978.

Berger, A. L.: The Milankovitch astronomical theory of paleoclimates: A modern review, Vistas in Astronomy, 24, Part 2, 103 – 122, doi:http://dx.doi.org/10.1016/0083-6656(80)90026-4, 1980.

Bloemendal, J. and deMenocal, P.: Evidence for a change in the periodicity of tropical climate cycles at 2.4 Myr from whole-core magnetic susceptibility measurements, Nature, 342, 897–900, 1989.

Bonfils, C., de Noblet-Ducoudre, N., Braconnot, P., and Joussaume, S.: Hot Desert Albedo and Climate Change: Mid-Holocene Monsoon in North Africa, Journal of Climate, 14, 3724–3737, 2001.

Bosmans, J. H. C., Drijfhout, S. S., Tuenter, E., Lourens, L. J., Hilgen, F. J., and Weber, S. L.: Monsoonal response to mid-holocene orbital forcing in a high resolution GCM, Climate Of The Past, 8, 723–740, doi:10.5194/cp-8-723-2012, 2012.

Bosmans, J. H. C., Drijfhout, S. S., Tuenter, E., Hilgen, F. J., and Lourens, L. J.: Response of the North-African summer monsoon to precession and obliquity forcing in EC-Earth, under review for publication in Climate Dynamics, 2014.

Braconnot, P. and Marti, O.: Impact of precession on monsoon characteristics from coupled ocean atmosphere experiments: changes in Indian monsoon and Indian ocean climatology, Marine Geology, 201, 23–34, doi:10.1016/S0025-3227(03)00206-8, 2003.

Braconnot, P., Joussaume, S., Noblet, N. D., and Ramstein, G.: Mid-Holocene and Last Glacial Maximum African monsoon changes as simulated within the Paleoclimate Modelling Intercomparison Project, Global and Planetary Change, 26, 51–66, 2000.

Braconnot, P., Otto-Bliesner, B., Harrison, S., Joussaume, S., Peterchmitt, J. Y., Abe-ouchi, A., Crucifix, M., Driesschaert, E., Fichefet, T., Hewitt, C. D., Kageyama, M., Kitoh, A., Laine, A., Loutre, M. F., Marti, O., Merkel, U., Ramstein, G., Valdes, P., Weber, S. L., Yu, Y., and Zhao, Y.: Results of PMIP2 coupled simulations of the Mid-Holocene and Last Glacial Maximum – Part 1: experiments and large-scale features, Climate Of The Past, 3, 261–277, 2007a.

Braconnot, P., Otto-Bliesner, B., Harrison, S., Joussaume, S., Peterchmitt, J. Y., Abe-ouchi, A., Crucifix, M., Driesschaert, E., Fichefet, T., Hewitt, C. D., Kageyama, M., Kitoh, A., Laine, A., Loutre, M. F., Marti, O., Merkel, U., Ramstein, G., Valdes, P., Weber, S. L., Yu, Y., and Zhao, Y.: Results of PMIP2 coupled simulations of the Mid-Holocene and Last Glacial Maximum – Part 2 : feedbacks with emphasis on the location of the ITCZ and mid- and high latitudes heat budget, Climate Of The Past, 3, 279–296, 2007b.

Braconnot, P., Marzin, C., Gregoire, L., Mosquet, E., and Marti, O.: Monsoon response to changes in Earth's orbital parameters: comparisons between simulations of the Eemian and of the Holocene, Climate Of The Past, 4, 281–294,

2008.

Brayshaw, D. J., Rambeau, C. M. C., and Smith, S. J.: Changes in Mediterranean climate during the Holocene: Insight from global and regional climate modelling, The Holocene, 21, 15–31, doi:10.1177/0959683610377528, 2011.

Caley, T., Malaizé, B., Zaragosi, S., Rossignol, L., Bourget, J., Eynaud, F., Martinez, P., Giraudeau, J., Charlier, K., and Ellouz-Zimmermann, N.: New Arabian Sea records help decipher orbital timing of Indo-Asian monsoon, Earth and Planetary Science Letters, 308, 433–444, 2011.

Chen, G.-S., Kutzbach, J. E., Gallimore, R., and Liu, Z.: Calendar effect on phase study in paleoclimate transient simulation with orbital forcing, Climate Dynamics, doi:10.1007/s00382-010-0944-6, 2010.

Chen, G.-S., Zhengyu, L., Clemens, S. C., Prell, W. L., and Liu, X.: Modeling the time-dependent response of the Asian summer monsoon to obliquity forcing in a coupled GCM: a PHASEMAP sensitivity experiment, Climate Dynamics, 36, 695–710, doi:10.1007/s00382-010-0740-3, 2011.

Clemens, S., Prell, W., Murray, D., Shimmield, G., and Weedon, G.: Forcing mechanisms of the Indian Ocean monsoon, Nature, 353, 720–725, 1991.

Clemens, S. C. and Prell, W. L.: A 350,000 year summer-monsoon multi-proxy stack from the Owen Ridge, Northern Arabian Sea, Marine Geology, 201, 35–51, 2003.

Clement, A., Hall, A., and Broccoli, A.: The importance of precessional signals in the tropical climate, Climate Dynamics, 22, 327–341, 2004.

Cook, K. H.: Generation of the African Easterly Jet and Its Role in Determining West African Precipitation, Journal of Climate, 12, 1165–1184, 1999.

Criado-Aldeanueva, F., Soto-Navarro, F., and Garcia-Lafuente, J.: Seasonal and interannual variability of surface heat and freshwater fluxes in the Mediterranean Sea: budgets and exchange through the Strait of Gibraltar, International Journal of Climatology, 32, 286–302, doi:10.1002/joc.2268, 2012.

Dallmeyer, A., Claussen, M., and Otto, J.: Contribution of oceanic and vegetation feedbacks to Holocene climate change in monsoonal Asia, Climate Of The Past, 6, 195–218, 2010.

de Noblet, N., Braconnot, P., Joussaume, S., and Masson, V.: Sensitivity of simulated Asian and African summer monsoons to orbitally induced variations in insolation 126, 115 and 6 kBP, Climate Dynamics, 12, 589–603, 1996.

Dee, D. P., Uppala, S. M., Simmons, A. J., Berrisford, P., Poli, P., Kobayashi, S., Andrae, U., Balmaseda, M. A., Balsamo, G., Bauer, P., Bechtold, P., Beljaars, A. C. M., van de Berg, L., Bidlot, J., Bormann, N., Delsol, C., Dragani, R., Fuentes, M., Geer, A. J., Haimberger, L., Healy, S. B., Hersbach, H., Hlm, E. V., Isaksen, L., Kllberg, P., Khler, M., Matricardi, M., McNally, A. P., Monge-Sanz, B. M., Morcrette, J.-J., Park, B.-K., Peubey, C., de Rosnay, P., Tavolato, C., Thpaut, J.-N., and Vitart, F.: The ERA-Interim reanalysis: configuration and performance of the data assimilation system, Quarterly Journal of the Royal Meteorological Society, 137, 553–597, doi:10.1002/qj.828, 2011.

deMenocal, P. B.: Plio-Pleistocene African climate, Science, 270, 53–59, 1995.

deMenocal, P. B., Ruddiman, W. F., and Pokras, E. M.: Influences of high- and low-latitude processes on African terrestrial climate: Pleistocene eolian records from equatorial Atlantic ocean drilling program site 663, Paleoceanography, 8, 209–242, 1993.

Dias De Melo, M. and Marengo, J. A.: The Holocene simulation of climate during the mid Holocene The influence of changes in orbital parameters over South American climate using the CPTEC AGCM : simulation of climate during the mid Holocene, The Holocene, 18, 501–516, doi:10.1177/0959683608089205, 2008.

D'Ortenzio, F., Iudicone, D., de Boyer Montegut, C., Testor, P., Antoine, D., Marullo, S., Santoleri, R., and Madec, G.: Seasonal variability of the mixed layer depth in the Mediterranean Sea as derived from in situ profiles, Geophysical Research Letters, 32, doi:10.1029/2005GL022463, 2005.

Erb, M. P., Broccoli, A. J., and Clement, A. C.: The contribution of radiative feedbacks to orbitally-driven climate change, Journal of Climate, doi:doi: 10.1175/JCLI-D-12-00419.1, 2013.

Gao, X., Xu, Y., Zhao, Z., Pal, J. S., and Giorgi, F.: On the role of resolution and topography in the simulation of East Asia precipitation, Theoretical and Applied Climatology, 86, 173–185, doi:10.1007/s00704-005-0214-4, 2006.

Gladstone, R., Flecker, R., Valdes, P., Lunt, D., and Marwick, P.: The Mediterranean hydrologic budget from a Late Miocene global climate simulation, Palaeogeography, Palaeoclimatology, Palaeoecology, 251, 254–267, 2007.

Gordon, C., Cooper, C., Senior, C. A., Banks, H., Gregory, J. M., Johns, T. C., Mitchell, J. F. B., and Wood, R. A.: The simulation of SST , sea ice extents and ocean heat transports in a version of the Hadley Centre coupled model without flux adjustments, Climate Dynamics, 16, 147–168, 2000.

Griffin, D. L.: The late Neogene Sahabi rivers of the Sahara and the hamadas of the eastern LibyaChad border area, Palaeogeography, Palaeoclimatology, Palaeoecology, 309, 176–185, 2011.

Hales, K., Neelin, J. D., and Zeng, N.: Interaction of Vegetation and Atmospheric Dynamical Mechanisms in the Mid-Holocene African Monsoon, Journal of Climate, 19, 4105–4120, 2006.

Hall, N. M. J. and Valdes, P. J.: A GCM Simulation of the Climate 6000 Years Ago, Journal of Climate, 10, 3–17, 1997.

Hastenrath, S.: Regional Circulation Systems, in: Climate dynamics of the tropics, chap. 6, Kluwer Academic Publishers, 1991.

Haug, G. H., Hughen, K. A., Sigman, D. M., Peterson, L. C., and Rohl, U.: Southward Migration of the Intertropical Convergence Zone Through the Holocene Southward Migration of the Intertropical Convergence Zone Through the Holocene, Science, 293, 1304–1308, doi:10.1126/science.1059725, 2001.

Hazeleger, W., Severijns, C., Semmler, T., Stefanescu, S., Yang, S., Wyser, K., Wang, X., Dutra, E., Baldasano, J. M., Bintanja, R., Bougeault, P., Caballero, R., Ekman, A. M., Christensen, J. H., van den Hurk, B., Jimenez, P., Jones, C., Kallberg, P., Koenigk, T., McGrath, R., Miranda, P., van Noije, T., Palmer, T.,

Parodi, J. A., Schmith, T., Selten, F., Storelvmo, T., Sterl, A., Tapamo, H., Vancoppenolle, M., Viterbo, P., and Willen, U.: EC-Earth: A Seamless Earth System Prediction Approach in Action, Bulletin of the American Meteorological Society, 91, 1357–1363, 2010.

Hazeleger, W., Wang, X., Severijns, C., Stefanescu, S., Bintanja, R., Sterl, A., Wyser, K., Semmler, T., Yang, S., van den Hurk, B., van Noije, T., van der Linden, E., and van der Wiel, K.: EC-Earth V2.2: description and validation of a new seamless earth system prediction model, Climate Dynamics, doi: 10.1007/s00382-011-1228-5, 2011.

Hilgen, F., Krijgsman, W., Langereis, C., Lourens, L., Santarelli, A., and Zachariasse, W.: Extending the astronomical (polarity) time scale into the Miocene, Earth and Planetary Science Letters, 136, 495–510, 1995.

Hilgen, F. J., Bissoli, L., Iaccarino, S., Krijgsman, W., Meijer, R., Negri, A., and Villa, G.: Integrated stratigraphy and astrochronology of the Messinian GSSP at Oued Akrech (Atlantic Morocco), Earth and Planetary Science Letters, 182, 237–251, 2000.

Hsu, Y.-H., Chou, C., and Wei, K.-Y.: Land Ocean Asymmetry of Tropical Precipitation Changes in the Mid-Holocene, Journal of Climate, 23, 4133–4151, doi: 10.1175/2010JCLI3392.1, 2010.

Imbrie, J. and Palmer Imbrie, K.: Ice ages: solving the mystery, Harvard University Press, 1986.

Jiang, D., Tian, Z., and Lang, X.: Mid-Holocene net precipitation changes over China: model–data comparison, Quaternary Science Reviews, 82, 104–120, 2013.

Jolly, D., Prentice, I. C., Bonnefille, R., Ballouche, A., Bengo, M., Brenac, P., Buchet, G., Burney, D., Cazet, J.-p., Cheddadi, R., Edorh, T., Elenga, H., Elmoutaki, S., Guiot, J., Laarif, F., Lamb, H., Lezine, M., Maley, J., Mbenza, M., Peyron, O., Reille, M., Reynaud, I., Riollet, G., Ritchie, J. C., Roche, E., Scott, L., Ssemmanda, I., Straka, H., Umer, M., Van Campo, E., Vilimumbalo, S., Vincens, A., and Waller, M.: Biome reconstruction from pollen and plant macrofossil data for Africa and the Arabian peninsula at 0 and 6000 years, Journal of Biogeography, 25, 1007–1027, 1998.

Joussaume, S. and Braconnot, P.: Sensitivity of paleoclimate simulation results to season definitions, Journal of Geophysical Research, 102, 1943–1956, 1997.

Joussaume, S., Taylor, K. E., Braconnot, P., Mitchell, F. B., Kutzbach, E., Harrison, S. P., Prentice, I. C., Broccoli, A. J., Abe-Ouchi, A., Bartlein, P. J., Bonfils, C., Dong, B., Guiot, J., Herterich, K., Hewitt, C. D., Jolly, D., Kim, J. W., Kislov, A., Kitoh, A., Loutre, M. F., Masson, V., McAvaney, B., McFarlane, N., Noblet, N. D., Peltier, W. R., Peterschmitt, J. Y., Pollard, I. D., Rind, D., Royer, F., Schlesinger, M. E., Syktus, J., Thompson, S., Valdes, P., Vettoretti, G., Webb, R. S., and Wyputta, U.: Monsoon changes for 6000 years ago: Results of 18 simulations from the Paleoclimate Modeling Intercomparison Project (PMIP), Geophysical Research Letters, 26, 859–862, 1999.

Kanarska, Y. and Maderich, V.: Modelling of seasonal exchange flows through the

Dardanelles Strait, Estuarine, Coastal and Shelf Science, 79, 449–458, 2008.
Kaspar, F., Spangehl, T., and Cubasch, U.: Northern hemisphere winter storm tracks of the Eemain interglacial and the last glacial inception, Climate of the Past, 3, 181–192, 2007.
Khodri, M., Leclainche, Y., Ramstein, G., Braconnot, P., Marti, O., and Cortijo, E.: Simulating the amplification of orbital forcing by ocean feedbacks in the last glaciation, Nature, 410, 570–574, 2001.
Khon, V. C., Park, W., Latif, M., Mokhov, I. I., and Schneider, B.: Response of the hydrological cycle to orbital and greenhouse gas forcing, Geophysical Research Letters, 37, doi:10.1029/2010GL044377, 2010.
Kitoh, A. and Murakami, S.: Tropical Pacific climate at the mid-Holocene and the Last Glacial Maximum simulated by a coupled ocean-atmosphere general circulation model, Paleoceanography, 17, 1–13, doi:10.1029/2001PA000724, 2002.
Kobayashi, C. and Sugi, M.: Impact of horizontal resolution on the simulation of the Asian summer monsoon and tropical cyclones in the JMA global model, Climate Dynamics, 93, 165–176, doi:10.1007/s00382-004-0427-8, 2004.
Kohfeld, K. E. and Harrison, S. P.: How well can we simulate past climates? Evaluating the models using global palaeoenvironmental datasets, Quaternary Science Reviews, 19, 321–345, 2000.
Kutzbach, J. E.: Monsoon Climate of the Early Holocene: Climate Experiment with the Earth's Orbital Parameters for 9000 Years Ago, Science, 214, 59–61, 1981.
Kutzbach, J. E. and Guetter, P. J.: The Influence of Changing Orbital Parameters and Surface Boundary Conditions on Climate Simulations for the Past 18000 years, Journal of the Atmospheric Sciences, 43, 1726–1759, 1986.
Kutzbach, J. E. and Otto-Bliesner, B. L.: The Sensitivity of the African-Asian Monsoonal Climate to Orbital Parameter Changes for 9000 Years B.P. in a Low-Resolution General Circulation Model, Journal of the Atmospheric Sciences, 39, 1177–1188, 1982.
Kutzbach, J. E., Bonan, G. B., Foley, J., and Harrison, S. P.: Vegetation and soil feedbacks on the response of the African monsoon to orbital forcing in the early to middle Holocene, Nature, 384, 623–626, 1996.
Kutzbach, J. E., Liu, X., Liu, Z., and Chen, G.: Simulation of the evolutionary response of global summer monsoons to orbital forcing over the past 280,000 years, Climate Dynamics, 30, 567–579, doi:10.1007/s00382-007-0308-z, 2008.
Kutzbach, J. E., Chen, G., Cheng, H., Edwards, R., and Liu, Z.: Potential role of winter rainfall in explaining increased moisture in the Mediterranean and Middle East during periods of maximum orbitally-forced insolation seasonality, Climate Dynamics, doi:10.1007/s00382-013-1692-1, 2013.
Lal, M., Cubasch, U., Perlwitz, J., and Waszkewitz, J.: Simulation of the Indian monsoon climatology in ECHAM3 climate model: sensitivity to horizontal resolution, International Journal of Climatology, 17, 847–858, 1997.
Larrasoaña, J. C., Roberts, A. P., Rohling, E. J., Winklhofer, M., and Wehausen, R.: Three million years of monsoon variability over the northern Sahara, Climate Dynamics, 21, 689–698, doi:10.1007/s00382-003-0355-z, 2003.

Leuschner, D. C. and Sirocko, F.: Orbital insolation forcing of the Indian monsoon - a motor for global climate changes?, Palaeogeography, Palaeoclimatology, Palaeocology, 197, 83–95, 2003.

Levis, S., Bonan, G. B., and Bonfils, C.: Soil feedback drives the mid-Holocene North African monsoon northward in fully coupled CCSM2 simulations with a dynamic vegetation model, Climate Dynamics, 23, 791–802, doi:10.1007/s00382-004-0477-y, 2004.

Lin, J. L.: The double-ITCZ problem in IPCC AR4 coupled GCMs: Ocean-atmosphere feedback analysis, Journal of Climate, 20, 4497–4525, 2007.

Liu, Z., Harrison, S. P., Kutzbach, J., and Otto-Bliesner, B.: Global monsoons in the mid-Holocene and oceanic feedback, Climate Dynamics, 22, 157–182, doi:10.1007/s00382-003-0372-y, 2004.

Lourens, L. and Reichart, G.-J.: Low latitude forcing of glacial cycles. In: Late Quaternary variability of the Arabian Sea monsoon and oxygen minimum zone, Ph.D. thesis, Utrecht University, 1996.

Lourens, L., Becker, J., Bintanja, R., Hilgen, F., Tuenter, E., van de Wal, R., and Ziegler, M.: Linear and non-linear response of late Neogene glacial cycles to obliquity forcing and implications for the Milankovitch theory, Quaternary Science Reviews, 29, 352–365, 2010.

Lourens, L. J., Antonarakou, A., Hilgen, F. J., Hoof, A. A. M. V., and Zachariasse, W. J.: Evaluation of the Plio-Pleistocene astronomical timescale, Paleoceanography, 11, 391–413, 1996.

Lourens, L. J., Wehausen, R., and Brumsack, H. J.: Geological constraints on tidal dissipation and dynamical ellipticity of the Earth over the past three million years, Nature, 409, 1029–1034, 2001.

Ludwig, W., Dumont, E., Meybeck, M., and Heussner, S.: River discharges of water and nutrients to the Mediterranean and Black Sea: Major drivers for ecosystem changes during past and future decades?, Progress in Oceanography, 80, 199–217, 2009.

Madec, G.: NEMO ocean engine, Tech. rep., Institut Pierre-Simon Laplace, note du Pole de modelisation de l'Institut Pierre-Simon Laplace No 27, 2008, 2008.

Mantsis, D. F.: Atmospheric response to orbital forcing and 20th century sea surface temperatures, Ph.D. thesis, University of Miami, http://scholarlyrepository.miami.edu/oa_dissertations/597, 2011.

Mantsis, D. F., Clement, B., Kirtman, B., Broccoli, A. J., and Erb, M. P.: Precessional cycles and their influence on the North Pacific and North Atlantic summer anticyclones, Journal of Climate, doi:10.1175/JCLI-D-12-00343.1, 2013.

Marchant, R., Cleef, A., Harrison, S. P., Hooghiemstra, H., Markgraf, V., Boxel, J. V., Ager, T., Almeida, L., Anderson, R., Baied, C., Behling, H., Berrio, J. C., Burbridge, R., Bjorck, S., Byrne, R., Bush, M., Duivenvoorden, J., Flenley, J., de Oliveira, P., van Geel, B., Graf, K., Gosling, W. D., Harbele, S., van der Hammen, T., Hansen, B., Horn, S., Kuhry, P., Ledru, M. P., Mayle, F., Leyden, B., Lozano-Garcia, S., Melief, A. M., Moreno, P., Moar, N. T., Prieto, A., van Reenen, G., Salgado-Labouriau, M., Schabitz, F., Schreve-Brinkman, E. J., and

Wille, M.: Pollen-based biome reconstructions for Latin America at 0 , 6000 and 18 000 radiocarbon years ago, Climate Of The Past, 5, 725–767, 2009.

Markgraf, V.: Climatic History of Central and South America since 18,000 yr B.P.: Comparison of Pollen Records and Model Simulations, in: Global climates since the last glacial maximum, edited by Wright, H. E., chap. 14, pp. 357–385, University of Minnesota Press, 1993.

Marzin, C. and Braconnot, P.: Variations of Indian and African monsoons induced by insolation changes at 6 and 9.5 kyr BP, Climate Dynamics, 33, 215–231, doi: 10.1007/s00382-009-0538-3, 2009a.

Marzin, C. and Braconnot, P.: The role of the ocean feedback on Asian and African monsoon variations at 6 kyr and 9.5 kyr BP, Geoscience, 341, 643–655, doi: 10.1016/j.crte.2009.09.001, 2009b.

Masson, V. and Joussaume, S. J.: Energetics of the 6000-yr BP Atmospheric Circulation in Boreal Summer , from Large-Scale to Monsoon Areas : A Study with Two Versions of the LMD AGCM, Journal of Climate, 10, 2888–2903, 1997.

Mayle, F. E., Burbridge, R., and Killeen, T. J.: Millennial-Scale Dynamics of Southern Amazonian Rain Forests, Science2, 290, 2291–2294, doi:10.1126/science. 290.5500.2291, 2000.

Meijer, P. T. and Tuenter, E.: The effect of precession-induced changes in the Mediterranean freshwater budget on circulation at shallow and intermediate depth, Journal of Marine Systems, 68, 349–365, doi:10.1016/j.jmarsys.2007.01.006, 2007.

Merlis, T. M., Schneider, T., Bordoni, S., and Eisenman, I.: The tropical precipitation response to orbital precession, Journal of Climate, 26, doi:10.1175/ JCLI-D-12-00186.1, 2013a.

Merlis, T. M., Schneider, T., Bordoni, S., and Eisenman, I.: Hadley Circulation Response to Orbital Precession. Part II: Subtropical Continent, Journal of Climate, 26, doi:10.1175/JCLI-D-12-00149.1, 2013b.

Montoya, M., von Storch, H., and Crowley, T. J.: Climate Simulation for 125 kyr BP with a Coupled Ocean – Atmosphere General Circulation Model, Journal of Climate, 13, 1057–1072, 2000.

Nicholson, S. E.: A revised picture of the structure of the monsoon and land ITCZ over West Africa, Climate Dynamics, 32, 1155–1171, doi:10.1007/ s00382-008-0514-3, 2009.

Notaro, M., Wang, Y., Liu, Z., Gallimore, R., and Levis, S.: Combined statistical and dynamical assessment of simulated vegetation–rainfall interactions in North Africa during the mid-Holocene1, Global Change Biology, 14, 347–368, 2008.

Ohgaito, R. and Abe-Ouchi, A.: The role of ocean thermodynamics and dynamics in Asian summer monsoon changes during the mid-Holocene, Climate Dynamics, 29, 39–50, doi:10.1007/s00382-006-0217-6, 2007.

Opsteegh, J., Haarsma, R., Selten, F., and Kattenberg, A.: ECBILT: a dynamic alternative to mixed boundary conditions in ocean models, Tellus, 50A, 348–367, 1998.

Paillard, D.: Glacial cycles: toward a new paradigm, Reviews of Geophysics, 39,

325–346, 2001.

Patricola, C. M. and Cook, K. H.: Dynamics of the West African Monsoon under Mid-Holocene Precessional Forcing: Regional Climate Model Simulations, Journal of Climate, 20, 694–716, doi:10.1175/JCLI4013.1, 2007.

Pokras, E. M. and Mix, A. C.: Earth's precessional cycle and Quaternary climatic change in tropical Africa, Nature, 326, 486–487, 1987.

Prell, W. L. and Kutzbach, J. E.: Monsoon Variability Over the Past 150,000 Years, Journal of Geophysical Research, 92, 8411–8425, 1987.

Raymo, M. E. and Nisancioglu, K.: The 41 kyr world: Milankovitch's other unsolved mystery, Paleoceanography, 18, doi:10.1029/2002PA000791, 2003.

Rohling, E. J.: Review and new aspects concerning the formation of eastern Mediterranean sapropels, Marine Geology, 122, 1–28, 1994.

Rohling, E. J. and Hilgen, F. J.: The eastern Mediterranean climate at times of sapropel formation: a review, Geologie en Mijnbouw, 70, 253–264, 1991.

Rossignol-Strick, M.: Mediterranean Quaternary sapropels, an immediate response of the African monsoon to variation of insolation, Palaeogeography, Palaeoclimatology, Palaeoecology, 49, 237–263, 1985.

Rossignol-Strick, M.: Rainy periods and bottom water stagnation initiating brine accumulation and metal concentrations: 1. The late Quaternary, Paleoceanography, 2, 333–360, 1987.

Ruddiman, W. F.: Earth's Climate: Past and Future, W.H. Freeman, 2007.

Saji, N. H., Goswami, B. N., Vinayachandran, P., and Yamagata, T.: A dipole mode in the tropical Indian Ocean, Nature, 401, 360–363, 1999.

Schmidt, G. A., Ruedy, R., Hansen, J. E., Aleinov, I., Bell, N., Bauer, M., Bauer, S., Cairns, B., Canuto, V., Cheng, Y., Del Genio, A., Faluvegi, G., Friend, A. D., Hall, T. M., Hu, Y., Kelley, M., Kiang, N. Y., Koch, D., Lacis, A., Lerner, J., Lo, K. K., Miller, R. L., Nazarenko, L., Oinas, V., Perlwitz, J., Perlwitz, J., Rind, D., Romanou, A., Russel, G. L., Sato, M., Shindell, D. T., Stone, P. H., Sun, S., Tausnev, N., Thresher, D., and Yao, M.-S.: Present-Day Atmospheric Simulations Using GISS ModelE: Comparison to In Situ, Satellite, and Reanalysis Data, Journal of Climate, 19, 153–192, 2006.

Short, D. A. and Mengel, J. G.: Tropical climatic phase lags and Earth's precession cycle, Nature, 323, 48–50, 1986.

Shukla, J.: Interannual Variability of Monsoons, in: Monsoons, edited by Fein, J. S. and Stephens, P. L., chap. 14, pp. 399–464, Wiley Interscience, 1987.

Sierro, F. J., Ledesma, S., Flores, J., Torrescusa, S., and Martinez del Olmo, W.: Sonic and gamma-ray astrochronology: Cycle to cycle calibration of Atlantic climatic records to Mediterranean sapropels and astronomical oscillations, Geology, 28, 695–698, 2000.

Sifeddine, A., Martin, L., Turcq, B., Volkmer-Ribeiro, C., Soubie, F., Campello Cordeira, R., and Suguio, K.: Variations of the Amazonian rainforest environment : a sedimentological record covering 30 , 000 years, Palaeogeography, Palaeoclimatology, Palaeoecology, 168, 221–235, 2001.

Soto-Navarro, F. J., Criado-Aldeanueva, F., Garcia-Lafuente, J., and Sanchez-

Roman, A.: Estimation of the Atlantic inflow through the Strait of Gibraltar from Climatological and in situ data, Journal of Geophysical Research, 115, doi: 10.1029/2010JC006302, 2010.

Sperber, K. R., Hameed, S., Potter, G. L., and Boyle, J. S.: Simulation of the Northern Summer Monsoon in the ECMWF Model: Sensitivity to Horizontal Resolution, Monthly Weather Review, 122, 2461–2481, 1994.

Sterl, A., Bintanja, R., Brodeau, L., Gleeson, E., Koenigk, T., Schmith, T., Semmler, T., Severijns, C., Wyser, K., and Yang, S.: A look at the ocean in the EC-Earth climate model, Climate Dynamics, doi:10.1007/s00382-011-1239-2, 2011.

Street-Perrott, F. A. and Perrot, R. A.: Holocene Vegetation, Lake Levels, and Climate of Africa, in: Global climates since the last glacial maximum, edited by Wright, H. E., chap. 13, pp. 318–356, University of Minnesota Press, 1993.

Su, H. and Neelin, J. D.: Dynamical mechanisms for African monsoon changes during the mid-Holocene, Journal of Geophysical Research, 110, doi:10.1029/2005JD005806, 2005.

Tao, W., Huijun, W., and Dabang, J.: Mid-Holocene East Asian summer climate as simulated by the PMIP2 models, Palaeogeography, Palaeoclimatology, Palaeoecology, 288, 93–102, doi:10.1016/j.palaeo.2010.01.034, 2010.

Texier, D., de Noblet, N., and Braconnot, P.: Sensitivity of the African and Asian Monsoons to Mid-Holocene Insolation and Data-Inferred Surface Changes, Journal of Climate, 13, 164–181, 2000.

Tian, Z. and Jiang, D.: Mid-Holocene ocean and vegetation feedbacks over East Asia, Climate of the Past, 9, 2153–2171, doi:10.5194/cp-9-2153-2013, 2013.

Tiedemann, R., Sarnthein, M., and Shackleton, N. J.: Astronomic timescale for the Pliocene Atlantic δ18O and dust flux records of Ocean Drilling Program Site 659, Paleoceanography, 9, 619–638, 1994.

Tuenter, E.: Modeling orbital induced variations in circum-Mediterranean climate, Ph.D. thesis, Utrecht University, 2004.

Tuenter, E., Weber, S. L., Hilgen, F. J., and Lourens, L. J.: The response of the African summer monsoon to remote and local forcing due to precession and obliquity, Global and Planetary Change, 36, 219 – 235, doi:10.1016/S0921-8181(02)00196-0, 2003.

Tuenter, E., Weber, S., Hilgen, F., Lourens, L., and Ganopolski, A.: Simulation of climate phase lags in response to precession and obliquity forcing and the role of vegetation, Climate dynamics, 24, 279–295, 2005.

Turcq, B., Albuquerque, A. L. S., Cordeiro, R. C., Sifeddine, A., Simoes Filho, F. F. L., Souza, A. G., Abrao, J. J., Oliveira, F. B. L., Silva, A. O., and Capita, J.: Accumulation of organic carbon in five Brazilian lakes during the Holocene, Sedimentary Geology, 148, 319 – 342, 2002.

Tzedakis, P. C.: Seven ambiguities in the Mediterranean palaeoenvironmental narrative, Quaternary Science Reviews, 26, 2042–2066, 2007.

Valcke, S. and Morel, T.: OASIS3 user guide, Tech. rep., CERFACS, prism Technical Report, 68pp, available online at http://www.prism.enes.org/Publications/Reports/oasis3_UserGuide_T3.pdf,

2006.

Valdes, P. J.: South American palaeoclimate model simulations: how reliable are the models ?, Journal of Quaternary Science, 15, 357–368, 2000.

Vamborg, F. S. E., Brovkin, V., and Claussen, M.: The effect of a dynamic background albedo scheme on Sahel / Sahara precipitation during the mid-Holocene, Climate Of The Past, 7, 117–131, doi:10.5194/cp-7-117-2011, 2011.

van der Laan, E., Gaboardi, S., Hilgen, F. J., and Lourens, L. J.: Regional climate and glacial control on high-resolution oxygen isotope records from Ain el Beida (latest Miocene, northwest Morocco): A cyclostratigraphic analysis in the depth and time domain, Paleoceanography, 20, 1–22, doi:10.1029/2003PA000995, 2005.

van der Laan, E., Hilgen, F. J., Lourens, L. J., Kaenel, E. d., Gaboardi, S., and Iaccarino, S.: Astronomical forcing of Northwest African climate and glacial history during the late Messinian (6.55.5 Ma), Palaeoceanography, Palaeoclimatology, Palaeoecology, 313-314, 107126, doi:10.1029/2003PA000995, 2012.

Wang, T. and Wang, H.: Mid-Holocene Asian summer climate and its responses to cold ocean surface simulated in the PMIP2 OAGCMs experiments, Journal of Geophysical Research: Atmospheres, pp. 1–12, 2013.

Wang, Y., Cheng, H., Edwards, R. L., Kong, X., Shao, X., Chen, S., Wu, J., Jiang, X., Wang, X., and An, Z.: Millennial-and orbital-scale changes in the East Asian monsoon over the past 224,000 years, Nature, 451, 1090–1093, 2008.

Wang, Y., Jian, Z., and Zhao, P.: Extratropical modulation on Asian summer monsoon at precessional bands, Geophysical Research Letters, 39, 2012.

Weber, S. L. and Tuenter, E.: The impact of varying ice sheets and greenhouse gases on the intensity and timing of boreal summer monsoons, Quaternary Science Reviews, 30, 469–479, 2011.

Webster, P. J.: The Elementary Monsoon, in: Monsoons, edited by Fein, J. S. and Stephens, P. L., chap. 1, pp. 3–32, Wiley Interscience, 1987a.

Webster, P. J.: The Variable and Interactive Monsoon, in: Monsoons, edited by Fein, J. S. and Stephens, P. L., chap. 11, pp. 269–330, Wiley Interscience, 1987b.

Webster, P. J., Magana, V. O., Palmer, T. N., Shukla, J., Tomas, R. A., Yanai, M., and Yasunari, T.: Monsoons : Processes , predictability , and the prospects for prediction 2 . Description of the Monsoons, Journal, 103, 451–510, 1998.

Winkler, M. G. and Wang, P. K.: The Late-Quaternary Vegetation and Climate of China, in: Global climates since the last glacial maximum, edited by Wright, H. E., chap. 10, pp. 221–256, University of Minnesota Press, 1993.

Wu, H., Guiot, J., Brewer, S., and Guo, Z.: Climatic changes in Eurasia and Africa at the last glacial maximum and mid-Holocene: reconstruction from pollen data using inverse vegetation modelling, Climate Dynamics, 29, 211–229, doi:10.1007/s00382-007-0231-3, 2007.

Wyrwoll, K.-h., Liu, Z., Chen, G., Kutzbach, J. E., and Liu, X.: Sensitivity of the Australian summer monsoon to tilt and precession forcing, Quaternary Science Reviews, 26, 3043–3057, doi:10.1016/j.quascirev.2007.06.026, 2007.

Xie, P. and Arkin, P. A.: Global Precipitation: A 17-Year Monthly Analysis Based

on Gauge Observations, Satellite Estimates, and Numerical Model Outputs, Bulletin of the American Meteorological Society, 78, 2539–2558, 1997.

Yu, G. and Harrison, S. P.: An evaluation of the simulated water balance of Eurasia and northern Africa at 6000 y BP using lake status data, Climate Dynamics, 12, 723–735, 1996.

Yu, G., Prentice, I. C., Harrison, S. P., and Sun, X.: Pollen-based biome reconstructions for China at 0 and 6000 years, Journal of Biogeography, 25, 1055–1069, 1998.

Zhao, Y. and Harrison, S. P.: Mid-Holocene monsoons: a multi-model analysis of the inter-hemispheric differences in the responses to orbital forcing and ocean feedbacks, Climate Dynamics, 39, 1457–1487, doi:10.1007/s00382-011-1193-z, 2012.

Zhao, Y., Braconnot, P., Marti, O., Harrison, S. P., Hewitt, C., Kitoh, A., Liu, A., Mikolajewicz, U., Otto-Bliesner, B., and Weber, S. L.: A multi-model analysis of the role of the ocean on the African and Indian monsoon during the mid-Holocene, Climate Dynamics, 25, 777–800, doi:10.1007/s00382-005-0075-7, 2005.

Zheng, W., Wu, B., He, J., and Yu, Y.: The East Asian Summer Monsoon at mid-Holocene: results from PMIP3 simulations, Climate of the Past, 9, 453–466, doi:10.5194/cp-9-453-2013, 2013.

Zhou, T. J. and Li, Z. X.: Simulation of the east asian summer monsoon using a variable resolution atmospheric GCM, Climate Dynamics, 19, 167–180, doi: 10.1007/s00382-001-0214-8, 2002.

Ziegler, M., Lourens, L. J., Tuenter, E., Hilgen, F., Reichart, G.-J., and Weber, N.: Precession phasing offset between Indian summer monsoon and Arabian Sea productivity linked to changes in Atlantic overturning circulation, Paleoceanography, 25, n/a–n/a, doi:10.1029/2009PA001884, 2010a.

Ziegler, M., Tuenter, E., and Lourens, L.: The precession phase of the boreal summer monsoon as viewed from the eastern Mediterranean (ODP Site 968), Quaternary Science Reviews, 29, 1481 – 1490, doi:http://dx.doi.org/10.1016/j.quascirev.2010.03.011, 2010b.

Summary

This thesis focuses on orbitally forced changes of monsoons and Mediterranean climate. Changes in the shape of the Earth's orbit around the Sun and its rotational axis govern the seasonal and latitudinal distribution of incoming solar radiation on time scales of thousands to millions of years. The three orbital parameters, eccentricity, precession and obliquity, are reflected in sedimentary records from all over the world. In this thesis a state-of-the-art coupled general circulation model, EC-Earth, is used to obtain a physical basis of climate response to orbital forcing.

First, a Mid-Holocene experiment is discussed, performed within the framework of the Paleoclimate Modelling Intercomparison Project (PMIP3). Stronger northern hemisphere summer insolation results in intensified monsoons in North-Africa and Asia, while reduced southern hemisphere summer insolation results in a weaker South-American monsoon. Over North-Africa, the monsoon extends further poleward during the Mid-Holocene. These results corroborate the findings of paleoclimate proxy studies as well as previous model studies, while giving a more detailed account of Mid-Holocene summer monsoons.

Secondly, the response of the North-African and Asian summer monsoons to separate precession and obliquity forcing is investigated. Strengthening of the North-African monsoon during minimum precession and maximum obliquity, when northern hemisphere summer insolation is increased, is mostly related to stronger monsoon winds carrying moisture from the tropical Atlantic Ocean. This is in contrast to previous studies suggesting high-latitude mechanisms. Furthermore, the monsoon winds, convection and precipitation extend farther north into the Sahara. The Asian monsoons are strengthened as well during minimum precession and maximum obliquity. Southerly monsoon winds over East-Asia are stronger due to an intensified west-east land-sea pressure gradient. The intensified North Pacific High is connected to anomalously high pressure over south-east Asia, and an Indian Ocean Dipole pattern emerges. The Indian monsoon is stronger, but the increased precipitation over the western Indian Ocean and decreased wind speed over the northern Indian Ocean damp the monsoon strengthening. The southern tropical Indian Ocean acts as a moisture source for the enhanced monsoon precipitation.

Thirdly, the influence of obliquity on low-latitude climate is addressed. Obliquity-induced insolation changes at low latitudes are very small, therefore glacial cycles

and other high latitude mechanisms are often invoked to explain low-latitude obliquity signals. However, the model results in this study show that obliquity-induced changes can occur through changes in the tropical cross-equator-ial insolation gradient. This gradient is stronger during high obliquity, causing increased cross-equatorial wind and moisture transport and therefore a re-distribution of precipitation.

Lastly, the effect of precession and obliquity on the freshwater budget of the Mediterranean is examined. Ample proxy studies suggest that the area was wetter and that the Mediterranean Sea was less saline at times of enhanced insolation seasonality, i.e. minimum precession and maximum obliquity. The EC-Earth results show that during these situations, both summer monsoonal runoff through the Nile as well as winter precipitation over the Mediterranean Sea are increased. The first is most important for precession, the latter for obliquity. The changes in winter precipitation are related to changes in the air-sea temperature difference.

Samenvatting

Onder invloed van de zwaartekracht van de zon, de maan en de planeten verandert de baan van de aarde rondom de zon. Deze veranderingen, die plaats vinden op tijdschalen van duizenden tot miljoenen jaren, beïnvloeden de verdeling van zonnestraling over de aarde. De resulterende cyclische klimaatveranderingen op de aarde zijn zichtbaar in fossielen en gesteenten. Er zijn drie astronomische (of Milankovitch) cycli die we terugzien in fossielen en gesteenten: veranderingen in de excentriciteit (ellipticiteit) van de aardbaan, veranderingen in de hoek van de aardas ten opzichte van het vlak waarin de aarde om de zon draait (obliquiteit) en de precessie van de equinoxen (zie Figuur 1.1). Samen controleren de eccentriciteit, obliquiteit en precessie de verdeling van zonnestraling over de seizoenen en de breedtegraden.

Met het klimaatmodel EC-Earth zijn experimenten uitgevoerd om te onderzoeken hoe het klimaat reageert op veranderingen in de baan van de aarde om de zon. Modelexperimenten zijn nodig om het verband tussen de astronomisch gestuurde veranderingen in zonnestraling en de astronomische cycli in fossielen en gesteenten beter te begrijpen. EC-Earth is een globaal atmosfeer-oceaan-land model met completere en geavanceerdere fysica en een hogere resolutie dan de meeste modellen die voor vergelijkbare studies gebruikt worden.

Moessons spelen een belangrijke rol in het klimaat van de tropen. In de zomer, wanneer de zonnestraling het sterkst is, warmt land sneller op dan oceaan. De luchtdruk boven land wordt lager dan boven de oceaan, en lucht boven land stijgt op. Hierdoor waait de wind vanaf de oceaan naar het land. Deze moesson-wind voert waterdamp aan, wat condenseert en uitregent boven land. De warmte die vrijkomt bij condensatie is een bron van energie voor de moesson.

In het Mid-Holoceen, zo'n 6000 jaar geleden, ontving het noordelijk halfrond meer zonnestraling in de zomer. De landmassa's van Noord-Afrika en Azië warmden daardoor nog meer op, en de moessonwinden en het vochttransport vanaf de oceaan waren sterker. Daardoor viel er meer regen in de Noord-Afrikaanse en Aziatische moessongebieden. De Noord-Afrikaanse moesson reikte ook verder noordwaards. De Zuid-Amerikaanse moesson was zwakker, omdat het zuidelijk halfrond in het Mid-Holoceen minder zonnestraling ontving. De EC-Earth resultaten voor het Mid-Holoceen komen overeen met geologische data, zoals pollen, plantfossielen en het waterpeil van meren. Het model produceert echter wel nog te weinig neerslag

boven de Sahara. Een oorzaak hiervan kan zijn dat EC-Earth, net als veel andere modellen, geen veranderingen in vegetatie berekent. Als het model dit wel zou doen, dan zou er door de sterkere moesson-regen meer vegetatie in de Sahel en de Sahara groeien. Het albedo van het land (weerkaatsingsvermogen) zou dan lager zijn, waardoor het land nog sterker opwarmt bij hogere zonnestraling en de moesson dus nog meer versterkt zou zijn.

Ook geïdealiseerde experimenten laten zien dat de moessons van Noord-Afrika en Azië sterk op veranderingen in de verdeling van zonnestraling reageren. De precessie van de equinoxen bepaalt welk seizoen op welke plek van de (excentrische) aardbaan plaatsvindt. Dit heeft een grote invloed op de verdeling van zonnestraling over de seizoenen, en daarom ook een grote invloed op de moessons. Wanneer de zomer op het noordelijk halfrond relatief dicht bij de zon plaatsvindt, en de hoeveelheid zonnestraling dus toegenomen is, zijn de moessonwinden sterker. Ze brengen dan ook meer vocht van zee naar land.

Veranderingen in de stand van de aardas (obliquiteit) hebben een veel kleinere invloed op de zonnestraling, vooral op lage breedtegraden, maar toch heeft obliquiteit invloed op de moessons en het tropische klimaat. De moessons zijn sterker wanneer de aardas schever staat, want dan is er meer zonnestraling op het halfrond waar het zomer is. Tot op heden werd de invloed van obliquiteit op het tropische klimaat toegeschreven aan klimaatveranderingen op hogere breedtegraden, waar obliquiteit grotere veranderingen in zonnestraling veroorzaakt. De EC-Earth experimenten laten echter zien dat obliquiteit het tropische klimaat kan beïnvloeden zonder veranderingen in ijskappen of andere veranderingen op hogere breedtegraden. Veranderingen in luchtcirculatie-patronen hangen samen met obliquiteit-gestuurde veranderingen in het verschil in zonnestraling tussen de keerkringen.

Veranderingen in de Noord-Afrikaanse moesson leiden tevens tot fluctuaties in uitstroom van de Nijl, en daarmee tot veranderingen in de Middellandse Zee. Er is veel geologisch bewijs dat precessie en obliquiteit het zoutgehalte van de Middellandse Zee beïnvloeden. Maar ook veranderingen in neerslag boven de Middellandse Zee zelf kunnen de zee zoeter of zouter maken. Wanneer de uitstroom van de Nijl toeneemt, neemt ook de neerslag boven de Middellandse Zee toe. EC-Earth laat zien dat beiden een grote rol spelen in het zoetwater-budget van de zee. De uitstroom van de Nijl verandert vooral in de late zomer, als gevolg van veranderingen in de moesson. Veranderingen in neerslag boven de Middellandse Zee vinden vooral plaats in de winter, en hangen samen met verschillen in temperatuur tussen het zee-oppervlak en de lucht. Nijl-uitstroom en neerslag kunnen beiden de diepzee-circulatie beïnvloeden, welke van de twee een grotere rol speelt dient verder onderzocht te worden met een gedetailleerd Middellandse Zee-model.

Acknowledgements

I could not have finished this thesis without the help of many, many people. Writing the acknowledgments, an important part of my thesis, makes me realise how blessed I am with amazing friends, family and colleagues. Therefore: a BIG thanks to all of you who have helped me with the scientific and technical aspects of my work over the past years, and, equally important, to those who helped take my mind off my thesis.

First and foremost I would like to thank those who gave me the opportunity to start this PhD project: Nanne Weber, Frits Hilgen and Luc Lourens. I would have gladly worked with Nanne longer, but I am thankful for her supervision and help during the first part of my PhD-project. She was, and still is, an inspiration. To Frits and Luc I am grateful the many conversations in which they patiently explained many aspects of astronomical forcing, orbital tuning and paleoclimatology in general, so that I could understand the roots of the research problems and place my research in a wider context. Luc, thank you for your advice, support and for stepping up as promotor. Frits, thank you for taking me, a climate modeller with very little experience in geology, into the field at Monte dei Corvi, together with Christian. Your enthousiasm and hard work in the field, as well as in the office, is inspirational.

Later on in the project Erik Tuenter and Sybren Drijfhout became involved as supervisors. Erik, it was great to have a fellow paleoclimate-modeller, especially one who was always happy to answer any quesions I had. Thank you for the many discussions on either scientific content or technical details. Sybren, thank you for taking over the supervision of my PhD-work at KNMI and becoming a promotor. Your quick and valuable responses to my questions and feedback on manuscripts, even now you are in Southampton most of the time, are much appreciated.

I am also grateful to the scientists who took the time to asses this thesis, as a member of the reading committee and / or the opposition: Pascale Braconnot, Hans Renssen, Eelco Rohling, Paul Valdes, Hans Middelkoop and Henk Dijkstra.

At KNMI I spent the first months at the Chemistry and Climate group, and I would like to thank everyone there for their help and support. Specifically, thanks to Peter van Veldhoven and Miranda van Brussel-Verzuu, as well as Philippe le Sager for all the help on technical aspects. Also, I was very fortunate with my roommate in

those first months: Renske de Winter. I appreciate all the help and conversations we had during both of our PhD projects, on both scientific and very much non-scientific matters. Also, thanks to Ingrid, Cintia, Marie-Jette, Rikke and Niels.

Near the end of my first year I moved to the Global Climate group at KNMI. Thanks to Wilco Hazeleger and Brigitta Kamphuis for facilitating this and for your support during my stay in your group. Everyone else in the Global Climate group was very welcoming as well, so thank you Sybren, Rein, Andreas, Richard, Camiel, Frank, Siswanto, Bert, Ronald, Elodie, Erik, Xueli, Paul, Martina, Marco, Eveline, Renske, Erik, Hylke, Sarah, Folmer, Iris, Andrea, Michiel, Paul, Geert Jan, Bart, Caroline, Lucinda, Renske, Jelle, Carlo, Clifford, Anna-Lena, Sara, Jessica and Irene. I have bothered most of you with my questions, some more than others: Camiel Severijns, thank you for all your help on EC-Earth and other issues. The same goes for Richard Bintanja, Andreas Sterl, Bert Wouters and Xueli Wang. Xueli, you were also a great roommate, thank you for your company. Hylke de Vries and Rein Haarsma, thank you for help with the storm track analysis. Eveline van der Linden, I really enjoyed our tea breaks, biking to work together, and the many other times we chatted during and outside of work hours.

At the university I worked at the Stratigraphy and Paleontology group at the Earth Sciences department. Again I was blessed with great roommates. Hemmo Abels, thank you for help on Mac-related issues, manuscripts and many scientific discussions. Christian Zeeden, danke schön für dein wissenschaftliche Enthusiasmus, viel Tee, Monte dei Corvi, Wien, und Cocktails! To Luc, Frits, Wilma, Ivo, Kees, Tiuri, Helen, Vittoria, Antonio, Chaowen, Stefanie, Margreet, Maria, Marjolein, Mariëtte, Bas, Marie-Louise, Itzel, Robin, Rick and Mathilde: thank you for showing an interest in my work, for patiently introducing me to your areas of expertise, and also for all the great times at (many) office drinks, water skiing, laser gaming, and yes, even the running.

I acknowledge the support from the department of Physical Geography, especially from Marjan Rossen. Furthermore, thank you for giving me the freedom to work at Earth Sciences and KNMI.

Besides the support at the University and KNMI I had a lot of support from abroad. Without the help and patient answers to my many emails by Simona Stefanescu at ECMWF I could not have performed my EC-Earth experiments. The same goes to Dominique Lucas and Shuting Yang. To Willem-Jan van de Berg and Aurore Voldoire I am grateful for sharing their work on changing the insolation code. Alastair McKinstry, thank you for your help on publishing the results of my PMIP experiments. Within PMIP I would like to thank Pascale Braconnot, Masa Kageyama and Jean-Yves Peterschmitt at IPSL-LSCE. Merci beaucoup to Pascale Braconnot for your help analysing the PMIP results during my visits to your institute. Your help was very fruitful for the Mid-Holocene paper. I am also grateful to Alice Marzocchi for sharing your work on orbital forcing, and for inviting me for a visit to the University of Bristol. The discussions with you, Dan Lunt and Rachel Flecker were very useful. After Bristol I headed to the University of Leeds: thanks to Aisling Dolan, Alan Haywood, Lauren Gregoire and Ruza Ivanovic for

great discussions and a great stay.

Also abroad, at the Urbino summer school, and later on back in Utrecht, I had some great times with my colleagues-turned-friends Robin Topper, Itzel Ruvalcaba Baroni and Marie-Louise Goudeau. I appreciate the discussions on our work as well as all the tea breaks, cakes, trips and diners together. Robin, thanks for all the help with Fortran, LaTeX (including the lay-out for this thesis) and the discussions on the Mediterranean.

Others that have helped me take my mind off of thesis-related things include my dear friends Martine and Loes. Thank you very much for your interest in my work and general well-being, and for patiently listening to me babbling on about the good, the bad and the ugly parts of my PhD research. Paula, Anke, Pauline and Jolina, thanks for the great weekends and other fun times.

Near the end of the acknowledgements I would like to thank those who have been a constant supporting factor during my PhD, and actually during my whole life: my family. Mom and dad, Gwenn and Jill, thank you for providing a great home base, for interest in my studies and my work, and for supporting me throughout school and university. My thanks also extends to the rest of my family, including Luuk, Maarten, Jan and Elly.

Then, last and above all, a very big thanks to Jasper, for your technical help, reading manuscripts and summaries, but most of all for your endless affection, support and patience.

Curriculum Vitæ

Joyce Bosmans was born on August 3rd 1986 in Roermond, the Netherlands. She lived in Grathem and attended the Scholengemeenschap St. Ursula in Horn, where she obtained her gymnasium diploma in 2004. She then moved to Utrecht and attended University College Utrecht. In 2006 she spent a semester at the University of Hull in the United Kingdom and in 2007 she obtained her bachelor degree. After that she started studying "Meteorology, Physical Oceanography and Climate" at the Institute for Marine and Atmospheric research Utrecht (IMAU) of the Faculty of Science at Utrecht University. Her master thesis focussed on the effect of surface meltwater on the Greenland Ice Sheet. At the end of 2009 Joyce finished her master and started working on the PhD project on which this thesis is based. This project was funded by the Faculty of Geosciences at Utrecht University through a "Focus en Massa" grant of Nanne Weber and Frits Hilgen. During this project she worked at the Stratigraphy and Paleontology group in Utrecht, with Frits Hilgen and Luc Lourens, as well as at the Royal Netherlands Meteorological Institute (KNMI), with Erik Tuenter and Sybren Drijfhout. From April 2014 onwards, Joyce will work as a post-doctoral researcher at the department of Physical Geography at the Faculty of Geosciences at Utrecht University, within the project "Water, Climate and Ecosystems".